Combined magnetic resonance imaging and photodynamic therapy using polyfunctionalised nanoparticles bearing robust gadolinium surface units

Nicolas G. Chabloz,[a] Hannah L. Perry,[a,b] Il-Chul Yoon,[a] Andrew J. Coulson,[a] Andrew J. P. White,[a] Graeme J. Stasiuk,[c] René M. Botnar[b] and James D. E. T. Wilton-Ely*[a,d]

[a] *Dr. N. G. Chabloz, H. L. Perry, I.-C. Yoon, A. J. Coulson, Dr. A. J. P. White, Prof. Dr. J. D. E. T. Wilton-Ely*
Department of Chemistry
Imperial College London
Molecular Sciences Research Hub
White City Campus
London W12 0BZ (UK).
E-mail: j.wilton-ely@imperial.ac.uk

[b] *H. L. Perry, Prof. Dr. René M. Botnar*
Division of Imaging Sciences and Biomedical Engineering
King's College London
St Thomas' Hospital
London SE1 7EH (UK)

[c] *Prof. Dr. G. Stasiuk*
School of Life Sciences, Biomedical Sciences, University of Hull, Hull HU6 7RX (UK)

[d] *Prof. Dr. J. D. E. T. Wilton-Ely*
London Centre for Nanotechnology (LCN)

In memory of Sir Rex Richards FRS FRSC FBA (1922 – 2019)

Abstract

A robust dithiocarbamate tether allows novel gadolinium units based on DOTAGA (q = 1) to be attached to the surface of gold nanoparticles (2.6 - 4.1 nm diameter) along with functional units offering biocompatibility, targeting and photodynamic therapy. A dramatic increase in relaxivity (r_1) per Gd unit from 5.01 mM^{-1} s^{-1} in unbound form to 31.68 mM^{-1} s^{-1} (10 MHz, 37 °C) is observed when immobilised on the surface due to restricted rotation and enhanced rigidity of the Gd complex on the nanoparticle surface. The single-step synthetic route provides a straightforward and versatile way of preparing multifunctional gold nanoparticles, including examples with conjugated zinc-tetraphenylporphyrin photosensitizers. The lack of toxicity of these materials (MTT assays) is transformed on irradiation of HeLa cells for 30 minutes (PDT), leading to 75% cell death. In addition to passive targeting, the inclusion of units capable of actively targeting overexpressed folate receptors illustrates the potential of these assemblies as targeted theranostic agents.

Keywords: Gadolinium, imaging agents, MRI, nanoparticles, PDT

Introduction

Nanoparticles have found widespread use in medicine to address applications such as imaging,[1,2] therapy[3,4] and drug delivery.[5] Superparamagnetic iron oxide nanoparticles (SPIONs) such as Feridex/Endorem and Resovist have been approved for clinical use while other nanoparticle-based formulations are undergoing clinical trials.[6] Gold nanoparticles (GNPs) are amongst the most studied due to their biocompatibility, the ease with which their dimensions can be controlled and the well-established methods for attachment of surface units through sulfur linkages (principally thiols).[7] The thermal response to near-IR light irradiation of gold nanostructures (photothermal therapy, PTT) has also attracted interest, but it is less established than the more widely-used photodynamic therapy (PDT), where cytotoxic singlet oxygen / radicals are generated by the photoexcitation of photosensitizers administered to the patient.[8] The accumulation of gold nanoparticles at tumour sites due to their leaky, immature vasculature with wider fenestrations than normal mature blood vessels, known as the enhanced permeability and retention (EPR) effect,[9] has led to the increasing use of GNPs in cancer therapy.[10]

This passive targeting imbues nanostructures with a great advantage over smaller, molecular substrates. In conjunction with this effect, the selectivity of the material for certain cell types can be dramatically increased by the addition of targeting surface units, such as aptamers or antibodies.[11] Gold nanostructures bearing aptamers show very specific protein binding, bringing the material into the proximity of the target protein, allowing targeting to be combined with therapy (such as PTT) to achieve localised destruction of cells.[12-14]

Magnetic resonance imaging (MRI) is a non-invasive technique that exploits the same principles as NMR to acquire detailed anatomical images with the highest spatial resolution of all the imaging modalities. In the body, different tissue types possess diverse fundamental relaxation parameters (T_1/T_2) as a result of their different proton densities. This intrinsic contrast allows a detailed anatomical image to be acquired using MRI. Contrast agents are often used to enhance the image and allow finer detail to be revealed and this is particularly important in the early diagnosis of pathologies such as cancer. Contrast enhancement occurs through the acceleration of the relaxation of water protons localised in the surrounding tissue. This can be achieved by the presence of an exogenous paramagnetic species, as T_1 recovery and T_2 decay are affected by the local magnetic moment. A more effective contrast agent results in larger relaxivity values (in mM^{-1} s^{-1}) as a function of concentration.[15] Most clinically-used contrast agents are based on paramagnetic ($4f^7$) gadolinium(III) ions, which interact with water

molecules to improve the relaxation rates of the protons, enhancing the image contrast.[15] The immobilisation of trivalent gadolinium units on the surface of gold nanoparticles dramatically increases the relaxation rate experienced by the protons of the water molecules in their vicinity.[16-29] This can be partly traced to the effect on the rotational correlation time, which increases when the assembly rotates slowly, leading to greatly increased relaxivity per Gd(III) ion. In addition to this intrinsic enhancement, the presence of many gadolinium ions creates a multimeric effect on the relaxation of water protons due to the increased localised contrast agent concentration.[15-33]

All current clinically-approved gadolinium magnetic resonance contrast agents (such as Dotarem™, shown in Fig. 1a) are extracellular probes with a non-specific biodistribution. One of the aims of the research described here is to add to the development of a new generation of contrast agents, which are able to recognise early reporters of a given pathology on the cellular surface. The targeting of overexpressed membrane receptors using MRI is hampered by the very low concentration of such receptors and by the relatively low sensitivity of Gd(III) contrast agents. This limitation can be overcome through the accumulation of a large number of imaging moieties (hundreds of Gd units) at the target site through active recognition by neighbouring surface units on the nanoparticle (*e.g.* folic acid).

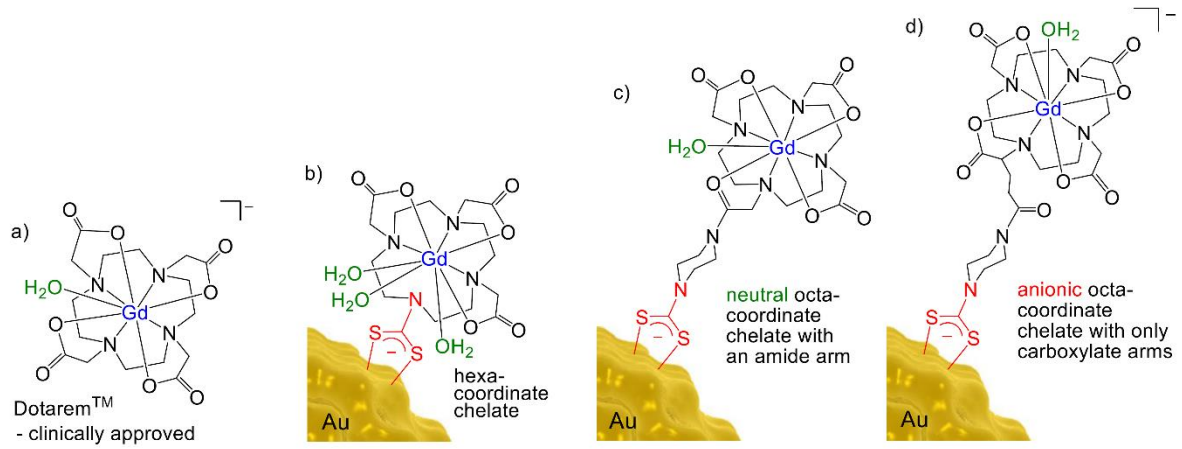

Figure 1. Design of a) clinically-approved contrast agent, Dotarem™ (q = 1), b) hexa-coordinate Gd chelate (q = 3) with dithiocarbamate tether (shown in red), c) the previously reported neutral octa-coordinate Gd chelate (q = 1) with dithiocarbamate tether and d) the anionic octa-coordinate Gd chelate (q = 1) reported in this work.

Our interest in the surface functionalisation of gold nanoparticles (GNPs) with metal began in 2008,[34] and since then much of our work[33-38] has focused on the use of dithiocarbamate

($R_2NCS_2^-$) tethers as an alternative to the ubiquitous thiol(ate) or disulfide attachment methodologies for GNPs. Competition experiments[38,39] have demonstrated that dithiocarbamates are able to displace thiol(ate)s from the surface of the nanoparticle, but not *vice versa*. This more robust attachment methodology is gaining popularity but there are still relatively few examples of metals being tethered to GNPs this way.[40] Computational approaches using Au_{20} nanoclusters have helped to provide a rationale for the more robust attachment observed.[41] These investigations reveal that there is much less distortion and reorganisation of the gold atoms when dithiocarbamate units are introduced to the Au_{20} surface compared to the case for thiolates. With dithiocarbamates, no evidence is found for the 'stapling' effect with thiolates, which has been observed structurally by Kornberg and co-workers in the crystal structure of $Au_{102}(SC_6H_4CO_2H\text{-}4)_{44}$ nanoparticles (diameter 1.6 nm).[42] 'Staples' form when a gold atom is lifted from the assembly and pinned between the two nearest thiolates, potentially making it prone to loss, for example as a molecular $[Au(SR)_2]^-$ unit (observed experimentally).[43] Though often not acknowledged (and quite possibly overlooked or ignored), the attachment through a single thiol(ate) tether often leads to detachment from the nanoparticle surface and this is likely to be exacerbated under physiological conditions. The performance of molecular contrast agents can be dramatically enhanced by increasing the mass of the assembly and this has been achieved through attachment to polymers, liposomes or nanoparticles, or through the formation of multimetallic (metallostar) motifs.[15] This has been widely used in conjunction with approaches to reduce the freedom of rotation of the Gd(III) units to further enhance the relaxation imparted to the protons of the nearby water molecules.

In 2014, we reported the first example of dithiocarbamates being used to attach gadolinium units to GNPs for potential use in MRI imaging.[33] These materials (Fig. 1b) showed promising relaxivities, however, the hexadentate coordination of the Gd^{3+} ion (q = 3) undermined their application due to the potential for loss of the toxic gadolinium ions under physiological conditions. This was a major factor in the improved design we have described previously,[44] based on an octadentate coordination environment (Fig. 1c), similar to Dotarem™ (Fig. 1a).[45] However, unlike Dotarem™, the resultant Gd chelate (Fig. 1c) is neutral rather than anionic. This could lead to a weaker interaction between the amide carbonyl lone pair and the Gd(III) centre, potentially impacting on the relaxivity performance and the complex stability. In addition, it has been shown[45] that macrocyclic chelates with carboxylate arms have faster water exchange rates (contributing to higher relaxivity) than macrocyclic chelates with amide arms. These factors were key to our new chelate design, which contains carboxylate arms and

no amide donors. This modification is also significant as it creates the same coordination environment found in a leading contrast agent in widespread clinical use, Dotarem^{TM}. This similarity to a clinically-approved compound also provides reassurance (particularly in the context of Nephrogenic Systemic Fibrosis, NSF) that the toxic gadolinium(III) ion will not be released under biological conditions. The considerations outlined above led to the design of a new anionic gadolinium(III) chelate (Fig. 1d) with carboxylate donors and a dithiocarbamate tether.

In the context of a multifunctional surface, this approach exploits the most robust tether (dithiocarbamate) to attach the most critical surface unit, the imaging modality. In an orthogonal approach, additional groups can then be secured using less robust (di)thiol(ate) groups, providing biocompatibility, targeting and a therapeutic function. The straightforward synthesis combined with the versatility offered by a modular design, gives access to a wide range of materials that can be used as a platform for combined imaging and therapy. In this report, the well-defined nature of the surface units, synthesised separately, is matched by the polyfunctionalisation of the GNPs, allowing the relaxivity and other properties to be correlated to the design.

Results and discussion

Synthesis of a novel gadolinium surface unit

The new chelate **9** was prepared by a straightforward multi-step route (Scheme 1) starting from **5**, generated in three steps from commercially-available cyclen.[46-48] All new compounds (**6** - **9**), were fully characterised by a combination of ^{1}H NMR spectroscopy, ^{13}C{^{1}H}NMR spectroscopy, mass spectrometry, infrared spectroscopy and elemental analysis.

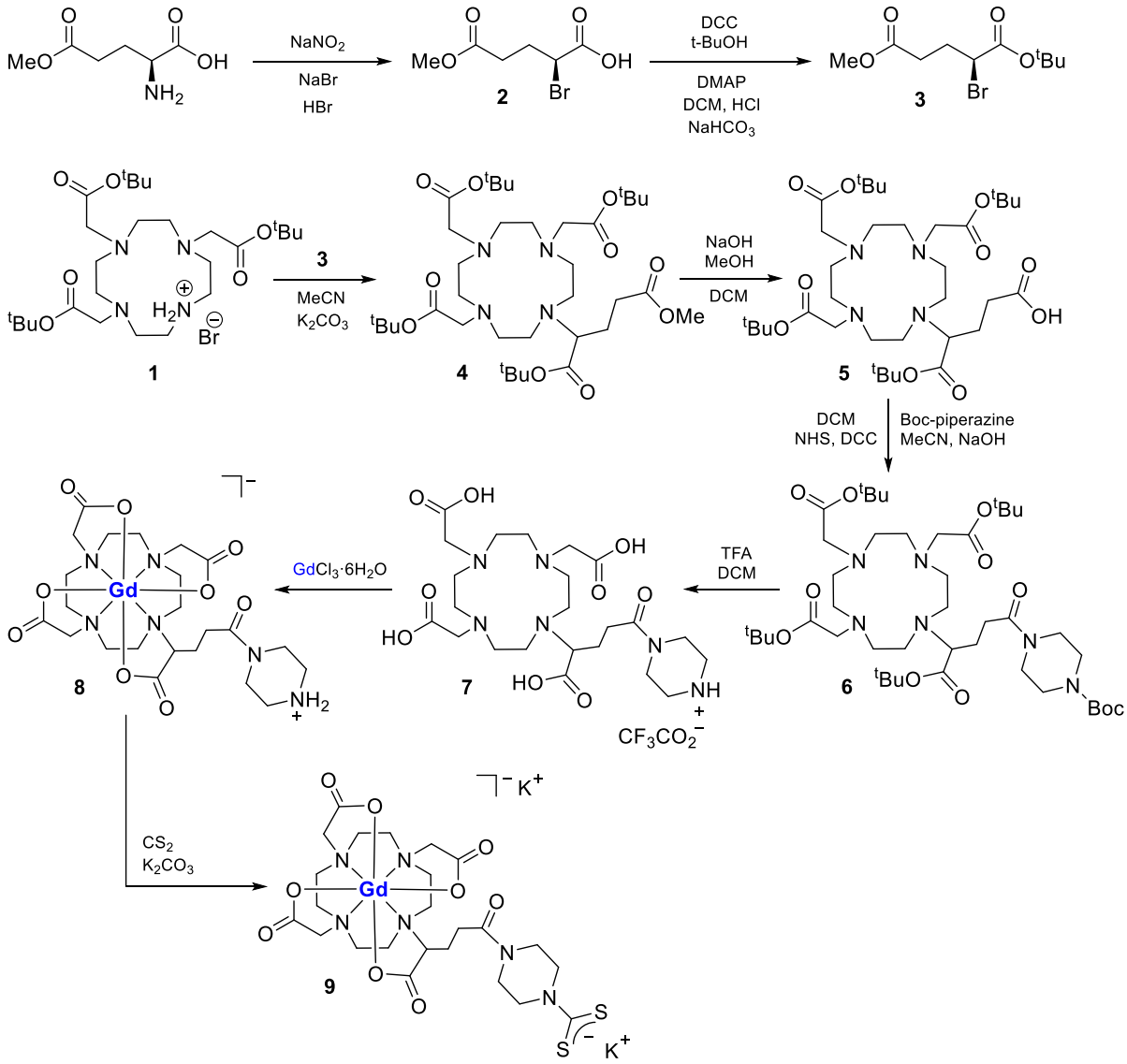

Scheme 1. Synthesis of the new macrocycle **9** from known DOTAGA precursor **5**.

Addition of the gadolinium to **7** was performed using $GdCl_3 \cdot 6H_2O$ and was followed by removal of any free (toxic) gadolinium ions as $Gd(OH)_3$, precipitated under basic conditions (Xylenol orange test). Infrared spectroscopic and mass spectrometry data were consistent with the formation of complex **8** (Scheme 1), which was found to be stable indefinitely as a solid and was prepared on a large scale (> 1 g). It is known that generation of the dithiocarbamate from the amine greatly increases its reactivity so precursor **8** was used for storage of the surface unit. When desired, the addition of K_2CO_3 followed by carbon disulfide, leads to the *in situ* formation of the expected dithiocarbamate moiety (**9**), in line with our previous studies on piperazine-based dithiocarbamate complexes.[35,36,38,44,49-55] High-resolution mass spectrometry confirmed the generation of **9** (*m/z* 812.1283 for $[M+K]^+$), while solid state infrared absorptions measured for **9** attributed to ν(CN) and ν(CS) at 1427 cm^{-1} and 1002 cm^{-1}, respectively,

provided evidence for the formation of the dithiocarbamate. This was reinforced by a resonance at 209.5 ppm in the $^{13}C\{^{1}H\}$NMR spectrum obtained for the diamagnetic lanthanum (La^{3+}, f^{0}) analogue of **9**, formed in an identical fashion.

The performance of **8** as a contrast agent was established using NMRD profiles measured with a 0.25 T fast field-cycling NMR relaxometer (see Supporting Information) and compared to the current clinically-approved standard, Dotarem™ (Fig. 1a). Perhaps due to the slightly higher molecular mass, compound **8** was found to possess a higher relaxivity (Figure 2). The presence of amide arms in the chelate, as present in our previous design (Figure 1c), has been reported to impact negatively on the relaxivity observed.[56] It is therefore noteworthy that the new design described here for **8**, in which the Gd centre is exclusively coordinated by carboxylate arms, exhibits superior relaxivity performance compared to the earlier design.

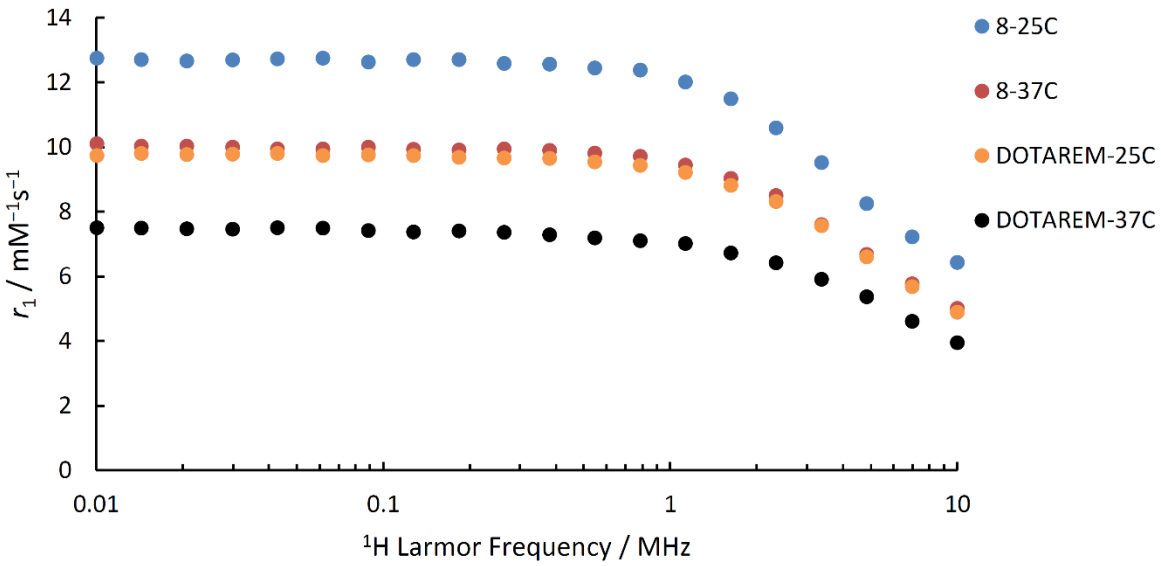

Figure 2. NMRD profiles of compound **8** at 25 and 37 °C and Dotarem™ under the same conditions.

The design of the chelate in **8** and **9** is intentionally closely based on that of Dotarem™, one of the leading clinically-approved contrast agents. Indeed, in contrast to our previous design (Fig. 1c), the anionic nature of the chelate mimics that of Dotarem™ even more closely as well as avoiding the use of an amide arm in the chelate. The stability of the chelate towards loss of gadolinium ions (and hence its toxicity) was therefore expected to be similar to the contrast agents used in the clinic. This was probed by adding Zn^{2+} ions to **8** and monitoring the relaxivity values obtained (Supporting Information), as described by standard literature

protocols.[57] This revealed no change in the relaxivity even after 45 hours of exposure to excess $ZnCl_2$ at 37 °C. Like Dotarem™, fluorescence lifetime measurements for the europium analogue of **8** (compound **10**) revealed the expected hydration value of $q = 1$ for the octadentate chelate (Supporting Information). The assessment of the gadolinium surface unit was continued in cytotoxicity studies. MTT cell viability assays (HeLa cells, 24h) were performed on **8** and showed little or no toxicity even at concentrations as high as 250 μM (Supporting Information).

Targeting and therapeutic units

As well as their stability under a range of physiological conditions, a major advantage of using gold nanoparticles is the ability to combine multiple groups on the surface using complementary, orthogonal attachment approaches.[58] Other platforms, such as molecular systems or liposomes, require substantial modifications to allow new combinations of imaging/targeting/therapeutic units to be incorporated into assemblies of sizes 2-200 nm, resulting in fundamental changes to the design. The nanomaterials reported here combine an imaging modality (MRI) with targeting and biocompatibility/stealth features and also a photoswitchable therapeutic (PDT) unit. The overarching aim of the programme is to construct a library of components (imaging, biocompatibility, targeting, therapy) which can be assembled in a straightforward manner to achieve a nanostructure of tuneable size (*e.g.* 2-200 nm) with the appropriate functionality to target, image and (selectively) kill specific cells.

Targeting groups (aptamers, antibodies *etc.*) can be chosen to recognise specific molecules on the cellular surface that act as early reporters of a given pathology. In a nanoparticle system such as the one reported here, this can enhance the passive targeting of cancerous cells provided by the EPR effect. Both of these targeting approaches would lead to a high concentration of Gd units being present in close proximity to the diseased cells. In the case of receptor-driven targeting, the high concentration of MRI contrast units would compensate for the very low concentration of such receptors (*e.g.* overexpressed membrane receptors) and the relatively low innate sensitivity of Gd(III) contrast agents.[59] Once the location of the GNPs has been identified (due to their localised contrast enhancement) through non-invasive MR imaging, photoexcitation (through the skin or *via* an endoscope) of the highly localised concentration of the photosensitizer immobilised on the surface of the nanoparticles would allow selective destruction of diseased tissue.

In order to explore this targeting concept, a thiol-functionalised folic acid group (FA-SH, **11**) we have previously used[44] was added to the assembly to investigate uptake in HeLa cells, which express folate receptors on their surface to a greater degree than MCF-7 cells.[60]

More complex alternatives, such as DNA/RNA aptamers, can also be used.[12] The modular conjugation of different thiol-based targeting moieties (some of which are commercially-available), tailored to recognise specific proteins or receptors, indicates the versatility of the proposed nanoparticles and their potential use as combined imaging and therapy platforms. The recognition moiety can be chosen based on the specific target and its intra- or extracellular location.

Porphyrins, such as clinically-approved porfimer sodium (Photofrin^{TM}), are well known for their ability to act as photosensitizers in photodynamic therapy (PDT).[61-62] The attachment of porphyrins to GNPs for this purpose has been reported, however, almost all designs feature a thiol, which could detach under demanding conditions (*vide supra*). It was therefore decided to prepare a new, more robust PDT sensitizer unit for attachment to the surface through two contact points. Pioneering work in this area has been performed by Beer and Davis, who reported zinc porphyrin assemblies attached to the surface of gold nanoparticles through both dithiocarbamate[63] and disulfide[64] (dithiolate) tethers for application in sensing.

The known amino-functionalised tetraphenylporphyrin (TPP) **13** was prepared from the parent porphyrin (TPP, **12**) and coupled to lipoic acid to yield the new compound **14** (Scheme 2) which was then metallated with $Zn(OAc)_2$ to afford the zinc-TPP (**15**) in 64% yield from **13**. The new compounds were fully characterised (^{1}H NMR, ^{13}C{^{1}H} NMR and IR spectroscopy, mass spectrometry, elemental analysis and XRD of a derivative – Supporting Information) followed by an investigation of the photophysics of **15**. This revealed an absorption at 420 nm and emission at 650 nm. The disulfide moiety forms a dithiolate on interaction with the gold surface, ensuring a strong attachment of the PDT sensitizer surface unit.

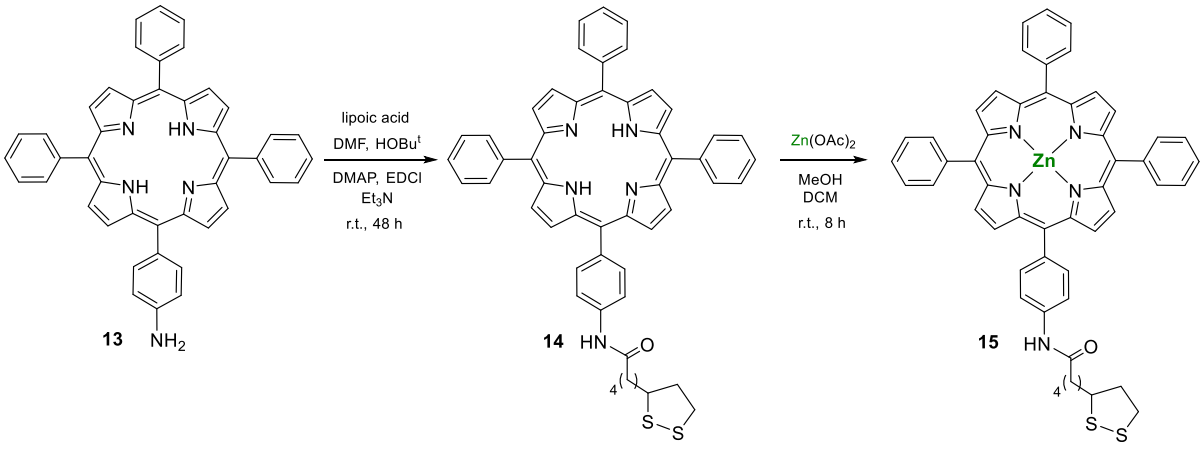

Scheme 2. Synthesis of a zinc porphyrin surface unit, ZnTPP (**15**).

In addition to the surface units described above for delivery of MRI contrast enhancement (**9**) and PDT (**15**), PEG-SH and thioglucose were used to enhance the functionality of the surface architecture. Poly(ethylene)glycol (PEG) units enhance water-solubility and biocompatibility, while thioglucose has been suggested to perform a targeting function for tumours (due to their higher consumption of glucose)[65] as well as conferring water solubility.[66]

Nanoparticle synthesis and functionalisation

By far the most common method of immobilising Gd units on the surface of gold nanoparticles (GNP) is through the use of thiol(ate)s.[67-68] It is often assumed that the strength of the Au-S interaction precludes their loss from the surface, however, recent results[40,69] suggest that the loss of thiol(ate)s from the GNP surface does indeed occur. Due to these assumptions, this loss of surface units is rarely investigated in the studies of GNPs for medical applications and so the extent of this issue remains unclear. The propensity of thiols to form disulfide linkages (rather than attach to the gold surface) has also been reported to hamper the effective design of Gd-functionalised nanoparticles.[67] These issues have led us[33,44] to exploit the strong attachment of dithiocarbamate tethers to the surface of gold nanoparticles[39-41,63,70-86] as the means to attach the gadolinium units. The robust attachment of the MRI contrast unit to the GNP surface is critical, since detachment will impact negatively on the overall relaxivity of the assembly and will undermine the location of the GNP through MR imaging. These considerations led directly to the design of **9** described above, which combines the superior strength of attachment (compared to thiol(ate)s) provided by the dithiocarbamate unit with limited rotational freedom. This rigidity maximises the relaxivity enhancement obtained through the immobilisation of the Gd unit on the nanoparticle, while its similarity to clinically approved Dotarem™ should lead to similar biological properties for the surface units.

A general protocol for the synthesis of gold nanoparticles (Scheme 3) was devised based on the Brust-Schiffrin method.[87] Glassware was washed with *aqua regia* and rinsed thoroughly beforehand. A methanol solution of tetrachloroauric acid was prepared and solutions of the various sulfur-based ligands (**9**, PEG-SH, thioglucose, FA-SH (**11**) and **15**) were then introduced in various ratios (0.01 – 0.5 eq. relative to Au). Ultrapure water was used to dissolve PEG-SH and thioglucose, while ZnTPP (**15**) required the use of DMSO. A 1:1 mixture of ultrapure water and DMSO was used to make a solution of FA-SH and a 1:1 mixture of methanol and acetonitrile was used for **9**. The mixture was cooled to 4 °C and a fresh solution of sodium borohydride in ultrapure water added dropwise to effect reduction from trivalent

gold to Au(0). The mixture was stirred at 10 °C for 3 hours, after which the nanoparticles were then centrifuged at 5300 rpm for 45 minutes. The supernatant was removed and the nanoparticles were rinsed at least 3 times by this method with ultrapure water until the filtrate failed to show the presence of the free Gd chelate ligand (**9**), as determined by measurement of relaxivity.

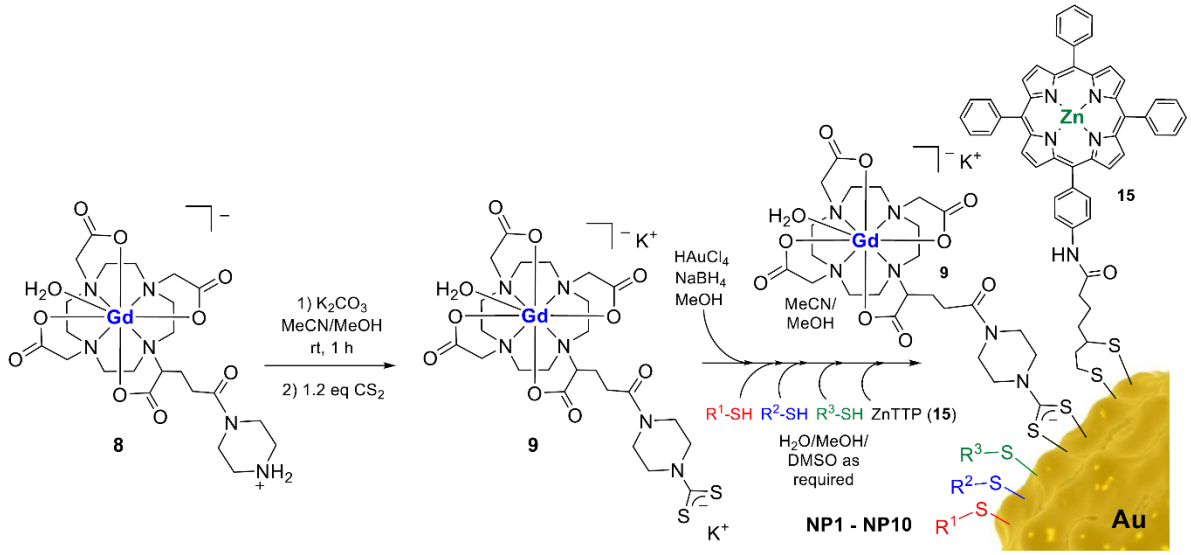

Scheme 3. Synthesis of GNPs with **9**, **15** and various surface units (R^1-SH, R^2-SH, R^3-SH).

A total of 10 functionalised GNPs were prepared in a modular fashion with up to five different surface units (Figure 3). In addition, the use of three different attachment approaches (DTC/dithiolate/monothiolate) ensures that the 'payload' of the most significant Gd (**9**) and ZnTPP (**15**) units is maintained by the strong attachment of the dithiocarbamate and dithiolate (respectively) relative to the weaker thiolate Au-S bonds used for other surface features.

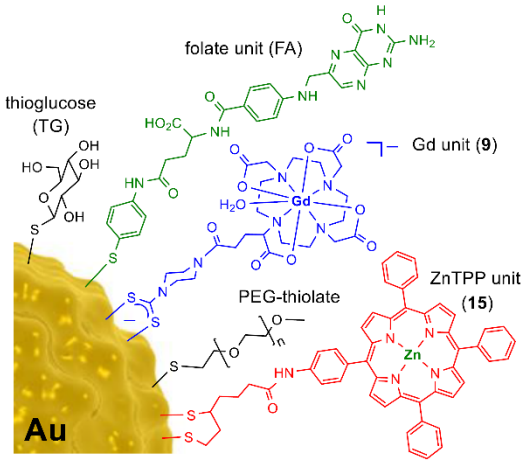

	Au	Gd (**9**)	PEG	TG	FA	ZnTPP (**15**)
NP1	1	1	-	-	-	-
NP2	1	1	0.05	-	-	-
NP3	1	1	0.05	0.05	-	-
NP4	1	1	0.05	-	0.01	-
NP5	1	1	0.05	0.05	0.01	-
NP6	1	1	-	-	-	0.5
NP7	1	1	0.05	-	-	0.5
NP8	1	1	0.05	0.05	-	0.5
NP9	1	1	0.05	-	0.05	0.5
NP10	1	1	0.05	0.05	0.05	0.5

Figure 3. Nanoparticle surface functionalisation with proportions used in the direct synthesis.

This approach represents a rapid, straightforward and versatile route to the modular preparation of multifunctional gold nanoparticles. The greater strength of attachment (compared to thiolates) of the DTC unit (**9**) ensures the presence of the Gd contrast agent, while the use of a disulfide unit for the PDT unit (**15**) helps prevent loss of the therapeutic unit. All surface units were added to the reaction mixture at the same, providing them all with the opportunity to bind to the nanoparticle surface. Thermogravimetric analysis (TGA) was performed (Supporting Information, Section S6) in an attempt to quantify the surface units through loss of mass. However, it was found that no distinct mass loss could be attributed to specific surface units. Similarly, solid-state infrared spectroscopy (Supporting Information, Section S6.1) was not able to distinguish between the surface units due to their many shared features, such as C-O and C=O absorptions. All surface units were added in large excess, with respect to the number of gold surface atoms so, although the values in Figure 3 do not represent final amounts present on the nanoparticle surface, it is likely that all surface units added are represented on the nanoparticle. This is reflected in the different relaxivity and cell uptake behaviour observed (*vide infra*). Once corrected for diameter, it was found that the use of increasing numbers of additional surface units causes a decrease in the number of gadolinium chelates on the surface of the GNPs, as determined by ICP-OES (Supporting Information, Table S9-1). This suggests that the additional surface units are successfully competing for some of the surface area, causing fewer Gd units to be present.

Transmission electron microscopy (TEM) was used to determine the diameter and size distribution of the nanoparticles (Figure 4). This revealed a size distribution of between 2.6 and 4.1 nm in diameter with the different surface units exerting a subtle effect on the sizes obtained. The particles displayed a reasonably narrow size distribution but were not monodisperse (Table S9-1 in Supporting Information), though the variation in size was not expected to have any significant impact on their performance. Dynamic light scattering (DLS) measurements for **NP5** and **NP7** suggested that the hydrodynamic radius increases from 2.6 - 4.1 nm to approximately 20 nm due to the PEGylated thiolate surface units (PEG-2000). Energy Dispersive X-ray spectroscopy (EDS) was used to identify the presence of Gd, Au and Zn (where present) in the assembly (Figure 4). The ratio of Gd, Au and Zn was more accurately determined by inductively-coupled plasma optical emission spectroscopy (ICP-OES) and allowed the number of Gd units per GNP to be calculated and used for relaxivity measurements. TGA for **NP1** (just **9** on the surface) was found to be in good agreement with the ICP-OES results. Calculations based on the TEM and ICP-OES data for **NP1** led to the estimation of

between 179 (ICP) and 206 (TGA) Gd units (of **9**) per nanoparticle. As no other surface units are present, this can be assumed to be close to the maximum possible loading of Gd units for this diameter of nanoparticle.

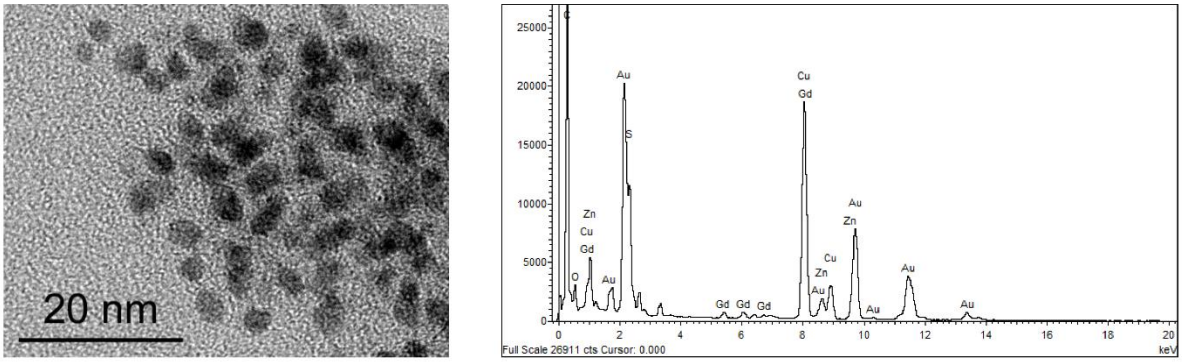

Figure 4. TEM (left) and EDS (right) data for **NP10**.

The surface plasmon resonance (SPR) band was observed in the UV-vis spectrum recorded for each assembly at approximately 550 nm, in agreement with the 2.6 - 4.1 nm size of the gold core. Zetapotential values ranging between −39.8 and −32.8 (Supporting Information) were measured, indicating good stability and resistance to agglomeration. The nanoparticles were also found to be stable in solution across a range of pH values between 4 – 10 (HEPES buffer solution) over a 24 h period. The stability in the presence of NaCl was tested in water and monitored by UV-vis spectroscopy, showing no tendency to precipitate over a period of 24 h. The same technique was used to analyse their behaviour in biological media, which revealed no changes to the data. See Supporting Information for further details.

Relaxivity studies

With a series of 10 gold nanoparticles functionalised with a range of different surface units to hand, the relaxivity of the nanoparticles was measured and NMRD profiles determined. The immobilisation of gadolinium units on a polymer or nanoparticle surface has often been employed in order to enhance the relaxivity of the individual Gd units as well as the whole assembly.[66,68] This effect can be traced to the slow tumbling of the much larger unit and a reduction in the rotational freedom experienced by each individual Gd unit. The materials prepared in this study exhibited a particularly pronounced enhancement of up to 8 times higher relaxivity per Gd centre. Part of this boost can be attributed to the rigid nature of the dithiocarbamate attachment of chelate **9** to the gold surface, preventing the rotation about either

the C-N (multiple bond character) or Au-S bonds. This is demonstrated in the NMRD profile of **NP1** shown in Figure 5. Designs in which the chelates are attached to the surface through a thiol(ate) tether inevitably allow rotation about the axis of the tether and the Au-S interaction.[59] The formation of unwanted disulfide linkages has also been observed which creates flexible chains of Gd units anchored at only a few points to the surface.[67] Many reports use long PEG-thiolate chains terminated in a Gd unit, which retain their internal flexibility and so restrict the enhancement observed.[32,68,88-91] When combined, these effects undermine to some degree the benefit of immobilisation on the nanoparticle surface but this is easily overlooked when relaxivity is quoted per nanoparticle rather than per Gd centre.

The effect of immobilising the Gd unit on the nanoparticles is clearly demonstrated by the relaxivity performance of **NP1**. These nanoparticles display a 6.3-fold contrast enhancement (**NP1**) **per Gd unit** over non-immobilised **8** (r_1 = 5.01 mM^{-1} s^{-1} at 10 MHz, 37 °C), as can be seen from the NMRD profile shown in Figure 5. This represents a relaxivity per Gd unit of r_1 = 31.68 mM^{-1} s^{-1} and per nanoparticle of r_1 = 5691 mM^{-1} s^{-1} for **NP1** (both at 10 MHz, 37 °C). This is one of the highest relaxivity enhancements per Gd ion yet reported for gold nanoparticles that could potentially be used in a clinical setting. A slightly higher value (r_1 ~ 40 mM^{-1} s^{-1} at 10 MHz, 37 °C) was reported by Helm and co-workers[68] for gold nanoparticles with a surface unit based on a heptadentate chelate with two coordinated water molecules (q = 2). The lower than usual coordination number with this polydentate chelate make this suitable for pre-clinical but not clinical imaging (nephrogenic systemic fibrosis concerns). The enhanced performance of **NP1** can be attributed to the internal rigidity of the surface unit provided by the multiple bond character present in the C-N bonds of the dithiocarbamate and the dual Au-S attachment at the surface (compared to a single Au-S attachment for thiolates). The flexibility of the tether attaching the surface unit to the surface has been identified[92] as the main factor limiting the relaxivity enhancement on immobilising Gd units to the surface of gold nanoparticles.

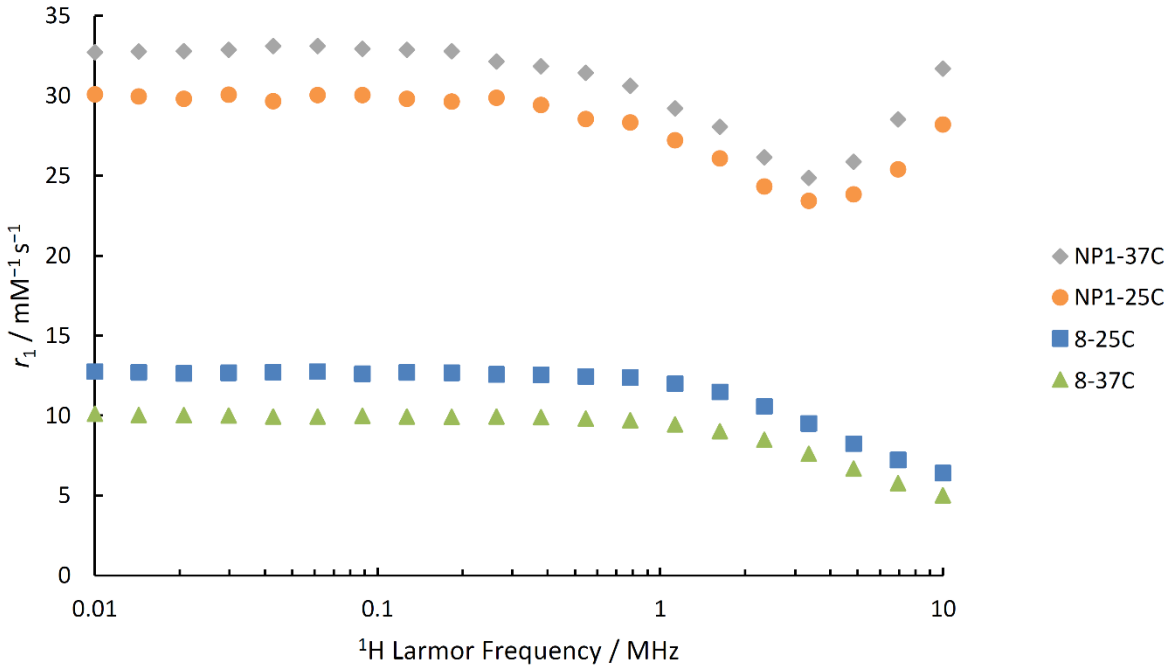

Figure 5. NMRD profiles of **NP1** and **8** at 25 and 37 °C.

The addition of PEG-SH units improves both the solubility of the GNPs in biological media and also enhances their biocompatibility by performing a 'stealth' function. This is a crucial factor in any clinical application as it prevents premature removal by macrophages.[93] Using a similar procedure to that employed for the synthesis of **NP1**, a series of materials with mixed surface units was prepared (Scheme 3), using just PEG-SH and the Gd unit (**NP2**). This led to a small reduction in relaxivity per Gd ion possibly due to crowding of the Gd centres by the PEG units, reducing their exposure to the bulk water.

In addition to **9**, thioglucose was also added in equimolar amounts to PEG-SH to generate **NP3**, which resulted in a triply functionalised surface. Two further PEGylated assemblies were functionalised with the thiol-modified derivative of folic acid (FA-SH, **11**) reported previously[44] with no thioglucose (**NP4**) and an assembly (**NP5**) with PEG-SH, thioglucose and folic acid (FA-SH) (Scheme 3 and Figure 3).

Monometallic Gd-based contrast agents, such as clinically-approved Dotarem™ (Figure 1) are hampered by the adverse effect on their relaxivity caused by their associated short rotational correlation time. Increasing the temperature leads to more rapid tumbling and causes a decrease in the r_1 value, despite the higher water exchange rate at elevated temperatures. For Gd units immobilised on nanoparticles, slower tumbling is indeed achieved, however, the potential for enhancement is reduced by undesirable internal rotation, often about

the axis of the tether. The rigidity introduced by the dithiocarbamate in our system means that an increase in temperature has little impact on the rotation of the Gd surface unit, while still allowing the beneficial effects of a higher water exchange rate. This can be seen in Figure 6, which plots the relaxation rate (R_1) at temperatures between 30 – 70 °C divided by the value at 30 °C (at 7 MHz) for monometallic **8** and **NP1**. This reveals the expected decrease in values for **8**, while the corresponding values for **NP1** show an increase in relaxation rate.

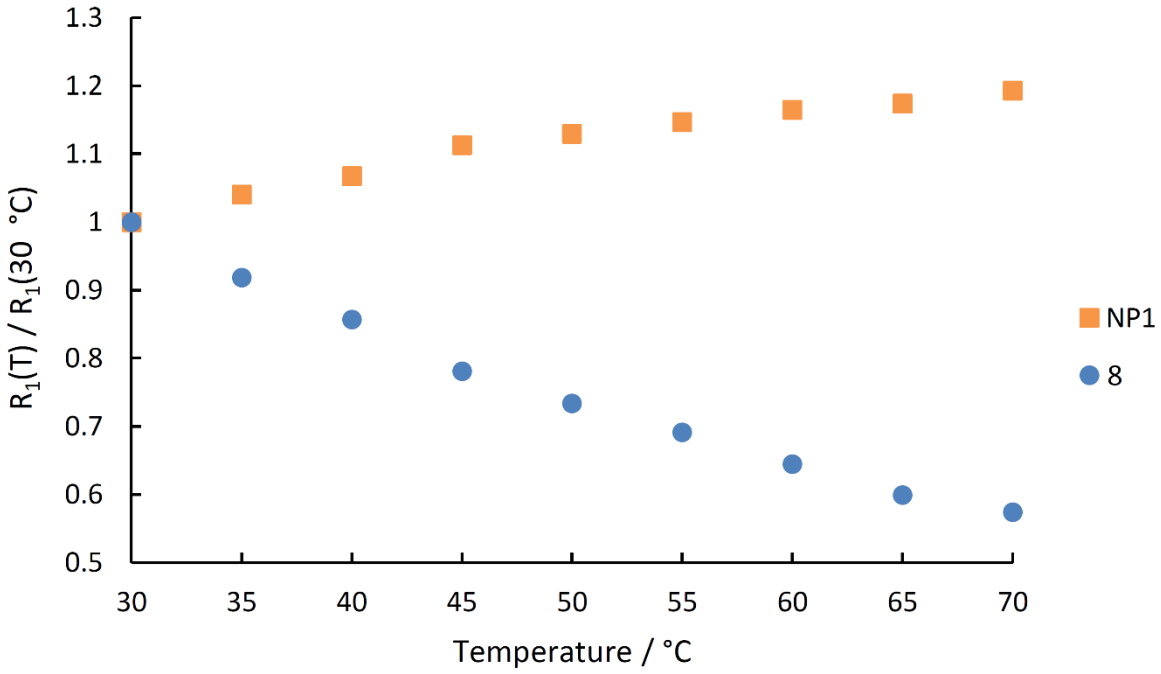

Figure 6. Plot of the ratio of relaxation rate (R_1) at temperatures between 30 – 70 °C compared to the value at 30 °C (at 7 MHz) of monometallic **8** and **NP1**.

With the very promising performance of the Gd unit (**9**) confirmed along with the demonstration that four different surface units can be attached to the surface, the focus moved to investigating the relaxivity performance with multiple surface units, including one providing a therapeutic action (ZnTPP, **15**).

As a control, an assembly (**NP6**) was prepared with only Gd (**9**) and ZnTPP (**15**). While EDS confirmed the presence of both Gd and Zn, the distribution of the two surface units was determined to be a 2:5 ratio of Gd and Zn by ICP-OES. This material displayed good relaxivity at 10 MHz and 37 °C both per Gd ion (42.21 mM^{-1} s^{-1}) and overall (3713 mM^{-1} s^{-1}) and is the best performance *per Gd unit* reported for any comparable (q = 1) chelate. The addition of PEG

surface units to aid biocompatibility (**NP7**) did not undermine the relaxivity performance substantially.

While it would be expected that the increase in complexity of the surface architecture must impact on the overall relaxivity per NP, the overall enhancement compared to Dotarem™ or compound **8** is still substantial. Less easy to predict is the impact on the relaxivity performance per Gd unit. As can be seen in the relaxivity *per Gd unit* recorded at 37 °C (Figure 7), the performance of **NP1** (only Gd units) is similar to that of **NP2** (Gd and PEG units), suggesting that the presence of PEG units has no specific effect. As has been noted previously,[66,94] the presence of thioglucose seems to enhance the relaxivity, possibly through the small size of the thioglucose units relieving the crowding of the Gd units, allowing better interaction with the bulk water. This is reflected in the increase for **NP3** (Gd, PEG and thioglucose units), however, the presence of folic acid units seems to have a detrimental effect on the r_1 values per Gd, as observed for **NP4** (Gd, PEG and folic acid units) and **NP5** (Gd, PEG, thioglucose and folic acid units). The addition of the ZnTPP unit (**15**) for **NP6** – **NP10** seems to lead to an enhancement, perhaps due to these bulky groups reducing the flexibility of the Gd units (**9**) still further. The enhancement of relaxivity *per Gd unit* on increasing the temperature from 25 °C to 37 °C (Section S6 in the Supporting Information) was seen for all nanoparticles whereas the r_1 value for the Gd unit itself (**8**) dropped, as is typical for small molecular weight monometallic Gd complexes. This can be traced to the greater rigidity afforded by the dithiocarbamate and the piperazine tether in our design. This is in agreement with our results for other DTC-based Gd units but is in stark contrast to the poorer performance at higher temperature exhibited by GNPs decorated with more flexible Gd units.[32,68,88-91] At 25 °C, the best performance is found for the same four nanoparticles (**NP3**, **NP6**, **NP7**, **NP8**), while the performance of the nanoparticles functionalised with folic acid is again the lowest.

Figure 7. NMRD profiles of **NP1 - NP10** and compound **8** in the study *per Gd unit* shown at 37 °C.

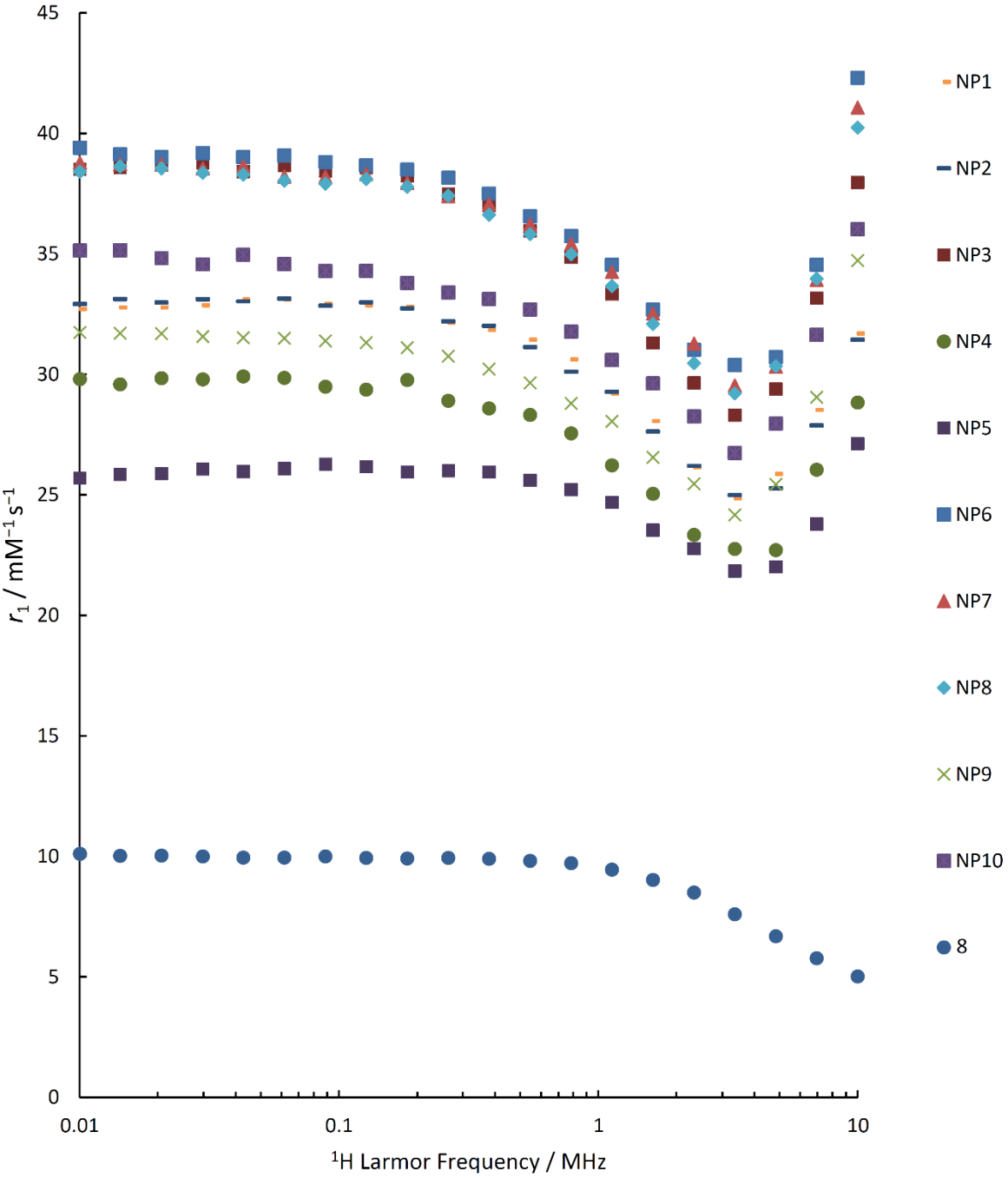

Figure 7. NMRD profiles of **NP1 - NP10** and compound **8** in the study *per Gd unit* shown at 37 °C.

The use of additional surface units for other functions (biocompatibility, targeting, therapy *etc.*) should lead to a reduction in the overall relaxivity per nanoparticle due to fewer Gd units being present. This is evident in Figure 8, with **NP1** (only Gd units), registering the highest overall relaxivity values and **NP10** (containing all 5 surface units) showing the lowest

relaxivity per nanoparticle. The overall r_1 value per nanoparticle decreases from 5691 mM^{-1} s^{-1} for **NP1** to 2090 mM^{-1} s^{-1} for **NP10** (both at 10 MHz, 37 °C). However, these changes must also be viewed in terms of the differences in nanoparticle diameter, which range from 2.6 - 4.1 nm, which will have an impact on the loading of Gd ions on the surface. Compared to the diffuse and non-localised effect of monometallic species such as Dotarem™, the high local concentration of Gd ions created by their manifold presence on the nanoparticle will lead to a great localised contrast enhancement, even for the uptake of a single nanoparticle. Uptake and selectivity can be enhanced by the other surface units, leading to targeting of the high Gd payload to a tumour, for example. The contrast enhancement observed would thus be extremely large for even a single receptor (compared to a targeting unit linked to one or only a few Gd centres). In addition to their high localised relaxivity, the small diameters of the nanoparticles described here should allow good membrane penetration and cellular uptake.

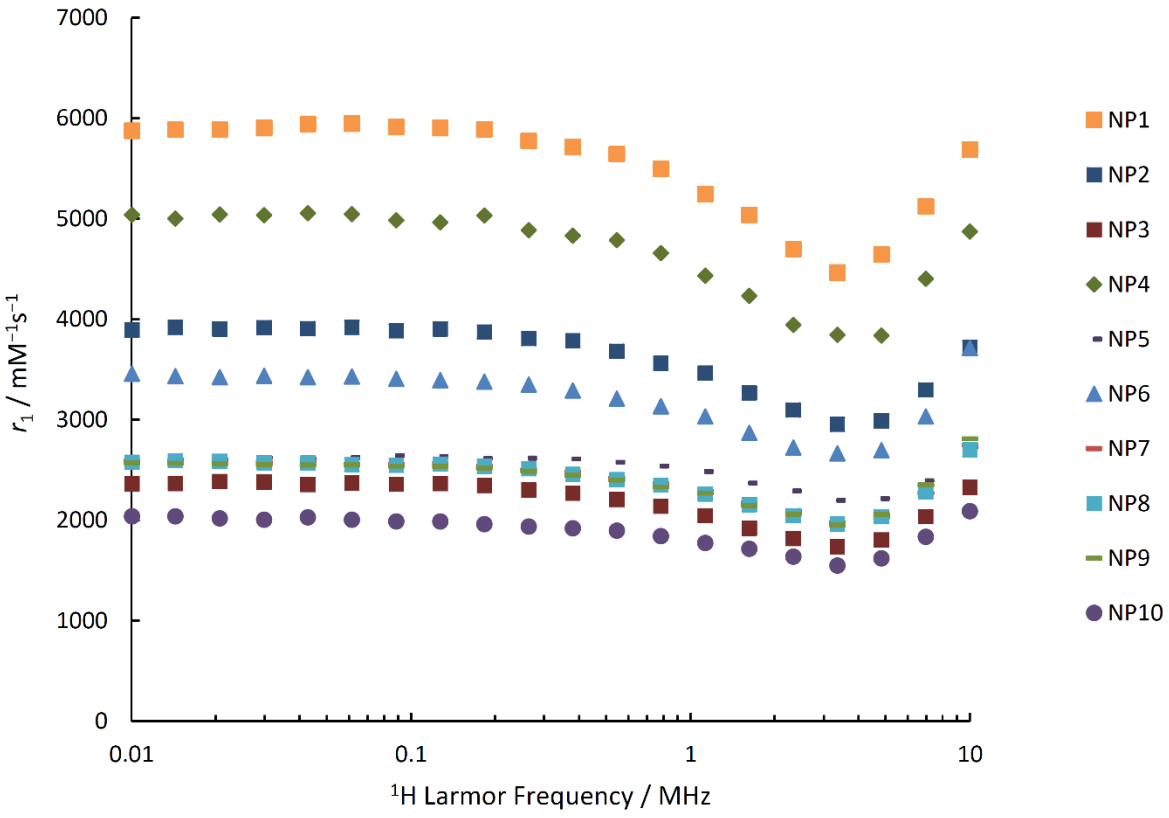

Figure 8. NMRD profiles of **NP1** – **NP10** as measured *per nanoparticle* at 37 °C.

Table 1. Summary of relaxivity values (measured at 10 MHz at 37 °C).

	r_1 per Gd / mM^{-1} s^{-1}	r_1 per NP / mM^{-1} s^{-1}
NP1	31.68	5691
NP2	31.44	3719
NP3	37.96	2330
NP4	28.83	4874
NP5	29.13	2932
NP6	42.21	3713
NP7	40.88	2749
NP8	40.24	2702
NP9	34.72	2810
NP10	37.01	2090
8	5.01	-
Dotarem™	3.94	-

Magnetic resonance imaging

The GNPs were imaged on a 1.5 T MRI Scanner (Ingenia, Philips) used for patients at St. Thomas' Hospital, London, UK, in order to investigate their contrast enhancing performance at a clinical magnetic field strength. Phantom imaging was carried out using solutions of the GNPs in Eppendorf tubes, which demonstrated the ability of the nanoparticles to deliver a contrast enhancement far superior to that of Dotarem™ and at a gadolinium concentration of only 0.02 mM. Clinical administration of Dotarem™ is typically set at 0.1 mmol/ kg, which represents a much higher concentration. Unsurprisingly, the relaxivities (per Gd unit) of the GNPs were far greater than the control of Dotarem™, which displayed a relaxivity of 4.6 ± 0.3 mM^{-1} s^{-1}. The relaxivities of the GNPs at 1.5 T were all similar in magnitude with values ranging from 25 ± 1 mM^{-1} s^{-1} (**NP5**) to 31 ± 3 mM^{-1} s^{-1} (**NP6**) per gadolinium unit (Figure 9). These values represent an increase in relaxivity between 5 and 7 times higher than Dotarem™. Figure 10 summarises the relaxivity performance of these GNPs over all frequencies recorded.

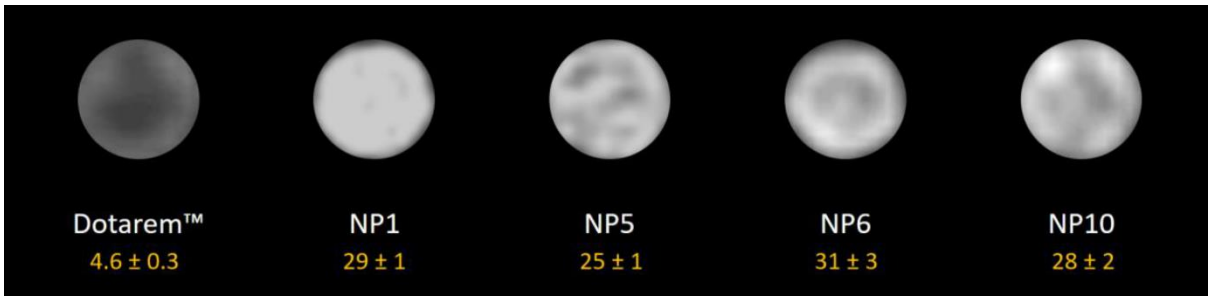

Figure 9. MR images and relaxivity values (per Gd unit, in mM^{-1} s^{-1}) for Dotarem™, **NP1**, **NP5**, **NP6** and **NP10** (1.5 T, 63.87 MHz 25 °C, $[Gd^{3+}]$ = 0.02 mM in all cases).

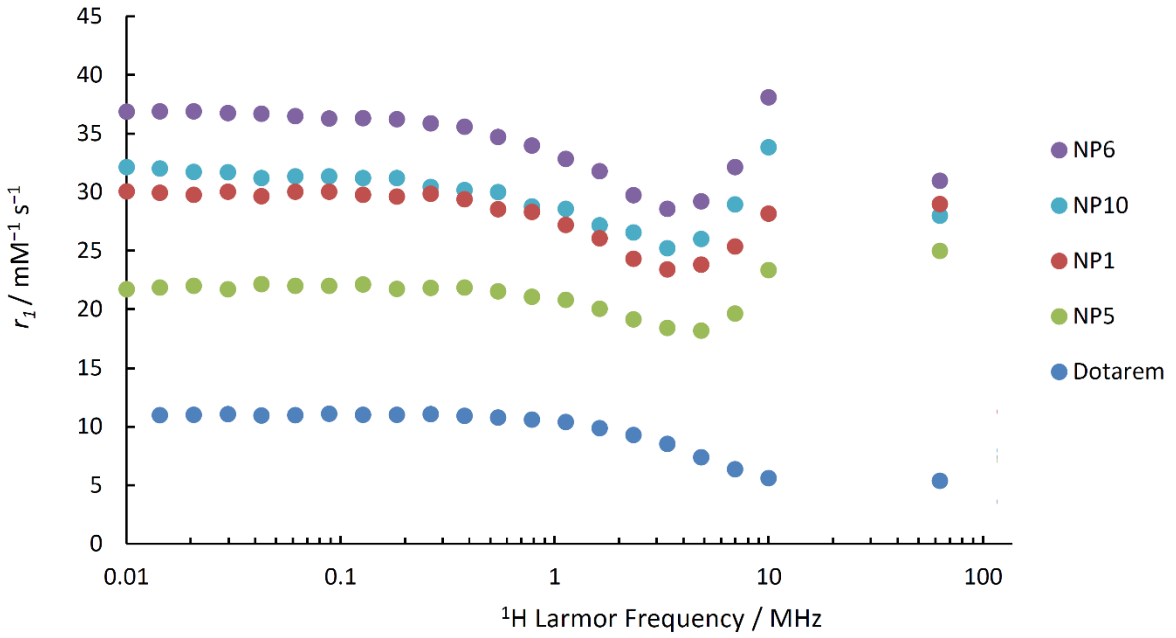

Figure 10. NMRD profiles of Dotarem™, **NP1**, **NP5**, **NP6** and **NP10** (at 25 °C) showing relaxivity behaviour (per Gd unit, in mM^{-1} s^{-1}) between 0.01 MHz and 63.87 MHz (clinical field).

The gadolinium chelate reported here (Fig. 1d, compound **9**) represents an improvement in design compared to that reported previously (**Au@DO3A-CS2**, Fig. 1c)[44] as it is negatively charged and possesses only carboxylate arms, making it directly comparable to clinically-approved Dotarem™. The relaxivities of the nanoparticle-bound chelates shown in Figures 1c and 1d (**9**) are comparable at low magnetic field strengths (0.25 mT – 0.25 T, 0.01 MHz – 10 MHz) but at a clinically-relevant magnetic field strength of 1.5 T, the new chelate (**9**) performs substantially better when attached to the GNP, with a relaxivity 24% higher than the **Au@DO3A-CS2** design shown in Figure 1c (29 mM^{-1} s^{-1} *versus* 22 mM^{-1} s^{-1}, respectively). It is possible that due to closer packing of **9** on the nanoparticle surface (2.6 chelates per nm^2 *versus* 1.6 chelates per nm^2 from ICP-OES and TEM data), their motion is restricted more effectively, causing the relaxivity to increase.

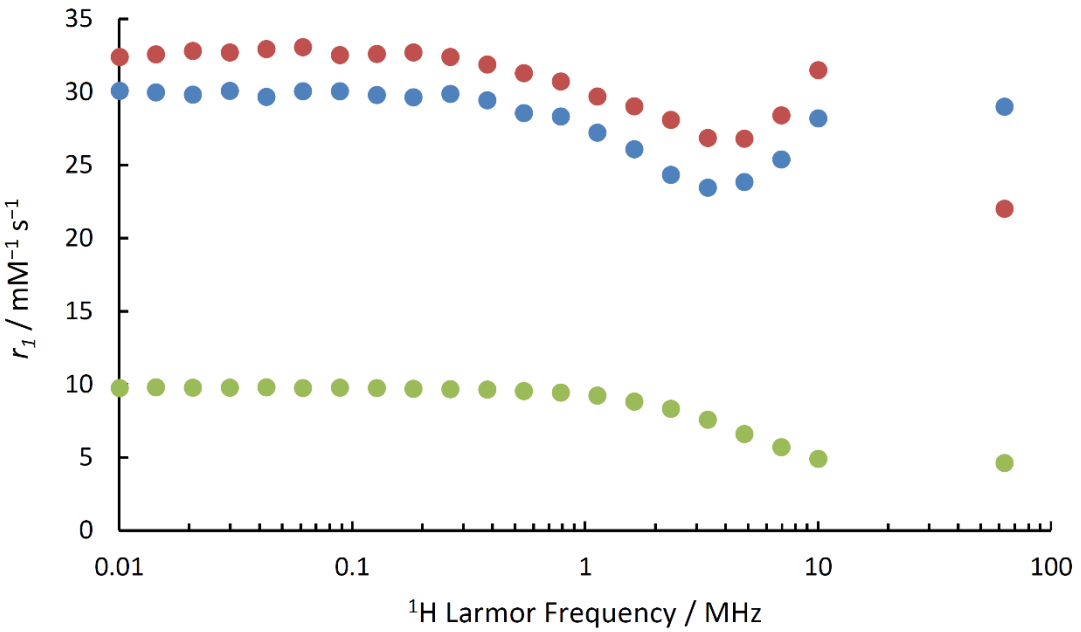

Figure 11. NMRD profiles of Dotarem™, **NP1** and **Au@DO3A-CS$_2$** (at 25 °C) showing relaxivity behaviour (per Gd unit, in mM^{-1} s^{-1}) between 0.01 MHz and 63.87 MHz (1.5 T clinical field).

Cell uptake and PDT studies

The GNPs were found to be non-cytotoxic towards cancerous (HeLa and MCF-7) cell lines at gold concentrations up to 250 μM (Supporting Information). Measurement of GNP uptake inside cells (HeLa and MCF-7) was determined after incubation for 1, 6 and 24 hours with the differently functionalised GNPs. The nanoparticles were detected inside the cells (ICP-OES, Supporting Information) at varying concentrations, depending on the incubation time and composition of the GNP, as shown in Figure 12.

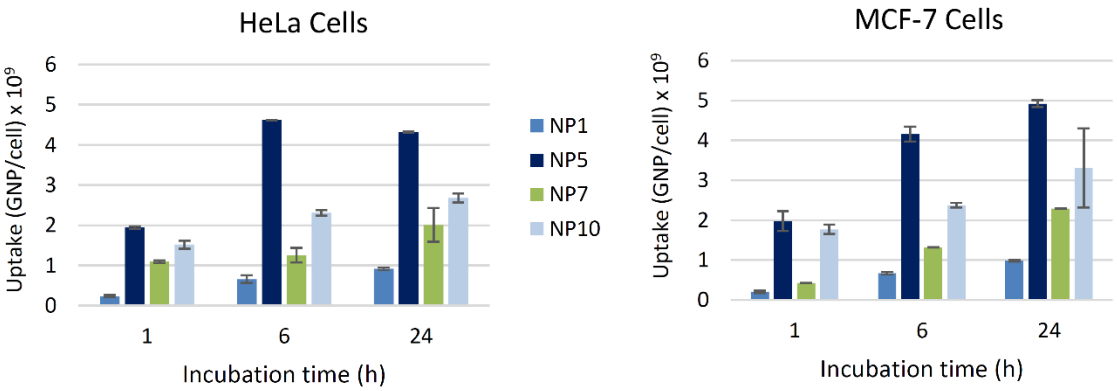

Figure 12. Cell uptake studies performed with **NP1**, **NP5**, **NP7** and **NP10** (200 μM) over various incubation times for HeLa (left) and MCF-7 cells (right).

The data in Figure 12 show that the nanoparticles functionalised with PEG, thioglucose and folic acid (**NP5**) show much greater uptake after 6 and 24 hours than the material with only Gd units (**NP1**). The presence of PEG is known to decrease or delay uptake of nanoparticles by cells, however, a comparison of **NP1** with **NP2** and **NP6** with **NP7** (given the associated error) reveals no such behaviour in this case. The addition of the ZnTPP unit (**15**) appears to hinder the uptake (**NP7** and **NP10**), however, the presence of PEG, thioglucose and folic acid surface units ameliorates this effect. HeLa cells express the folate receptor to a greater extent than MCF-7 cells,[95-97] however, it is the combination of folic acid and thioglucose that appears to lead to the greatly enhanced uptake of **NP5** (particularly after 6 h, where there was a significant difference in uptake between HeLa and MCF-7 cells ($p < 0.025$)).

A widefield microscope (FILM, Imperial College) with an LED operating at 570 nm was used to investigate the photodynamic therapeutic effect (in HeLa cells) of the GNPs bearing ZnTPP surface units. Using 200 μM concentrations of **NP7** (Gd, PEG and ZnTPP) and **NP10** (Gd, PEG, thioglucose, folic acid and ZnTPP), the effect of the surface functionality on the cellular uptake and performance in PDT was assessed. Since the cytotoxic effect of singlet oxygen is only effective when generated within the cell, the greater uptake of **NP10** compared to **NP7** should render this assembly more effective. This is indeed observed in Figure 13, where the control is provided by irradiation of the cells in the absence of nanoparticles. After 5 minutes of irradiation at 570 nm, a decrease in cell viability of around 50% was observed for **NP10** and only 10% for **NP7**. After 15 minutes of irradiation, the cells incubated with **NP10** showed a much lower viability of 35% while the **NP7** experiment displayed a more modest decrease to 58% cell viability. These results can be taken as an illustration of the need for sufficient cellular uptake to achieve a significant therapeutic effect. Irradiation for 30 minutes in total led to a final cell viability value of around 25% with **NP10**.

Figure 13. Cell viability of HeLa cells after irradiation with laser light (570 nm) for 5, 15 and 30 minutes following incubation with **NP7**, **NP10** (200 μM) or no nanoparticles (control).

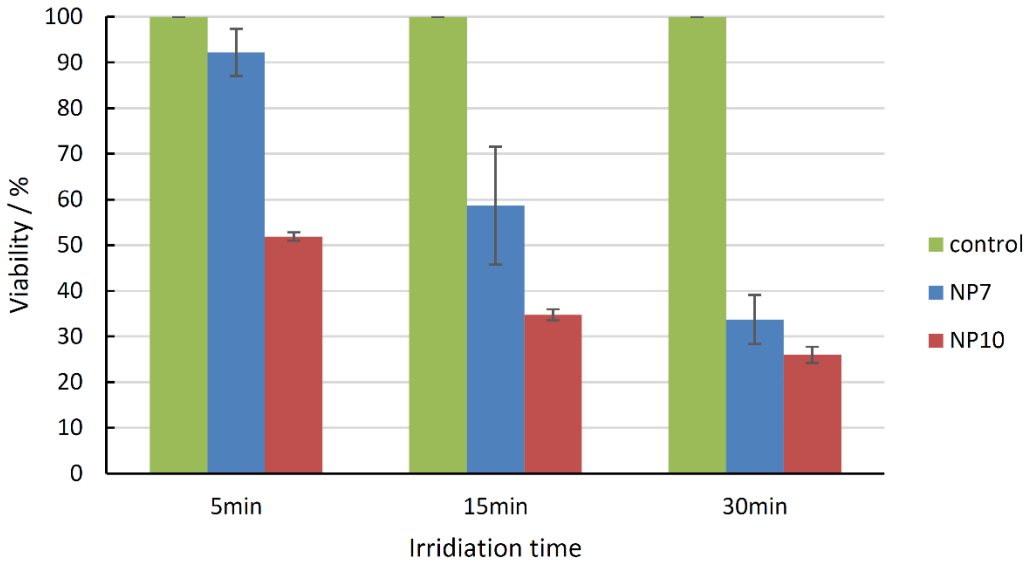

Figure 13. Cell viability of HeLa cells after irradiation with laser light (570 nm) for 5, 15 and 30 minutes following incubation with **NP7**, **NP10** (200 μM) or no nanoparticles (control)

Conclusions

This contribution illustrates how a straightforward synthetic strategy combining orthogonal tethering approaches can be used to prepare a series of nanoparticles functionalised with up to 5 different surfaces units. The increasing strength of the thiolate/dithiolate/dithiocarbamate interactions ensure that the key surface units responsible for imaging and therapy are retained. In this work, the powerful enhancement effect on relaxivity *per Gd unit* of immobilising trivalent gadolinium complexes on the nanoparticle surface is clearly shown. In order to achieve this, a new, non-toxic, anionic, octadentate Gd surface unit (**9**) has been designed and prepared in multigram quantities based on the clinically-approved DOTA scaffold (q = 1). The limited flexibility of the tether is key to the enhanced relaxivity observed and this is achieved through the multiple bond character of the dithiocarbamate C-N bond and the attachment of this 1,1'-dithiolate ligand at two points of the gold surface. An enhancement of up to 8 times is observed per Gd unit (comparing unattached **8** to **NP6** at 10 MHz and 37 °C) and the overall assembly displays r_1 values of up to 5691 mM^{-1} s^{-1} per nanoparticle (**NP1**). In contrast to monometallic (*e.g.* Dotarem™) or Gd units immobilised on nanoparticles or polymers where internal rotation is possible, an increase in temperature (as observed between 25 and 37 °C) results in an increase in r_1 values and this is attributed to the combination of the rigidity in our system and the improved water exchange rate at elevated temperatures. Compared to our previous design,[44] the fully functionalised assembly (**NP10**) displays better relaxivity both per

Gd and overall (particularly at 63.87 MHz, 1.5 T clinical field), despite more flexibility in the tether. Any loss of relaxivity from lower rigidity appears to be counteracted by more efficient packing, leading to a better loading of surface units.

Since tumours often express only a few receptors, the targeting of these receptors with a huge payload of Gd units will help locate diseased tissue through a vastly improved MRI signal. The accumulation of gold nanoparticles in tumours (EPR effect) is enhanced by the inclusion of a unit capable of actively targeting folate receptors, which are overexpressed by HeLa cells. It appears that the combination of thioglucose and folic acid (FA-SH) units leads to a slight increase in cellular uptake in HeLa cells compared to a cell line (MCF-7) where the folate receptor is expressed less.[96,97]

The nanomaterials prepared in this study are stable over a wide range of pH, salt concentrations (NaCl) and towards transmetallation (with Zn^{2+} ions) of the Gd surface units. They are all non-toxic, even at concentrations similar to those used clinically (250 μM), however, on irradiation with light, the nanoparticles functionalised with the novel ZnTPP unit (**15**) display the ability to kill 75% of HeLa cells in 30 minutes. This provides a proof of principle for these materials being used both to evaluate disease progression and also deliver a photo-switchable and localised therapeutic intervention.[98] The work described here has provided a new methodology for functionalising nanoparticles, which have the potential to deliver targeted (and hence lower dose) imaging/therapeutic agents. In any future clinical translation of such materials, the ability to image the localisation of the contrast agent and then apply light-driven therapy would represent a key advance in limiting the side effects associated with traditional chemotherapy drugs. In particular, the ability to only 'switch on' the cytotoxic effect (through the skin or via endoscope) when needed would allow targeting of the therapy and less collateral damage.

Methods

Materials and Equipment

All chemicals and solvents were purchased from Alfa-Aesar, Sigma-Aldrich and VWR and were used without further purification, unless otherwise stated. All experiments and manipulations of compounds were conducted in air, unless otherwise specified. Solvent mixtures are volume/volume mixtures. A Waters LCT Premier ES-ToF (ESI) spectrometer was used for electrospray and high-resolution mass spectra (accurate mass mode). Standard FTIR spectra were measured using a Perkin Elmer Spectrum GX spectrometer. UV-Vis spectra were

recorded with a Perkin Elmer Lambda-20 spectrophotometer. Fluorescence measurements in solution were carried out using an Agilent (Varian) Cary Eclipse spectrofluorimeter. NMR spectroscopy was performed at 25 °C using a Bruker AV400 or 500MHz spectrometer at room temperature in $CDCl_3$ unless otherwise stated. The widefield microscopy was carried out using a Zeiss Axio Observer inverted microscope. TEM images and EDS data were obtained using a JEOL 2010 high-resolution TEM (80-200 kV) equipped with an Oxford Instruments INCA EDS 80mm X-Max detector system. Thermogravimetric analysis was performed on a Mettler Toledo DSC 1LF/UMX Thermogravimetric Analyser. ICP-OES analyses were performed using a Perkin-Elmer OPTIMA 2000 DV ICP-OES spectrometer. Zeta-potential & DLS analyses were carried out on a Zetasizer Nano ZS90 DLS system (Malvern Instrument Ltd, England). NMRD profiles were recorded using a SMARtracer™ 0.25 T bench-top fast field cycling NMR relaxometer (Stelar).

Synthesis of functionalised nanoparticles

In a flask pre-washed with *aqua regia* and thoroughly rinsed with ultrapure water was introduced $HAuCl_4$ (59 mg, 0.150 mmol, 1 eq.) in methanol (13 mL). The sulfur-based ligands (PEG-SH, thioglucose, **9**, **15**) were then introduced at the desired quantities (0.01 - 1 eq. relative to Au) in solution (ultrapure water for PEG-SH and thioglucose, a 1:1 mixture of methanol and acetonitrile for ZnTPP (**15**) and a 1:1 mixture of ultrapure water and DMSO for compound **8**. The mixture was then cooled down to 4 °C with an ice bath for at least 10 minutes. A fresh solution of sodium borohydride (47.3 mg, 1.252 mmol, 8.4 eq.) in 3.3 mL of ultrapure water was then added dropwise. The mixture was stirred at 10 °C for 3 hours. The nanoparticles were then centrifuged at 5000 rpm for 45 minutes. The supernatant was removed and the nanoparticles were re-dispersed in water and re-centrifuged several times to ensure complete removal of any unattached surface units. Complete removal of unbound Gd chelates was confirmed by testing the relaxivity of the supernatant.

Protocol for Relaxometry

The NMRD profiles were measured at ^1H Larmor frequencies from 0.01 to 10 MHz using a Stelar SMARtracer™ FFC NMR relaxometer (0.25 T), equipped with a VTC90 temperature control unit. Each point was measured 8 times and if the deviation was outside 1%, the measurement was repeated and the average value was taken. The measurements were made at 25 °C and 37 °C for each gold nanoparticle (GNP) and the precise concentration of Gd^{3+} was

determined using ICP-OES. The r_1 values were calculated by first subtracting the R_1 of pure water from the R_1 measured and then dividing the resulting value by the concentration of Gd^{3+}.

Protocol for Magnetic Resonance Imaging

Magnetic resonance imaging was performed at 25 °C on a clinical 1.5 T MRI Scanner (Philips Ingenia, Philips Medical Systems) using a Modified Look-Locker Imaging (MOLLI) T_1 sequence. The scan parameters were as follows: 15 x 300 x 300 mm field of view, 300 x 300 mm acquisition matrix, 3 mm slice thickness, 2.145 ms echo time, 4.290 ms repetition time and 50° flip angle. Each nanoparticle sample was prepared at gadolinium concentrations (ICP-OES) between 0.01 and 0.065 mM. The 1 mL phantoms were submerged in water during acquisition to reduce Gibbs artefacts. The T_1 maps were analysed using Philips DICOM Viewer 3.0. T_1 values were extracted for each nanoparticle sample across 5 slices and a mean average value was taken. R_1 was then plotted against gadolinium concentration and the gradient of the straight line was taken to be the relaxivity.

Protocol for in vitro Viability Assay

Cells were seeded into a 96-well plate at a density of 15,000 cells per well and incubated for 24 h at 37 °C in a 5% CO_2 incubator. The cells were then incubated with fresh media containing various concentrations of nanoparticle (0-250 µM) and incubated for a further 24 hours. The media was then replaced with a solution of 3-(4,5-dimethylthiazol-2-yl)-2,5-diphenyltetrazolium bromide (MTT) in PBS (2 mg mL^{-1}) and incubated for 2 hours. The solution was then replaced with DMSO to dissolve the formazan crystals and the absorbance at 570nm was measured using a 96-well plate reader (SpectraMax M2/M2e Microplate Reader from Molecular Devices). All experiments were repeated five times and the cell viability was reported as a percentage relative to the control cells. Error bars represent the standard deviation.

Protocol for in vitro Uptake Study

Cells were seeded into a 96-well plate at a density of 15,000 cells per well and incubated for 24 h at 37 °C in a 5% CO_2 incubator. The cells were then incubated with a 200 µM solution of the respective nanoparticle for a period of 1, 6 or 24 hours and in duplicates. The media was then removed and the cells were washed three times with PBS to ensure that all un-internalised nanoparticles had been removed. The cells were then fixed using a 4% formaldehyde solution and digested using *aqua regia* for at least 2 hours at room temperature. The digested solutions

were then diluted with water to reach a 10% concentration of *aqua regia* and the gold concentration was measured using ICP-OES.

Protocol for in vitro Photodynamic Therapy Study

HeLa cells were seeded into 8-well plates at a density of 30,000 cells per well and incubated for 24 h at 37 °C, in 5% CO_2. The cells were then incubated with a 200 μM solution of the respective nanoparticle in media for a further 24 h. The media was then removed and the cells were washed 3 times with PBS before fresh media were added. Each well was then irradiated with a 570 nm laser, at 37 °C on a Zeiss-Axio Observer inverted microscope for a period of 5, 15 or 30 min. To measure cell viability, an MTT viability assay was performed as described above.

Supporting Information

The synthesis and characterisation of the surface units and functionalised nanoparticles are described in the ESI along with details of relaxivity, cytotoxicity, stability, cell uptake and irradiation studies.

Acknowledgements

The authors wish to express their gratitude to the EPSRC for a DTP studentship (to N.G.C). The EPSRC Centre for Doctoral Training in Smart Medical Imaging (King's College London and Imperial College London) is acknowledged for provision of relaxometer facilities and a studentship (to H.L.P.). We wish to thank the Imperial College President's PhD Scholarship program for a studentship (to I.-C.Y). We are grateful for the assistance of E. Ware in obtaining the TEM images, P. Carry for ICP-OES facilities and G. Nordio for assistance with MRI. We thank the Facility for Imaging by Light Microscopy (FILM) for access to microscopy instruments. This facility is supported by funding from the Wellcome Trust (grant 104931/Z/14/Z) and BBSRC (grant BB/L015129/1).

Conflict of interest

The authors declare no conflict of interest.

References

1. Y. Huang, S. He, W. Cao, K. Cai, X. J. Liang, *Nanoscale* **2012**, *4*, 6135-6149
2. J. S. Basuki, L. Esser, H. T. T. Duong, Q. Zhang, P. Wilson, M. R. Whittaker, D. M. Haddleton, C. Boyer, T. P. Davis, *Chem. Sci.* **2014**, *5*, 715-726.
3. L. C. Kennedy, L. R. Bickford, N. A. Lewinski, A. J. Coughlin, Y. Hu, E. S. Day, J. L. West, R. A. Drezek, *Small* **2011**, *7*, 169-183
4. D. Y. Joh, L. Sun, M. Stangl, A. Al Zaki, S. Murty, P. P. Santoiemma, J. J. Davis, B. C. Baumann, M. Alonso-Basanta, D. Bhang, G. D. Kao, A. Tsourkas, J. F. Dorsey, *PLoS One* **2013**, *8*, e62425-e62435.
5. X. Q. Zhang, X. Xu, R. Lam, D. Giljohann, D. Ho, C. A. Mirkin, *ACS Nano* **2011**, *5*, 6962-6970.
6. A. C. Anselmo, S. Mitragotri, *AAPS* J **2015**, *17*, 1041-1054.
7. C. J. Eling, T. W. Price, A. R. L. Marshall, F. Narda Viscomi, P. Robinson, G. Firth, A. M. Adawi, J.-S.G. Bouillard, G. J. Stasiuk, *ChemPlusChem* **2017**, *82*, 674-680.
8. Y. Cheng, J. D. Meyers, A. M. Broome, M. E. Kenney, J. P. Basilion, C. Burda, *J. Am. Chem. Soc.* **2011**, *133*, 2583-2591.
9. S. Jain, D. G. Hirst, J. M. O'Sullivan, *Br. J. Radiol.* **2012**, *85*, 101-113.
10. R. A. Kudgus, R. Bhattacharya, P. Mukherjee, *Anticancer Agents Med. Chem.* **2011**, *11*, 965-973.
11. R. K. Delong, C. M. Reynolds, Y. Malcolm, A. Schaeffer, T. Severs, A. Wanekaya, *Nanotechnol. Sci. Appl.* **2010**, *3*, 53-63.
12. M. E. Gallina, Y. Zhou, C. J. Johnson, D. Harris-Birtill, M. Singh, H. Zhao, D. Ma, T. Cass, D. S. Elson, *Mater. Sci. Eng. C. Mater. Biol. Appl.* **2016**, *59*, 324-332.
13. P. K. Jain, X. Huang, I. H. El-Sayed, M. A. El-Sayed, *Acc. Chem. Res.* **2008**, *41*, 1578-1586.
14. E. C. Dreaden, A. M. Alkilany, X. Huang, C. J. Murphy, M. A. El-Sayed, *Chem. Soc. Rev.* **2012**, *41*, 2740-2779.
15. P. Caravan, *Chem. Soc. Rev.* **2006**, *35*, 512-523.
16. F. J. Nicholls, M. W. Rotz, H. Ghuman, K. W. MacRenaris, T. J. Meade, M. Modo, *Biomaterials* **2016**, *77*, 291-306
17. R. J. Holbrook, N. Rammohan, M. W. Rotz, K. W. MacRenaris, A. T. Preslar, T. J. Meade, *Nano Lett.* **2016**, *16*, 3202-3209

18. N. Rammohan, R. J. Holbrook, M. W. Rotz, K. W. MacRenaris, A. T. Preslar, C. E. Carney, V. Reichova, T. J. Meade, *Bioconjug. Chem.* **2017**, *28*, 153-160
19. C. Zeng, X. Shi, B. Wu, D. Zhang, W. Zhang, *Colloids Surf. B Biointerfaces* **2014**, *123*, 130-135
20. V. S. Marangoni, O. Neumann, L. Henderson, C. C. Kaffes, H. Zhang, R. Zhang, S. Bishnoi, C. Ayala-Orozco, V. Zucolotto, J. A. Bankson, P. Nordlander, N. J. Halas, *Proc. Natl. Acad. Sci. U. S. A.* **2017**, *114*, 6960-6965
21. G. Liang, L. Xiao, *Biomater. Sci.* **2017**, *5*, 2122-2130
22. Y. Zeng, D. Zhang, M. Wu, Y. Liu, X. Zhang, L. Li, Z. Li, X. Han, X. Wei, X. Liu, *ACS Appl. Mater. Interfaces* **2014**, *6*, 14266-14277
23. Q. Chen, H. Wang, H. Liu, S. Wen, C. Peng, M. Shen, G. Zhang, X. Shi, *Anal. Chem.* **2015**, *87*, 3949-3956
24. B. Zhou, Z. Xiong, J. Zhu, M. Shen, G. Tang, C. Peng, X. Shi, *Nanomedicine* **2016**, *11*, 1639-1652
25. K. S. B. Culver, Y. J. Shin, M. W. Rotz, T. J. Meade, M. C. Hersam, T. W. Odom, *J. Phys. Chem. C* **2016**, *120*, 22103-22109
26. L. F. Vistain, M. W. Rotz, R. Rathore, A. T. Preslar, T. J. Meade, *Chem. Commun.* **2016**, *52*, 160-163
27. B. Zhou, Z. Xiong, P. Wang, C. Peng, M. Shen, S. Mignani, J.-P. Majoral, X. Shi, *Drug Deliv.* **2018**, *25*, 178-186
28. V. Mogilireddy, I. Déchamps-Olivier, C. Alric, G. Laurent, S. Laurent, L. Vander Elst, R. Muller, R. Bazzi, S. Roux, O. Tillement, F. Chuburu, *Contrast Media Mol. Imaging* **2015**, *10*, 179-187
29. A. Pitchaimani, T. D. T. Nguyen, L. Maurmann, J. Key, S. H. Bossmann, S. J. Aryal, *Biomed. Nanotechnol.* **2017**, *13*, 417-426.
30. G. J. Stasiuk, S. Tamang, D. Imbert, C. Gateau, P. Reiss, P. Fries, M. Mazzanti, *Dalton Trans*. **2013**, *42*, 8197-8200
31. G. J. Stasiuk, S. Tamang, D. Imbert, C. Poillot, M. Giardiello, C. Tisseyre, E. L. Barbier, P. H. Fries, M. de Waard, P. Reiss, M. Mazzanti, *ACS Nano* **2011**, *5*, 8193-8201.
32. M. F. Ferreira, B. Mousavi, P. M. Ferreira, C. I. Martins, L. Helm, J. A. Martins, C. F. Geraldes, *Dalton Trans.* **2012**, *41*, 5472-5475.
33. S. Sung, H. Holmes, L. Wainwright, A. Toscani, G. J. Stasiuk, A. J. White, J. D. Bell, J. D. E. T. Wilton-Ely, *Inorg. Chem.* **2014**, *53*, 1989-2005.

34. J. D. E. T. Wilton-Ely, *Dalton Trans.* **2008**, 25-29.
35. E. R. Knight, A. R. Cowley, G. Hogarth, J. D. E. T. Wilton-Ely, *Dalton Trans.* **2009**, 607-609.
36. E. R. Knight, N. H. Leung, Y. H. Lin, A. R. Cowley, D. J. Watkin, A. L. Thompson, G. Hogarth, J. D. E. T. Wilton-Ely, *Dalton Trans*. **2009**, 3688-3697.
37. V. L. Hurtubise, J. M. McArdle, S. Naeem, A. Toscani, A. J. White, N. J. Long, J. D. E. T. Wilton-Ely, *Inorg. Chem*. **2014**, *53*, 11740-11748.
38. E. R. Knight, N. H. Leung, A. L. Thompson, G. Hogarth, J. D. E. T. Wilton-Ely, *Inorg. Chem.* **2009**, *48*, 3866-3874.
39. Y. Zhao, W. Perez-Segarra, Q. Shi, A. Wei, *J. Am. Chem. Soc.* **2005**, *127*, 7328-7329.
40. M. S. Vickers, J. Cookson, P. D. Beer, P. T. Bishop, B. Thiebaut, *J. Mater. Chem.* **2006**, *16*, 209-215.
41. S. Naeem, S. A. Serapian, A. Toscani, A. J. White, G. Hogarth, J. D. E. T. Wilton-Ely, *Inorg. Chem*. **2014**, *53*, 2404-2416.
42. P. D. Jadzinsky, G. Calero, C. J. Ackerson, D. A. Bushnell, R. D. Kornberg, *Science* **2007**, *318*, 430-433.
43. M. Friederici, I. Angurell, M. Seco, O. Rossell, J. Llorca, *Dalton Trans.* **2011**, *40*, 7934-7940.
44. N. G. Chabloz, M. N. Wenzel, H. L. Perry, I.-C. Yoon, S. Molisso, G. J. Stasiuk, D. S. Elson, A. E. G. Cass, J. D. E. T. Wilton-Ely, *Chem. Eur. J.* **2019**, *25*, 10895-10906.
45. a) G. J. Stasiuk, N. J. Long, *Chem. Commun*. **2013**, *49*, 2732-2746; b) B. N. Siriwardena-Mahanama, M. J. Allen, *Molecules* **2013**, *18*, 9352-9381.
46. B. Jagadish, G. L. Brickert-Albrecht, G. S. Nichol, E. A. Mash, N. Raghunand, *Tetrahedron Lett.* **2011**, *52*, 2058-2061.
47. N. Sim, R. Pal, D. Parker, J. Engelmann, A. Mishra, S. Gottschalk, *Org Biomol Chem*. **2014**, *12*, 9389-9404.
48. K.-P. Eisenwiener, P. Powell, H. R. Mäcke, *Bioorg. Med. Chem. Lett.* **2000**, *10*, 2133-2135.
49. J. D. E. T. Wilton-Ely, D. Solanki, G. Hogarth, *Eur. J. Inorg. Chem.* **2005**, 4027-4030.
50. J. D. E. T. Wilton-Ely, D. Solanki, E. R. Knight, K. B. Holt, A. L. Thompson, G. Hogarth, *Inorg. Chem*. **2008**, *47*, 9642-9653.

51. M. J. Macgregor, G. Hogarth, A. L. Thompson, J. D. E. T. Wilton-Ely, *Organometallics* **2009**, *28*, 197-208.
52. G. Hogarth, E.-J. C. R. C. R. Rainford-Brent, S. E. Kabir, I. Richards, J. D. E. T. Wilton-Ely, Q. Zhang, *Inorg. Chim. Acta* **2009**, *362*, 2020-2026.
53. A. Toscani, E. K. Heliövaara, J. B. Hena, A. J. P. White, J. D. E. T. Wilton-Ely, *Organometallics* **2015**, *34*, 494-505.
54. J. A. Robson, F. Gonzalez de Rivera, K. A. Jantan, M. N. Wenzel, A. J. White, O. Rossell, J. D. E. T. Wilton-Ely, *Inorg. Chem*. **2016**, *55*, 12982-12996.
55. A. Toscani, K. A. Jantan, J. B. Hena, J. Robson, E. J. Parmenter, V. Fiorini, A. J. P. White, S. Stagni, J. D. E. T. Wilton-Ely, *Dalton Trans.* **2017**, *46*, 5558-5570.
56. a) M. H. Ou, Y. M. Chen, Y. H. Chang, W. K. Lu, G. C. Liu, Y. M. Wang, *Dalton Trans.* **2007**, 2749-2759.
57. S. Laurent, L. Vander Elst, C. Henoumont, R. N. Muller, *Contrast Media Mol. Imaging* **2010**, *5*, 305-308.
58. A. J. Mieszawska, W. J. Mulder, Z. A. Fayad, D. P. Cormode, *Mol. Pharm.* **2013**, *10*, 831-847.
59. Y. Song, X. Xu, K. W. MacRenaris, X. Q. Zhang, C. A. Mirkin, T. J. Meade, *Angew. Chem.* **2009**, *121*, 9307-9311; *Angew. Chem. Int. Ed. Engl.* **2009**, *48*, 9143-9147.
60. M. D. Salazar, M. Ratnam, *Cancer Metastasis Rev.* **2007**, *26*, 141-152.
61. O. Penon, T. Patino, L. Barrios, C. Nogués, D. B. Amabilino, K. Wurst, L. Pérez-Garcia, *ChemistryOpen* **2015**, *4*, 127-136
62. D. K. Chatterjee, L. S. Fong, Y. Zhang, *Adv. Drug Deliv. Rev.* **2008**, *60*, 1627-1637.
63. D. P. Cormode, J. J. Davis, P. D. Beer, *J. Inorg. Organomet. Polym. Mater.* **2007**, *18*, 32-40.
64. P. D. Beer, D. P. Cormode, J. J. Davis, *Chem. Commun.* **2004**, 414-415.
65. F. Geng. K. Song, J. Z. Xing, C. Yuan, S. Yan, Q. Yang, J. Chen, B. Kong, *Nanotechnology* **2011**, *22*, 285101-285109.
66. M. Marradi, D. Alcantara, J. M. de la Fuente, M. L. Garcia-Martin, S. Cerdan, S. Penades, *Chem. Commun.* **2009**, 3922-3924.
67. C. Alric, J. Taleb, G. Le Duc, C. Mandon, C. Billotey, A. Le Meur-Herland, T. Brochard, F. Vocanson, M. Janier, P. Perriat, S. Roux, O. Tillement, *J. Am. Chem. Soc.* **2008**, *130*, 5908-5915.
68. L. Moriggi, C. Cannizzo, E. Dumas, C. R. Mayer, A. Ulianov, L. Helm, *J. Am. Chem. Soc.* **2009**, *131*, 10828-10829.

69. J. M. Wessels, H. G. Nothofer, W. E. Ford, F. von Wrochem, F. Scholz, T. Vossmeyer, A. Schroedter, H. Weller, A. Yasuda, *J. Am. Chem. Soc.* **2004**, *126*, 3349-3356.
70. T B. Huff, M. N Hansen, Y. Zhao, J. X. Cheng, A. Wei, *Langmuir* **2007**, *23*, 1596-1599.
71. M.-H. Park, Y. Ofir, B. Samanta, P. Arumugam, O. R. Miranda, V. M. Rotello, *Adv. Mater.* **2008**, *20*, 4185-4188.
72. M. N. Hansen, L. S. Chang, A. Wei, *Supramol. Chem.* **2008**, *20*, 35-40.
73. J. Sharma, R. Chhabra, H. Yan, Y. Liu, *Chem. Commun.* **2008**, 2140-2142.
74. H. Zhu, D. M. Coleman, C. J. Dehen, I. M. Geisler, D. Zemlyanov, J. Chmielewski, G. J. Simpson, A. Wei, *Langmuir* **2008**, *24*, 8660-8666.
75. C. Subramani, Y. Ofir, D. Patra, B. J. Jordan, I. W. Moran, M.-H. Park, K. R. Carter, V. M. Rotello, *Adv. Funct. Mater.* **2009**, *19*, 2937-2942.
76. M.-H. Park, Y. Ofir, B. Samanta, V. M. Rotello, *Adv. Mater.* **2009**, *21*, 2323-2327.
77. H. Ichikawa, K. Yasui, M. Ozawa, K. Fujita, *Synth. Met.* **2009**, *159*, 973-976.
78. G. Patel, A. Kumar, U. Pal, S. Menon, *Chem. Commun.* **2009**, 1849-1851.
79. Y. Zhao, J. N. Newton, J. Liu, A. Wei, *Langmuir* **2009**, *25*, 13833-13839.
80. H. Wan, L. Chen, J. Chen, H. Zhou, L. Liu, *J. Disper. Sci. Technol.* **2009**, *30*, 194-197.
81. C. Subramani, A. Bajaj, O. R. Miranda, V. M. Rotello, *Adv. Mater.* **2010**, *22*, 5420-5423.
82. X. Duan, M. H. Park, Y. Zhao, E. Berenschot, Z. Wang, D. N. Reinhoudt, V. M. Rotello, J. Huskens, *ACS Nano* **2010**, *4*, 7660-7666.
83. M. H. Park, S. S. Agasti, B. Creran, C. Kim, V. M. Rotello, *Adv. Mater.* **2011**, *23*, 2839-2842.
84. K. Chen, H. D. Robinson, *J. Nanopart. Res.* **2010**, *13*, 751-761.
85. M. H. Park, X. Duan, Y. Ofir, B. Creran, D. Patra, X. Y. Ling, J. Huskens, V. M. Rotello, *ACS Appl. Mater. Interfaces* **2010**, *2*, 795-799.
86. F. von Wrochem, D. Gao, F. Scholz, H. G. Nothofer, G. Nelles, J. M. Wessels, *Nat. Nanotechnol.* **2010**, *5*, 618-624.
87. M. Brust, J. Fink, D. Bethell, D. J. Schiffrin, C. Kiely, *J. Chem. Soc., Chem. Commun.* **1995**, 1655-1656.

88. M. F. Ferreira, J. Goncalves, B. Mousavi, M. I. Prata, S. P. Rodrigues, D. Calle, P. Lopez-Larrubia, S. Cerdan, T. B. Rodrigues, P. M. Ferreira, L. Helm, J. A. Martins, C. F. Geraldes, *Dalton Trans.* **2015**, *44*, 4016-4031.
89. M. Milne, P. Gobbo, N. McVicar, R. Bartha, M. S. Workentin, R. H. E. Hudson, *J. Mater. Chem. B* **2013**, *1*, 5628-5636.
90. P. J. Debouttière, S. Roux, F. Vocanson, C. Billotey, O. Beuf, A. Favre-Réguillon, Y. Lin, S. Pellet-Rostaing, R. Lamartine, P. Perriat, O. Tillement, *Adv. Funct. Mater.* **2006**, *16*, 2330-2339.
91. J. A. Park, P. A. Reddy, H. K. Kim, I. S. Kim, G. C. Kim, Y. Chang, T. J. Kim, *Bioorg. Med. Chem. Lett*. **2008**, *18*, 6135-6137.
92. M. F. Warsi, V. Chechik, *PCCP* **2011**, *13*, 9812-9817.
93. T. Niidome, M. Yamagata, Y. Okamoto, Y. Akiyama, H. Takahashi, T. Kawano, Y. Katayama, Y. Niidome, *J. Control. Release* **2006**, *114*, 343-347.
94. A. Irure, M. Marradi, B. Arnáiz, N. Genicio, D. Padro, S. Penadés, *Biomater. Sci.* **2013**, *1*, 658-668.
95. G. A. Mansoori, K. S. Brandenburg, A. Shakeri-Zadeh, *Cancers* **2010**, *2*, 1911-1928.
96. V. Lebret, L. Raehm, J.-O. Durand, M. Smaïhi, M. H. V. Werts, M. Blanchard-Desce, D. Méthy-Gonnod, C. Dubernet, *J. Sol-Gel Sci. Technol* **2008**, *48*, 32-39
97. Y. Song, W. Shi, W. Chen, X. Li, H. Ma, *J. Mater. Chem.* **2012**, *22*, 12568-12573.
98. P. García Calavia, G. Bruce, L. Pérez-García, D. A. Russell, *Photochem. Photobiol. Sci.*, **2018**, *17*, 1534-1552.

For ToC use:

Combined magnetic resonance imaging and photodynamic therapy using polyfunctionalised nanoparticles bearing robust gadolinium surface units.

Nicolas G. Chabloz, Hannah L. Perry, Il-Chul Yoon, Andrew J. Coulson, Andrew J. P. White, Graeme J. Stasiuk, René M. Botnar and James D. E. T. Wilton-Ely*

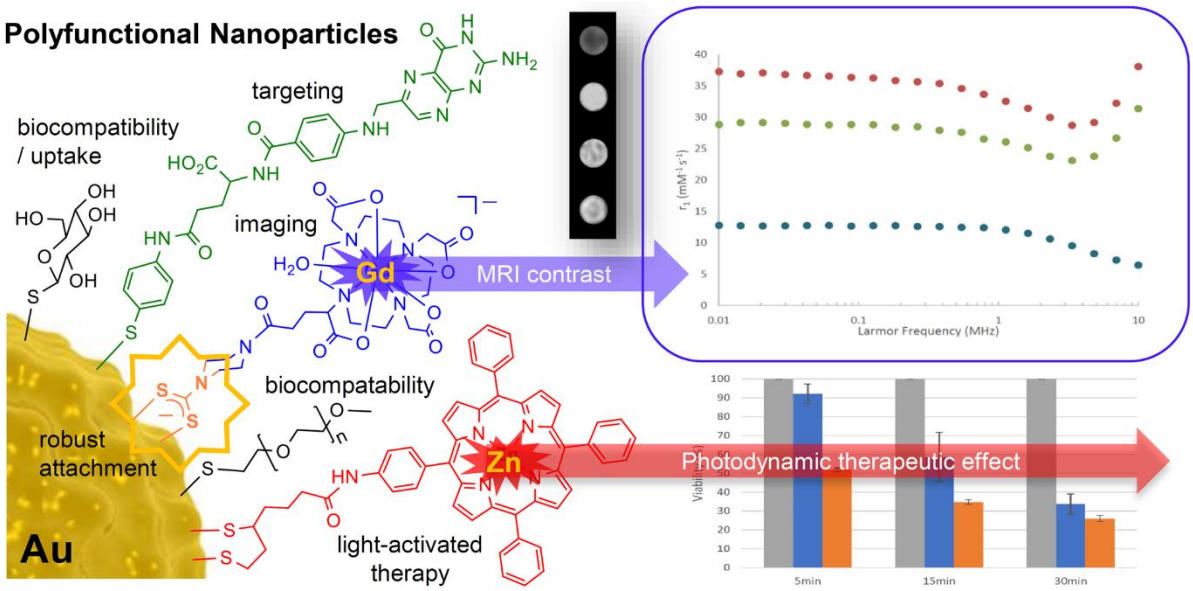

The straightforward synthesis of multifunctional nanoparticles combines the robust attachment of gadolinium units for enhanced MRI contrast with photodynamic therapy.

Keywords: gadolinium, imaging agents, MRI, nanoparticles, PDT

Supporting Information

Combined magnetic resonance imaging and photodynamic therapy using polyfunctionalised nanoparticles bearing robust gadolinium surface units.

Nicolas G. Chabloz, Hannah L. Perry, Il-Chul Yoon, Andrew J. Coulson, Andrew J. P. White, Graeme J. Stasiuk, René M. Botnar and James D. E. T. Wilton-Ely*

S1. General considerations regarding starting materials and equipment

All chemicals and solvents were purchased from Alfa-Aesar, Sigma-Aldrich and VWR and were used without further purification, unless otherwise stated. All experiments and manipulations of compounds were conducted in air, unless otherwise specified. Solvent mixtures are volume/volume mixtures. A Waters LCT Premier ES-ToF (ESI) spectrometer was used for electrospray and high-resolution mass spectra (accurate mass mode). Standard FTIR spectra were measured using a Perkin Elmer Spectrum GX spectrometer. UV-Vis spectra were recorded with a Perkin Elmer Lambda-20 spectrophotometer. Fluorescence measurements in solution were carried out using an Agilent (Varian) Cary Eclipse spectrofluorimeter. NMR spectroscopy was performed at 25 °C using Bruker AV400 or 500MHz spectrometers at room temperature in $CDCl_3$ unless otherwise stated. ^{1}H NMR and ^{13}C NMR chemical shifts (δ) were referenced to the residual non-deuterated solvent signal and the ^{13}C signal of the deuterated solvent, respectively. The deuterated solvents were all purchased from Sigma Aldrich. The widefield microscopy was carried out using a Zeiss Axio Observer inverted microscope in the Facility for Imaging by Light Microscopy (FILM). TEM images and EDS data were obtained at Imperial College using a JEOL 2010 high-resolution TEM (80-200 kV) equipped with an Oxford Instruments INCA EDS 80mm X-Max detector system. Thermogravimetric analysis was performed on a Mettler Toledo DSC 1LF/UMX Thermogravimetric Analyzer, using a ceramic sample holder. The protocol used was to heat between 30-120 °C at 30 °C per minute then hold at 120 °C for 20 minutes before continuing to heat between 120-600 °C at 10 °C per minute. ICP-OES analyses were performed using a Perkin-Elmer OPTIMA 2000 DV ICP-OES spectrometer. Zeta-potential & DLS analyses were carried on a Zetasizer Nano ZS90 DLS system (Malvern Instrument Ltd, England). NMRD profiles were recorded using a SMARtracer 0.25 T bench-top fast field cycling NMR relaxometer (King's College London-Imperial College London CDT in Smart Medical Imaging).

S2. Synthesis and characterization of the surface unit

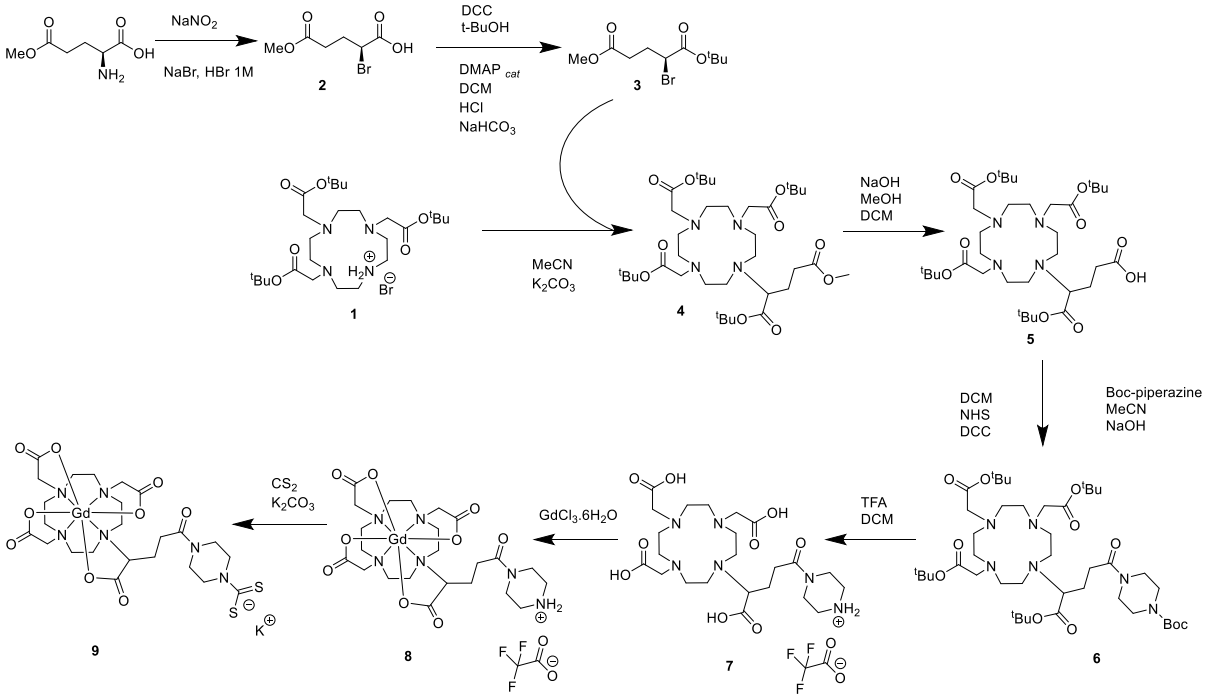

Synthesis of DO3A-tri-^{t}Bu-ester·HBr (**1·HBr**)[1]

At -20 °C, a suspension of cyclen (5.00 g, 29.02 mmol, 1.0 eq.) and sodium acetate (7.86 g, 95.82 mmol, 3.3 eq.) in *N*,*N*-dimethylacetamide (DMA, 60 mL) was treated with a solution of *tert*-butyl bromoacetate (14.10 mL, 95.49 mmol, 3.3 eq.) in DMA (20 mL) dropwise over a period of 40 minutes. The temperature was maintained at -20 °C during the addition, then the mixture was stirred at room temperature for 24 hours. The reaction mixture was then poured onto water (300 mL) to afford a colorless solution. Sodium bicarbonate (12.60 g, 149.98 mmol, 5.1 eq.) was added in portions, inducing the precipitation of **1·HBr** as a white solid. The precipitate was then filtered and dissolved in chloroform (250 mL). The solution was washed with water (100 mL), dried over sodium sulfate, filtered and concentrated to around 20-30 mL. Addition of diethyl ether (250 mL) led to precipitation of **1·HBr** as a white solid (Yield: 13.50 g, 78%).

^{1}H NMR (400 MHz, DMSO-d_6) δ 8.95 (broad, 2H, N<u>H</u>·<u>H</u>Br), 3.42 (s, 4H, NC<u>H</u>$_2$COO), 3.35 (s, 2H, NC<u>H</u>$_2$COO), 2.95 (m, 4H, NC<u>H</u>$_2$C<u>H</u>$_2$N), 2.85 (m, 4H, NC<u>H</u>$_2$C<u>H</u>$_2$N), 2.70 (m, 8H, NC<u>H</u>$_2$C<u>H</u>$_2$N), 1.42 (s, 18H, C<u>H</u>$_3$), 1.41 (s, 9H, C<u>H</u>$_3$) ppm.
^{13}C{^{1}H} NMR (101 MHz, DMSO-d_6) δ 170.6, 169.9 (<u>C</u>OO), 80.5, 80.5 (<u>C</u>(CH$_3$)), 56.1, 51.8, 50.6, 49.7, 48.3, 45.6 (NC<u>H</u>$_2$C<u>H</u>$_2$N, NC<u>H</u>$_2$COO), 27.8 (C(C<u>H</u>$_3$)$_3$) ppm.
MS (ES-Positive) for $C_{26}H_{51}N_4O_6$: calculated $[M]^+$ 515.3808, found $[M]^+$ 515.3793.

Synthesis of 2-bromo-5-methoxy-5-oxopentanoic acid (**2**)[2]

L-Glutamic acid 5-methyl ester (2.00 g, 12.41 mmol, 1.0 eq.) and sodium bromide (4.34 g, 42.19 mmol, 3.4 eq.) were dissolved in a 2N aqueous solution (15 mL) of hydrobromic acid (22.08 mmol, 1.8 eq) and cooled to 0 °C. Sodium nitrite (1.52 g, 22.08 mmol, 1.8 eq.) was added in portions. After stirring for 2 hours, conc. sulfuric acid (0.75 ml) was added followed by 15 minutes of stirring at room

temperature. The aqueous phase was extracted with diethyl ether (3 x 50 mL) and the combined organic phases were dried over magnesium sulfate and concentrated to afford a white powder (2.06 g, 73%).

^{1}H NMR (400 MHz, $CDCl_3$) δ 9.86 (s, 1H, COOH), 4.37 (dd, J = 8.5, 5.7 Hz, 1H, BrCHCOOH), 3.67 (s, 3H, OCH_3), 2.58 – 2.50 (m, 2H, CH_2CH_2), 2.44 – 2.19 (m, 2H, CH_2CH_2) ppm.
$^{13}C\{^{1}H\}$ NMR (101 MHz, $CDCl_3$) δ 174.1, 172.9 (COO), 52.1 (OCH_3), 44.3 (BrCH), 31.3, 29.5 (CH_2CH_2) ppm.
MS (ES-Positive) for $C_6H_9BrO_4$: calculated $[M+H]^+$ 224.9762, found $[M+H]^+$ 224.9779.

Synthesis of 1-tert-butyl 5-methyl 2-bromopentanedioate (**3**)[2]

Compound **2** (2.06 g, 9.10 mmol, 1.0 eq.), DCC (2.44 g, 11.83 mmol, 1.3 eq.) and 4-dimethylaminopyridine (DMAP) (0.11 g, 0.91 mmol, 0.1 eq.) were dissolved in anhydrous dichloromethane (10 mL). The solution was cooled to 0 °C and t-butanol (4.00 mL, 36.40 mmol, 4.0 eq.) was added. The solution was then stirred overnight at room temperature. The precipitate was filtered and the filtrate was concentrated under vacuum. The residue was dissolved in dichloromethane and washed with a 0.5N HCl solution followed by a saturated aqueous solution of sodium bicarbonate. The organic layer was dried over magnesium sulfate, filtered and dried under vacuum to yield a yellow oil which was purified by column chromatography on silica gel 60 (40-63 µm) (eluent 1:1 v/v ethyl acetate/hexane, Rf: 0.70) (Yield: 1.44g, 76%).

^{1}H NMR (400 MHz, $CDCl_3$) δ 4.21 (dd, J = 8.5, 5.9 Hz, 1H, BrCHCOOH), 3.66 (s, 3H, OCH_3), 2.48 (m, 2H, CH_2CH_2), 2.36 – 2.15 (m, 2H, CH_2CH_2), 1.45 (s, 9H, $C(CH_3)_3$) ppm.
$^{13}C\{^{1}H\}$ NMR (101 MHz, $CDCl_3$) δ 172.65 (COOMe), 168.37 (COOtBu), 82.69 ($C(CH_3)_3$), 51.89 (OCH_3), 46.76 (BrCH), 31.45, 29.82, (CH_2CH_2), 27.81 ($C(CH_3)_3$) ppm.
MS (CI-Positive) for $C_{10}H_{17}BrO_4$: calculated $[M+NH_4]^+$ 298.0654, found $[M+NH_4]^+$ 298.0647.

Synthesis of DO3A- tert-butylester-4-methylesterpentane (**4**)

The compound **1·HBr** (3.40 g, 5.70 mmol, 1.0 eq.) was dissolved in anhydrous acetonitrile (200 mL). Potassium carbonate (3.15 g, 22.80 mmol, 4.0 eq.) was added to the reaction mixture which was then heated at reflux for 30 minutes. Compound **3** (1.23 g, 5.94 mmol, 1.1 eq.) was then added and the mixture was left to stir at 70 °C for 24 hours. The unreacted potassium carbonate was removed by filtration and the solvent was removed under vacuum affording a yellow oil. The product was purified by column chromatography on silica gel (eluent 96:4 v/v dichloromethane/ methanol, Rf: 0.58) giving a yellow solid after evaporation of the solvent. (Yield: 4.10 g).

^{1}H NMR (400 MHz, $CDCl_3$) δ 3.63 (s, 3H, OCH_3), 3.48 (d, J=10.4 Hz, 1H, NCHCOO), 3.42 – 3.31 (m, 4H, NCH_2CH_2N), 3.26-2.99 (m, 4H, NCH_2CH_2N), 2.88-2.72 (m, 4H, NCH_2CH_2N), 2.63-2.42 (m, 6H, NCH_2COO), 2.38-2.23 (m, 4H, NCH_2CH_2N), 2.19-2.07 (m, 2H, CH_2CH_2COO), 2.03-1.92 (m, 1H, $CHCH_2CH_2$), 1.75-1.63 (m, 1H, $CHCH_2CH_2$), 1.49-1.36 (m, 36H, $C(CH_3)_3$) ppm.
$^{13}C\{^{1}H\}$ NMR (101 MHz, $CDCl_3$) δ 174.8 (CH_2COOCH_3), 173.5, 173.1, 173.0 (CH_2COO), 82.6, 82.0, 81.9 ($C(CH_3)_3$), 60.0 (NCHCOO), 56.0, 55.9, 55.7, 52.8, 52.6, 51.7, 48.7, 48.3, 47.4, 44.5, 32.4 (NCH_2CH_2N, NCH_2COO), 28.0, 27.9, 27.9 ($C(CH_3)_3$), 19.5 ($CHCH_2CH_2$) ppm.
MS (ES-Positive) for $C_{36}H_{66}N_4O_{10}$: calculated $[M + H]^+$ 715.4857, found $[M + H]^+$ 715.4849.
IR (solid state, cm^{-1}) 2985, 2937, 2862 [ν(C-H)], 1725 [ν (C=O)], 1371 [ν (C-H)], 1225 [ν (C=O) ester], 1160, 1108 [ν(C-N)].
Anal. Calcd (%) $C_{36}H_{66}N_4O_{10}\cdot 2CH_2Cl_2\cdot 2H_2O$: C 49.6, H 8.1, N 6.1; Found: C 49.0, H 7.7, N 6.5.

Synthesis of DO3A- 4-tertiobutylesterbutanoic acid (**5**)[3]

Compound **4** (4.10 g, 5.75 mmol, 1.0 eq.) and NaOH (0.47 g, 11.50 mmol, 2.0 eq.) were dissolved in methanol (20 mL) and stirred at 50 °C overnight. The solution was neutralized to pH 7 with a 1M aqueous HCl solution. The solvent was removed under vacuum and the residue was dissolved in dichloromethane, washed with water and brine, dried over sodium sulfate, filtered and all solvent removed under vacuum to afford a yellow oil. (Yield: 3.20 g, 81%).

^{1}H NMR (400 MHz, 223K, $CDCl_3$) δ 3.50 (d, J = 10.0 Hz, 1H, NCHCOO), 3.47–3.28 (m, 4H, NCH_2CH_2N), 2.99–2.74 (m, 8H, NCH_2CH_2N), 2.72–2.47 (m, 6H, NCH_2COO) 2.32–2.20 (m, 4H, NCH_2CH_2N), 2.16–2.07 (m, 2H, CH_2CH_2COOH), 2.05–1.96 (m, 1H, $CHCH_2CH_2$), 1.70–1.60 (m, 1H, $CHCH_2CH_2$), 1.46–1.38 (m, 36H, $C(CH_3)_3$) ppm.
^{13}C{^{1}H} NMR (101 MHz, 223K, $CDCl_3$) δ 175.2 (CH_2COOH), 172.7, 172.6, 172.3, 172.2 (CH_2COO), 82.2, 82.1, 81.9, 81.8 ($C(CH_3)_3$), 59.2 (NCHCOO), 55.4, 55.3, 55.1 52.4, 52.3, 48.1, 48.0, 47.6, 46.7, 43.8, 33.3 (NCH_2CH_2N, NCH_2COO), 27.8, 27.7, 27.6 ($C(CH_3)_3$), 20.3 ($CHCH_2CH_2$) ppm.
MS (ES-Positive) for $C_{35}H_{64}N_4O_{10}$: calculated $[M + H]^+$ 701.4701, found $[M + H]^+$ 701.4686.

Synthesis of DOTA-boc-piperazine-tetra-tBu-ester (**6**)

Compound **5** (1.10 g, 1.57 mmol, 1.0 eq.) and *N*-hydroxysuccinimide (NHS) (0.40 g, 3.45 mmol, 2.2 eq.) were dissolved in anhydrous dichloromethane (25 mL). The mixture was then cooled to 0 °C, after which *N*,*N*-dicyclohexylcarbodiimide (DCC) (0.39 mg, 1.88 mmol, 1.2 eq.) was added. The reaction mixture was left to stir at 0 °C for 3 hours. 1-boc-piperazine (0.31 g, 1.73 mmol, 1.1 eq.) was dissolved in anhydrous dichloromethane (15 mL) and added at 0 °C. The reaction was left to stir for another 2 hours at 0 °C after which it was stirred for 18 hours at room temperature. The precipitate was filtered and the filtrate was then evaporated to dryness. The foamy solid obtained was dissolved in acetonitrile (10 mL) and kept at -20 °C for 2 hours, producing a precipitate. After filtration, the filtrate was evaporated and dissolved in dichloromethane (20 mL) and washed with an aqueous solution of 2 M NaOH (2 x 10 mL). The organic phase was dried over Na_2SO_4, filtered and evaporated to dryness to afford a yellow foam which was purified by purified by column chromatography on silica gel (eluent 90:10 v/v dichloromethane/ methanol, Rf: 0.47) (Yield: 1.20 g, 88%).

IR (solid state, cm^{-1}): 2980, 2938, 2865 (ν_{C-H}), 1724, 1701 (ν_{C-O}), 1646 ($\nu_{C=O}$), 1368 (ν_{C-H}), 1228 ($\nu_{C=O}$), 1157, 1107 (ν_{C-N}).
^{1}H NMR (400 MHz, $CDCl_3$) δ 3.48–3.33 (m, 4H, CH_2CH_2), 3.27–2.53 (m, 29H, NCH_2CH_2N, NCH_2COO), 1.89–1.83 (m, 1H, NCHCOO), 1.48–1.44 (m, 45H, $C(CH_3)_3$) ppm.
^{13}C{^{1}H} NMR (101 MHz, $CDCl_3$) δ 175.2 ,173.0, 172.9, 172.8, 170.7 (CH_2COO), 154.6 (NCOO), 82.4, 82.1, 82.0, 81.9, 80.5 ($C(CH_3)_3$), 59.7 (NCHCOO), 56.0, 55.9, 55.6, 52.7, 52.6, 48.6, 48.2, 47.3, 45.2, 44.4, 41.4, 31.0 (NCH_2CH_2N, NCH_2COO), 28.4, 28.70, 27.9, 27.8 ($C(CH_3)_3$), 19.8 ($CHCH_2CH_2$) ppm.
MS (ES-Positive) for $C_{44}H_{80}N_6O_{11}$: Calculated $[M + H]^+$ 869.5963, found $[M + H]^+$ 869.5942.

Synthesis of DOTAGA-piperazine TFA (**7**)

Compound **6** (1.20 g, 1.38 mmol, 1.0 eq.) was dissolved in a 1:3 v/v ratio mixture of trifluoroacetic acid and dichloromethane stirred at room temperature for 48 hours. All solvent was removed under vacuum and the residue was then dissolved in dichloromethane and the solvent evaporated again. This process was performed 3 times with dichloromethane and 3 times with methanol. The oily residue was dissolved in a minimum of methanol and diethyl ether was added to induce precipitation of the product. After trituration of the solid, the solvent was isolated as a colorless powder (Yield: 0.91 g, 99%).

IR (solid state, cm^{-1}) 3464, 3106 [ν(O-H)], 2930, 2857 [ν(C-H)], 1676 [ν (C=O) ester], 1629 [ν (C=O) amide], 1391 [ν (C-H)], 1200 [ν (C=O) ester], 1177, 1122 [ν (C-N)].
^{1}H NMR (400 MHz, D_2O) δ 4.01-3.93 (m, 1H), 3.90–3.74 (m, 13H) 3.71–3.53 (m, 3H), 3.47–3.22(m, 8H), 3.19–2.95 (m, 3H), 2.87–2.75 (m, 1H), 2.66–2.47 (m, 1H), 2.02–1.84 (m, 2H), 1.51–1.40 (m, 1H) ppm.
$^{13}C\{^{1}H\}$ NMR (101 MHz, D_2O) δ 175.1, 173.6, 173.5, 172.6, 171.2 (CH_2COO), 163.1, 162.8 (NCOO), 117.8, 114.9 (TFA salt), 56.0, 53.5, 51.1, 50.4, 48.4, 45.4, 43.1, 43.0, 42.9, 42.5, 40.3, 38.5, 33.0 (NCHCOO,NCH_2CH_2N, NCH_2COO,$CHCH_2CH_2$) ppm.
MS (ES-Positive) for $C_{23}H_{41}N_6O_9$: calculated $[M]^+$ 545.2935, found $[M]^+$ 545.2941.
Anal. Calcd (%) for $C_{23}H_{41}N_6O_9 \cdot 0.8Et_2O \cdot H_2O$: C 40.1, H 6.1, N 9.3; Found: C 40.4, H 5.6, N 9.7.

Synthesis of [Gd(DOTAGA-piperazine)] (**8**)

Compound **7** (0.81 g, 1.23 mmol, 1 eq.) was dissolved in water (10 mL) and $GdCl_3 \cdot 6H_2O$ (0.55 g, 1.48 mmol, 1.2 eq.) was added. The pH of the solution was adjusted to 5.6 by addition of an aqueous solution of NaOH. The reaction mixture was stirred at room temperature and the pH was monitored and adjusted to 5.5-6.0. Once the pH was stable, the reaction was stirred overnight at 50 °C. The mixture was then cooled to room temperature, after which the pH was adjusted to 10.9 and stirred for 40 minutes in order to precipitate $Gd(OH)_3$. The reaction mixture was then centrifuged, the supernatant was collected and its pH adjusted to 6.5. The xylenol orange test was performed in order to detect any uncomplexed gadolinium. If the test detected the presence of uncomplexed gadolinium, the workup procedure was repeated until no free gadolinium could be detected (Yield: 0.98 g, 98%).

IR (solid state, cm^{-1}) 3451, 3155 [ν(O-H)], 2934, 2864 [ν(C-H)], 1676 [ν (C=O) ester], 1614 [ν (C=O) amide], 1404 [ν (C-H)], 1205 [ν (C=O) ester], 1130, 1090 [ν (C-N)].
MS (ES-Positive) for $C_{23}H_{38}N_6O_9Gd$: calculated $[M + H]^+$ 700.1941, found $[M + H]^+$ 700.1939.

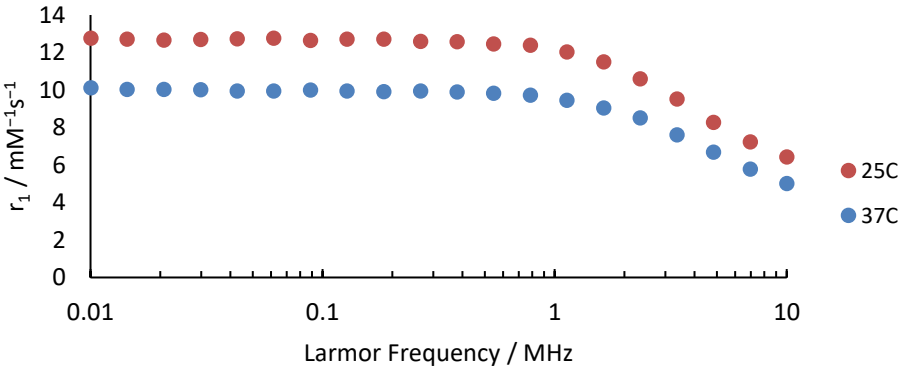

*Figure S2-1 NMRD relaxivity profiles of compound **8** at 25 and 37 °C.*

As a control to confirm the reaction of carbon disulfide to form the dithiocarbamate needed for attachment to the gold surface, attempts were made to prepare AuNPs with just **8**. In contrast to the color change to orange observed with dithiocarbamate **9**, addition of **8** (ammonium salt) to $HAuCl_4$ led to no color change indicating that no reaction had taken place. Continuing with the protocol to form the nanoparticles, addition of the reducing agent $NaBH_4$ led instead to immediate aggregation and precipitation of an insoluble solid (in water, MeOH). This behavior occurs on formation of colloidal gold without the presence of an effective capping ligand.

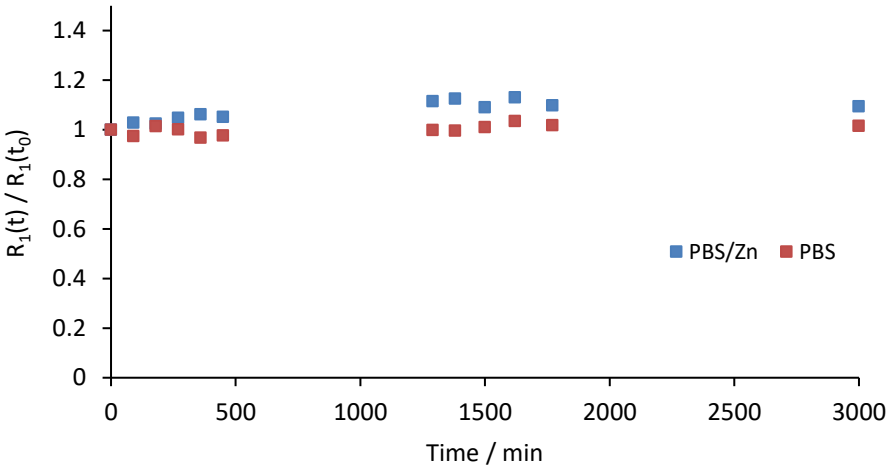

*Figure S2-2 Relaxivity measurements for compound **8** in PBS on addition of 10 eq. $Zn(OAc)_2$ at 37 °C indicating stability to transmetallation and loss of gadolinium(III) ions.*

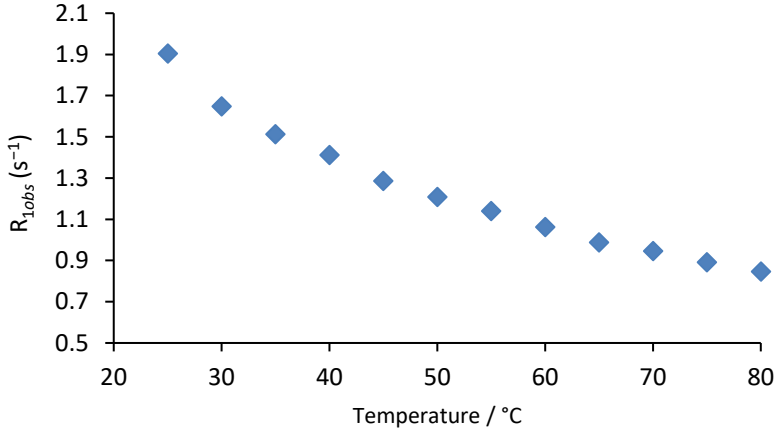

*Figure S2-3 Relaxation rate temperature dependance of **8** indicating a decrease in relaxivity with increasing temperature.*

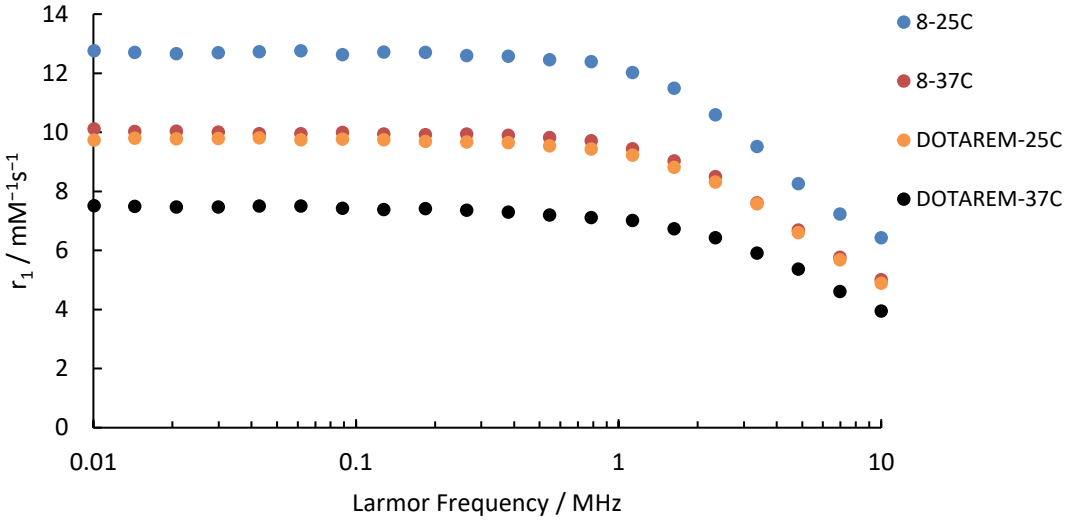

*Figure S2-4 NMRD profiles to compare the relaxivity of **8** and Dotarem at 25°C and 37 °C.*

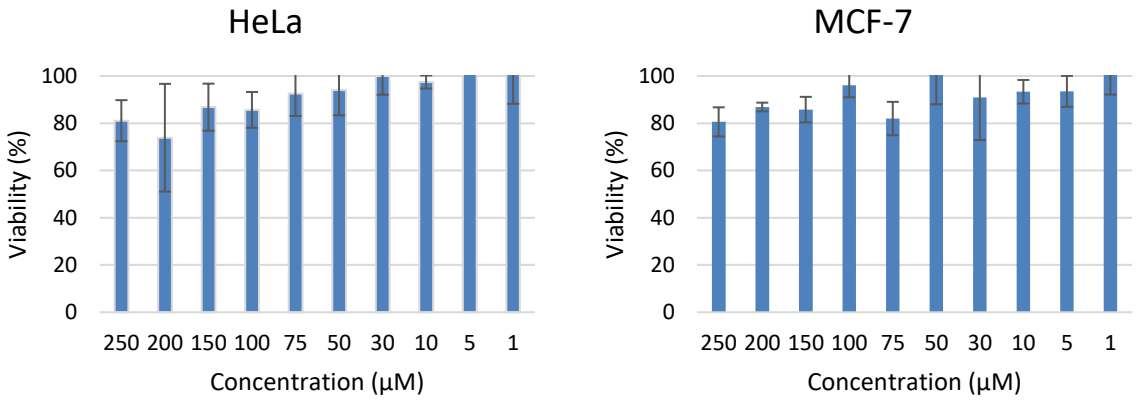

*Figure S2-5 MTT cell viability assays for compound **8**.*

Synthesis of Gd(DOTAGA-piperazine-dithiocarbamate) dipotassium salt (**9**)

A solution of **8** (50 mg, 0.076 mmol, 1 eq.) in 5 mL of dry methanol was treated with potassium carbonate (84 mg, 0.608 mmol, 8 eq.) under nitrogen. The mixture was stirred for 1 hour at room temperature. Carbon disulfide (4.6 µL, 0.076 mmol, 1.2 eq.) was then added at room temperature and the mixture was stirred for another hour. The mixture was filtered through Celite and the filtrate directly used for the functionalization of gold nanoparticles, assuming a quantitative yield.

IR (solid state, cm^{-1}) 3397 [ν(O-H)], 2979 [ν(C-H)], 1676 [ν(C=O) ester], 1601 [ν(C=O) amide], 1427 [ν(C-N)], 1203 [ν(C=O) ester], 1129 [ν(C-N)], 1002 [ν(C-S)].
MS (ES-Positive) for $C_{24}H_{35}N_6O_9S_2Gd$: calculated $[M + K]^+$ 812.0785, found $[M + K]^+$ 812.1283.

Synthesis of [Eu(DOTAGA-piperazine)] (**10**)

Compound **7** (50 mg, 0.076 mmol, 1 eq.) was dissolved in water (10 mL) and $EuCl_3 \cdot 6H_2O$ (34 mg, 0.091 mmol, 1.2 eq.) was added. The pH of the solution was adjusted to 5.6 by addition of an aqueous solution of NaOH. The reaction mixture was stirred at room temperature and the pH was monitored and adjusted to 5.5-6. Once the pH was stable, the reaction was stirred overnight at 50 °C. The mixture was then cooled to room temperature, after which the pH was adjusted to 10.9 and stirred for 40 minutes in order to precipitate $Eu(OH)_3$. The reaction mixture was then centrifuged, the supernatant was collected and its pH adjusted to 6.5. The mixture was purified by size exclusion column (Sephadex G-10).

$^{13}C\{^1H\}$ NMR (101 MHz, D_2O) δ 209.5 (CS_2), 180.0 (NCHCOO), 168.0 (NCH_2COO), 162.8 (NCO), 50.7 (CS_2NCH_2), 44.9 ($CS_2NCH_2CH_2$), 32.0 (NCHCOO, NCH_2CH_2N, NCH_2COO, $CHCH_2CH_2$) ppm.
MS (ES-Positive) for $C_{23}H_{37}EuN_6O_9$: calculated $[M]^+$ 694.1834, found $[M]^+$ 694.1912.

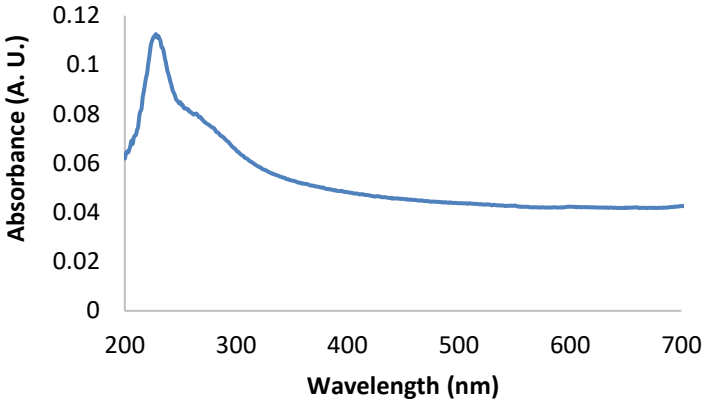

*Figure S2-6 Absorption spectrum of **10**.*

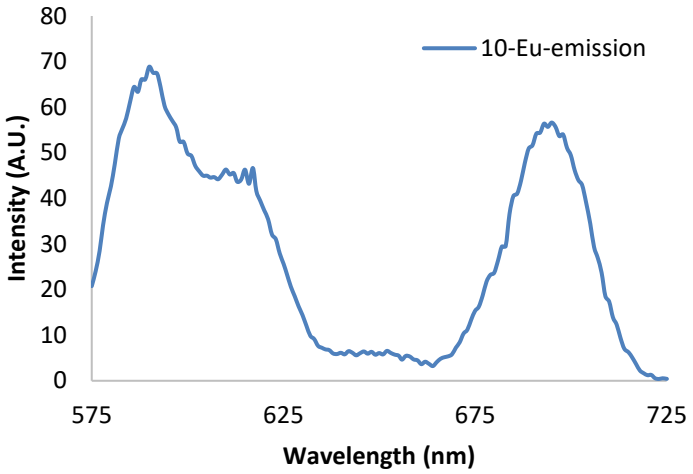

*Figure S2-7 Emission spectrum of **10**.*

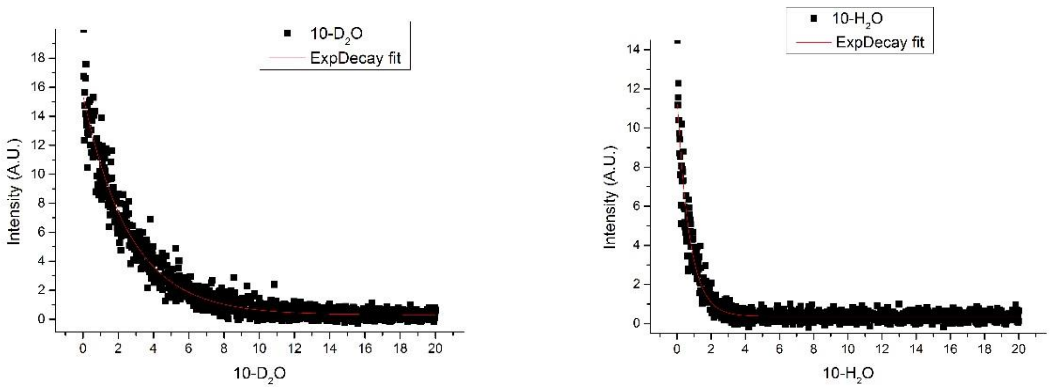

*Figure S2-8 Lifetime measurement of **10** in H_2O and D_2O (pH 7.5, 298K).*

*Table S2-1 Summary of results of the Lifetime measurment of **10** and hydration number*

	$\lambda_{ex}/\lambda_{em}$ (nm)	K_{H2O} (ms^{-1})	τ (ms)	K_{D2O} (ms-1)	τ (ms)	*q*
Compound **10**	230/690	1.37938645	0.72496	0.37829781	2.64342	0.901306

$$q = 1.2((K_{H2O}-K_{D2O})-0.25)$$

S3. Synthesis of the FA-SH ligand

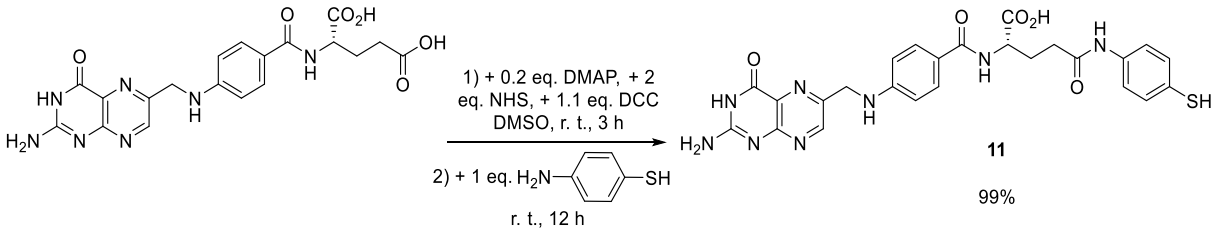

Synthesis of FA-SH (**11**)[4]

A solution of folic acid (200 mg, 0.453 mmol, 1 eq.) in dry dimethylsulfoxide (10 mL) was initially heated under nitrogen at 50 °C to ensure complete dissolution of the starting material. After cooling to room temperature, *N*-hydroxysuccinimide (NHS) (104 mg, 0.906 mmol, 2 eq.), 4-(dimethylamino)pyridine (DMAP) (11 mg, 0.091 mmol, 0.2 eq.) and *N*,*N'*-dicyclohexylcarbodiimide (DCC) (103 mg, 0.498 mmol, 1.1 eq.) were added. The mixture was stirred at room temperature for 3 hours before addition of 4-aminothiophenol (47 µL, 0.453 mmol, 1 eq.). The mixture was stirred overnight under nitrogen. After filtration through Celite, the filtrate was poured onto a cold 1:3 mixture of acetone and diethyl ether. The precipitate was filtered and washed with dichloromethane, acetone and diethyl ether to give **11** as an orange oily solid (Yield: 250 mg, 99%).

NMR data compared well with those reported in the literature.[4]
MS (ES-Positive) for $C_{25}H_{24}N_8O_5S$: calculated $[M + H]^+$ 549.1669, found $[M + H]^+$ 549.1647.
IR (solid state, cm^{-1}): 3253 (ν_{N-H}), 2799 (ν_{C-H}), 1697 ($\nu_{C=O}$), 1014 (ν_{C-N}).

S4. Synthesis of the Porph-SH ligand

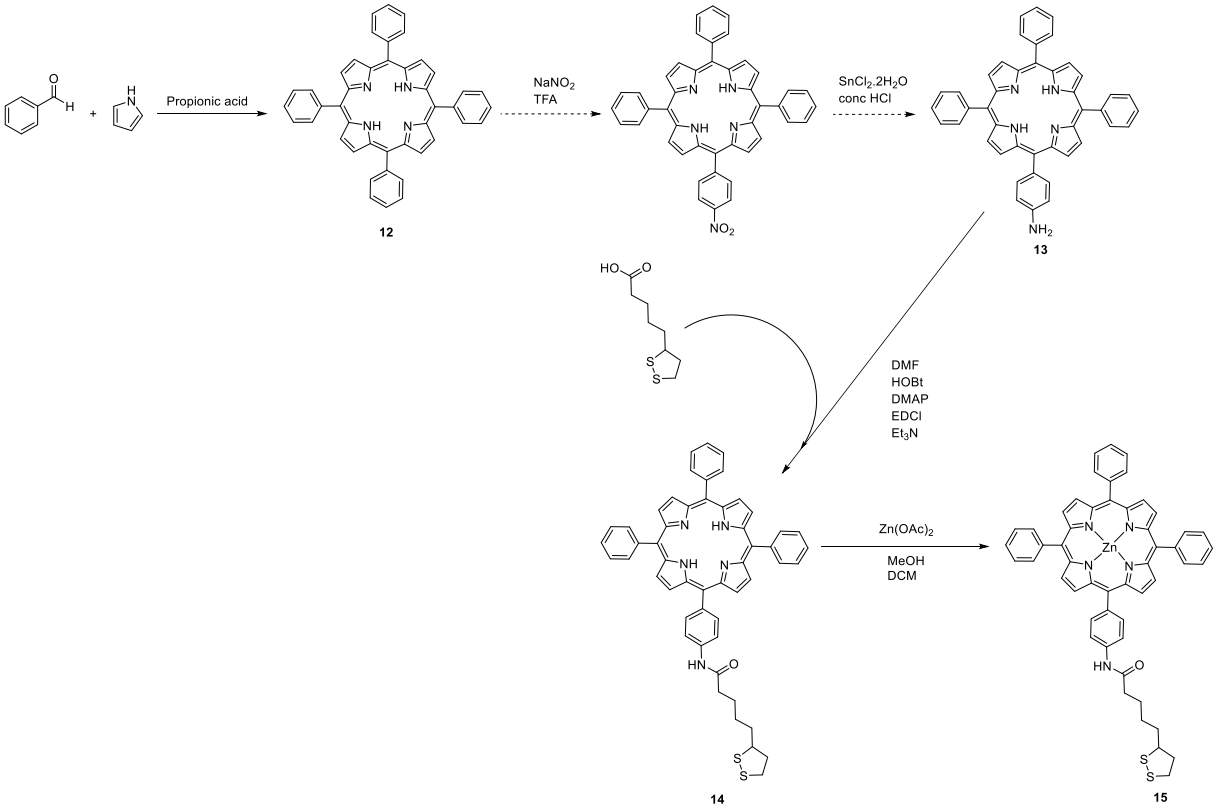

Synthesis of meso-tetraphenylporphyrin (**12**)[5]

Freshly distilled pyrrole (5.60 ml, 80 mmol) and benzaldehyde (8 mL, 80 mmol) were added to propionic acid (300 mL) and heated at reflux for 30 min. The solution was then cooled to room temperature and filtered, the filtered solid was washed thoroughly with methanol. After a hot water wash, the resulting purple crystals were air dried, and finally dried under vacuum to give the purple product (Yield: 2.50 g, 5%).

^{1}H NMR (400 MHz, $CDCl_3$) δ 8.90 (s, 8H, pyrrole), 8.27 (m, 8H, *ortho*-phenyl), 7.80 (m, 12H, *para/meta*-phenyl), -2.72 (s, 2H, NH) ppm.

Synthesis of 5-(4-aminophenyl)-10,15,20-triphenylporphyrin (**13**)[6]

A solution of **12** (500 mg, 0.81 mmol) in trifluoroacetic acid (40 mL) was treated with sodium nitrite (100 mg, 1.45 mmol). After 55 min stirring at room temperature, the reaction was quenched with water (250 mL) and the mixture extracted with dichloromethane. The organic layers were washed once with saturated aqueous $NaHCO_3$ and once with water before being dried over anhydrous Na_2SO_4. The solvent was removed under vacuum and the residue was dissolved in 40 mL of concentrated hydrochloric acid and heated to 65 °C. After 10 min of stirring at 65 °C tin(II) chloride (1.18g, 5.23 mmol) was added. The mixture was stirred for 1 hour at 65 °C, after which it was poured in 250 mL of water and cooled to room temperature. The solution was adjusted to pH 8 using ammonium hydroxide. The solution was then extracted with dichloromethane, dried over Na_2SO_4 and the solvent was removed under vacuum. The product was purified by column chromatography on silica gel (eluent dichloromethane) giving a purple solid after evaporation of the solvent (Yield: 251 mg, 49%).

^{1}H NMR (400 MHz, $CDCl_3$) δ 8.94 (d, J = 4.8 Hz 2H, pyrrole), 8.86 (s, 6H, pyrrole), 8.24 (m, 6H, *ortho*-phenyl), 8.02 (m, 2H, *ortho*-aminophenyl), 7.78 (m, 9H, *para/meta*-phenyl), 7.07 (m, 2H, *meta*-aminophenyl), 4.06 (s, 2H, NH_2), -2.74 (s, 2H) ppm.

Synthesis of Porph-lipoic acid 5-(4-aminophenyl)-10,15,20-triphenylporphyrin (**14**)

Compound **13** (111 mg, 0.17 mmol) and lipoic acid (40 mg, 0.19 mmol) were dissolved in anhydrous DMF followed by addition of HOBt (26 mg, 0.19 mmol), DMAP (2 mg, 0.018 mmol), EDCl (37 mg, 0.19 mmol) and Et_3N (26 µl, 0.19 mmol). The reaction was stirred at room temperature for 48 hours followed by addition of H_2O (15 mL) and EtOAc was then used to extract the product. The organic phase was washed with water and then dried over Na_2SO_4. The product was purified by column chromatography on silica gel (eluent dichloromethane) giving a purple solid after evaporation of the solvent (Yield: 113 mg, 80%).

IR (solid state, cm^{-1}): 3376, 3321, 3054, 3026, 2930, 2857, 2611, 2535, 1698,1669, 1594, 1517, 1474, 1442, 1402, 1350, 1306, 1181, 1128, 1072, 981, 966, 798, 723, 699, 658, 572, 560, 522, 513.
^{1}H NMR (400 MHz, $CDCl_3$) δ 8.86 (s, 8H, pyrrole), 8.25-8.19 (m, 6H, *ortho*-phenyl), 8.18-8.11(m, 2H, *ortho*-aminophenyl), 7.89-7.82 (m, 1H, *meta*-aminophenyl), 7.82-7.70 (m, 10H, *meta*-phenyl, *meta*-aminophenyl), 7.41(s, 1H, NH), 4.25-4.08 (m, 1H, CH), 3.64-3.49 (m, 1H), 3.48-3.32 (m, 1H), 2.70-2.56 (m, 1H), 2.53-2.45 (m, 1H), 2.44-2.37(m, 1H), 2.33-2.07 (m, 1H), 1.95-1.44 (m, 5H), -2.75 (s, 2H) ppm.
^{13}C{^{1}H} NMR (101 MHz, $CDCl_3$) δ 171.0 (CO), 142.2 (Ar_q), 137.6 (Ar_{qNH}), 135.2, 134.7 (Ar), 131.3 (pyrrole), 127.9, 126.8 (Ar), 120.3 (Ar_q), 118.1, 118.0 (Ar_{NH}), 59.7 ($CO\underline{C}H_2$), 55.4 (CH), 37.2, 36.3, 30.8, 27.8, 26.5 (CH_2) ppm.
MS (ES-Positive) for $C_{52}H_{43}N_5OS_2$: Calculated $[M + MeOH + H]^+$ 850.3250, found $[M + MeOH + H]^+$ 850.2937.
Anal. Calcd (%) for $C_{52}H_{43}N_5OS_2$ $1.5CH_2Cl_2$: C 68.0, H 4.9, N 7.4; Found: C 67.8, H 5.0, N 7.6.

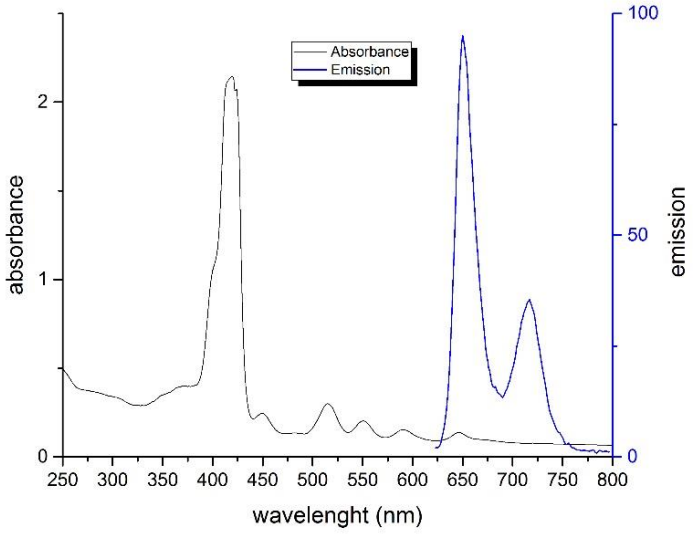

*Figure S4-1 Absorption and emission spectra of **14**.*

Synthesis of Zn-Porph-lipoic acid (**15**)

Compound **14** (20 mg, 0.024 mmol) was dissolved in dichloromethane and ZnOAc (11mg, 0.036 mmol) was dissolved in MeOH, added to the reaction mixture and stirred at room temperature for 8h. The solution was washed with water twice and dried over Na_2SO_4 and the solvent evaporated. The product was purified by column chromatography on silica gel (eluent dichloromethane) giving a purple solid after evaporation of the solvent. The product was recrystallized from a dichloromethane/hexane solution to produce a purple solid (17 mg, 80%).

IR (solid state, cm^{-1}): 3340, 3051, 2921, 2850, 1651, 1595, 1522, 1484, 1439, 1400, 1339, 1302, 1262, 1203, 1179, 1124, 1068, 993, 795, 751, 717, 701, 660, 571, 501, 438.
^{1}H NMR (400 MHz, THF-d_8) δ 9.50 (d, J = 12.3 Hz, 1H, NH), 8.91 (d, J = 4.6 Hz, 2H, pyrrole), 8.84 (d, J = 4.4 Hz, 6H, pyrrole) 8.24-8.15 (m, 6H, ortho-phenyl), 8.13-8.08 (m, 2H, amino-phenyl), 8.08-8.04 (m, 2H, amino-phenyl), 7.79-7.67 (m, 9H, meta, para-phenyl), 4.37-4.25 (m, 1H, CH), 3.69-3.55 (m, 1H), 3.53-3.44 (m, 1H), 2.78-2.63 (m, 1H), 2.52-2.47 (m, 2H), 2.32-2.17 (m, 1H), 2.12-1.49 (m, 6H) ppm.
^{13}C{^{1}H} NMR (101 MHz, DMSO-d_6) δ 171.5 (CO), 151.4, 151.3, 151.0, 150.9, 144.6, 140.3, 138.9, 138.0 (C_q), 135.6 (amino-phenyl), 135.4 (*ortho*-phenyl), 132.3, 132.2 (pyrrole), 128.1, 127.2 (*meta/para*-phenyl), 121.5 (amino-phenyl$_q$), 117.8 (amino-phenyl), 60.3 (CH_2), 56.1 (CH), 37.4, 32.3, 31.5, 28.8, 28.6, 27.5 (6 x CH_2) ppm.
MS (ES-Positive) for $C_{52}H_{41}N_5OS_2Zn$: calculated $[M + H + MeCN + Na]^+$ 944.2285, found $[M + H + MeCN + Na]^+$ 944.2006.
Anal. Calcd (%) for $C_{52}H_{41}N_5OS_2Zn$ CH_2Cl_2 $2C_4H_8O$: C 66.0, H 5.4, N 6.3; Found: C 65.9, H 5.5, N 5.8.

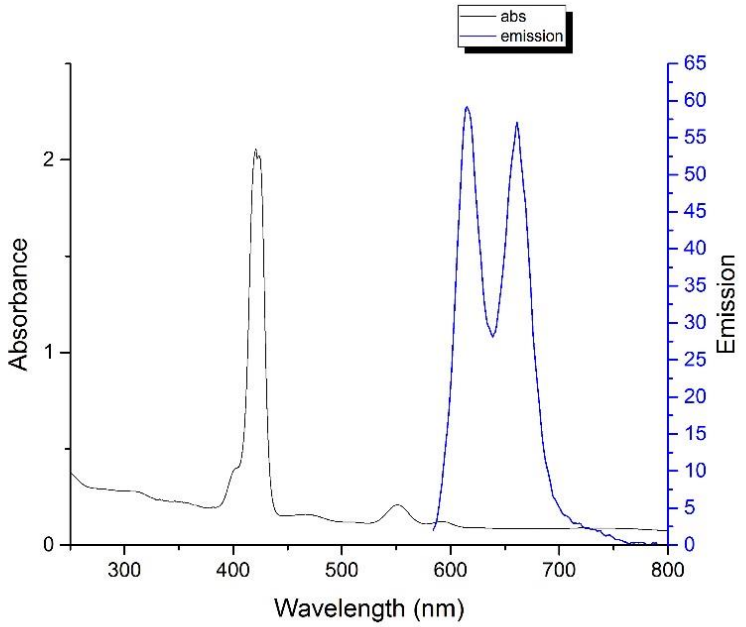

*Figure S4-2 Absorption and Emission spectra of **15**.*

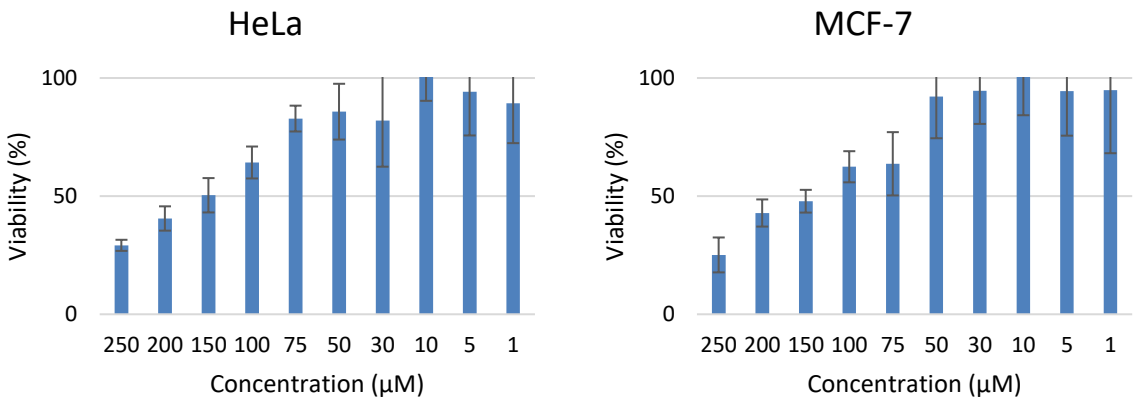

*Figure S4-3 MTT viability assays for **15**.*

S5. Synthesis of the functionalized gold nanoparticles (GNPs)

General protocol for the synthesis of gold nanoparticles (adapted Brust-Schiffrin method):[7]

In a flask pre-washed with *aqua regia* and thoroughly rinsed with ultrapure water was introduced $HAuCl_4$ (59 mg, 0.150 mmol, 1 eq.) in methanol (13 mL). The sulfur-based ligand(s) (PEG-SH, thioglucose, **8**, **15**) were then introduced at the desired quantities (0.01 - 1 eq. relative to Au) in solution (ultrapure water for PEG-SH and thioglucose, in a 1:1 mixture of ultrapure water and DMSO for **8** and in a 1:1 mixture of methanol and acetonitrile for **15**). The mixture was then cooled down to 4°C with an ice bath for at least 10 minutes. A fresh solution of sodium borohydride (47.3 mg, 1.252 mmol, 8.4 eq.) in 3.3 mL of ultrapure water was then added dropwise. The mixture was stirred at 10 °C for 3 hours. The nanoparticles were then centrifuged at 5000 rpm for 45 minutes. The supernatant was removed and the nanoparticles were redispersed in water and centrifuged several times to ensure complete removal of any unattached surface units. Complete removal of **8** was confirmed by testing the relaxivity of the supernatant.

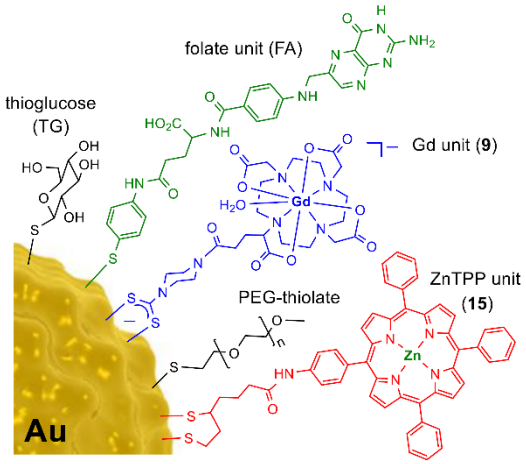

	Au	Gd (**9**)	PEG	TG	FA	ZnTPP (**15**)
NP1	1	1	-	-	-	-
NP2	1	1	0.05	-	-	-
NP3	1	1	0.05	0.05	-	-
NP4	1	1	0.05	-	0.01	-
NP5	1	1	0.05	0.05	0.01	-
NP6	1	1	-	-	-	0.5
NP7	1	1	0.05	-	-	0.5
NP8	1	1	0.05	0.05	-	0.5
NP9	1	1	0.05	-	0.05	0.5
NP10	1	1	0.05	0.05	0.05	0.5

Figure S5-1 Proportions of surface units used to prepare the nanoparticles.

S6. Characterization of the AuNPs

S6.1 Infrared spectroscopy

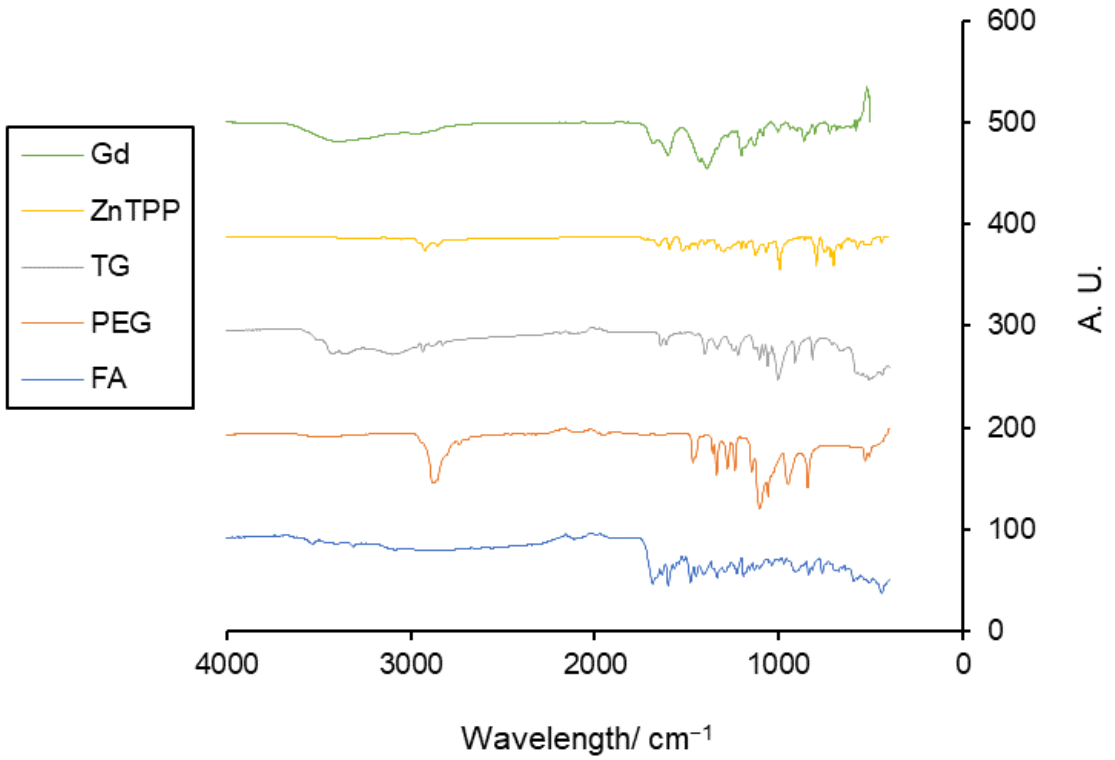

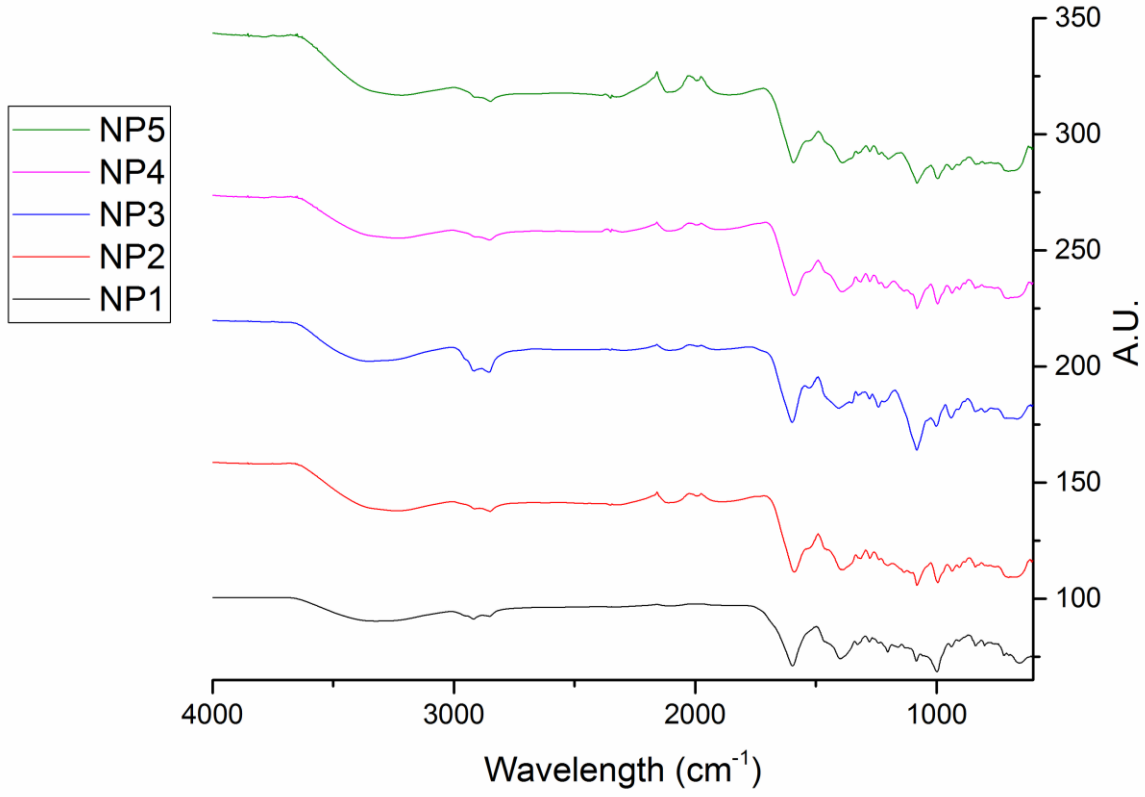

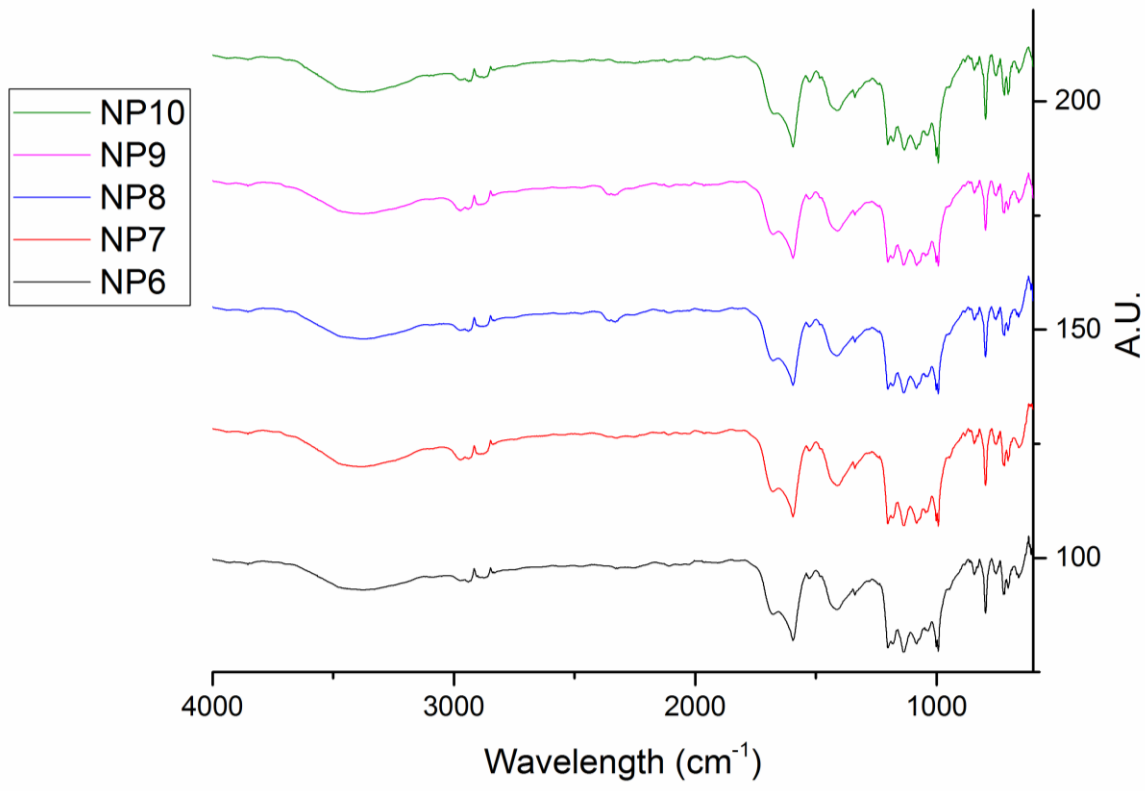

*Figure S6-1 Infrared spectra of the surface units and **NP1** - **NP10**.*

S6.2 Characterization of NP1[Gd]

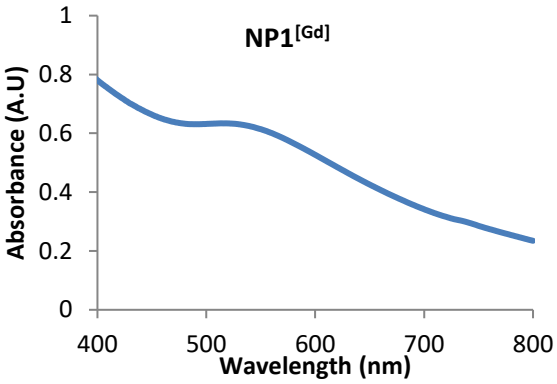

*Figure S6.2-1 UV-vis spectrum of **NP1***

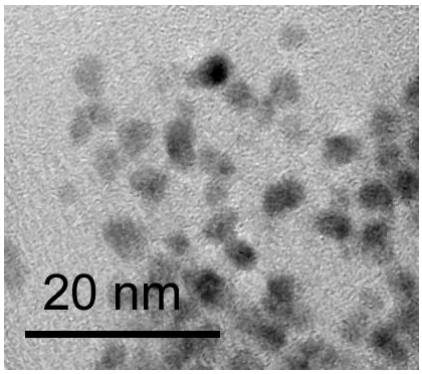

*Figure S6.2-2 TEM image of **NP1.***

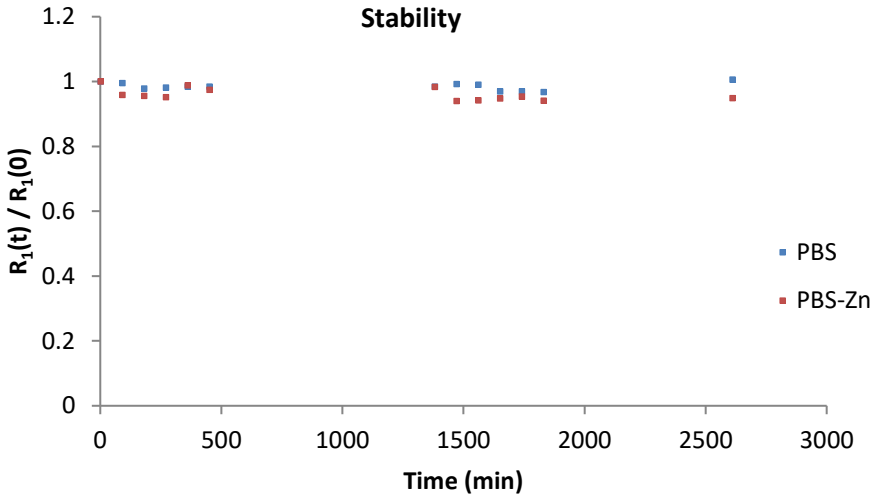

*Figure S6.2-3 Relaxivity data for **NP1** between t = 0 and t = 2610 minutes on addition of Zn^{2+} (2 eq. per Gd) in a transmetallation experiment at 37 °C.*

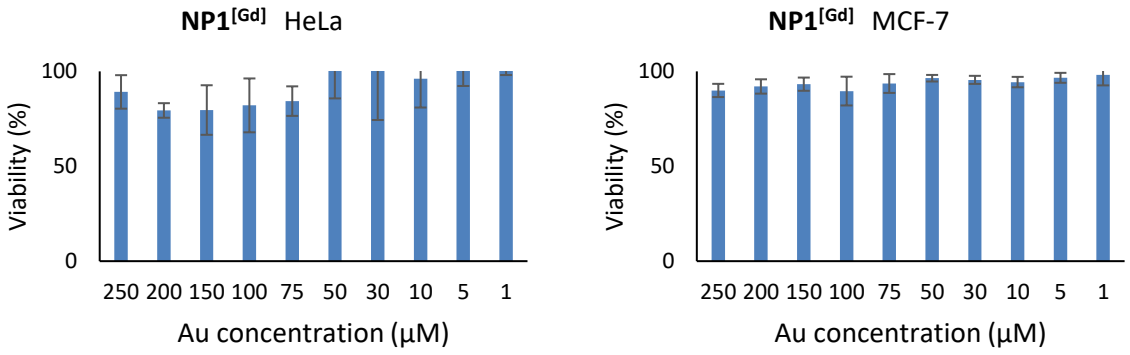

*Figure S6.2-4 Cell viability of HeLa and MCF-7 cells incubated with different concentration of **NP1** after 24h.*

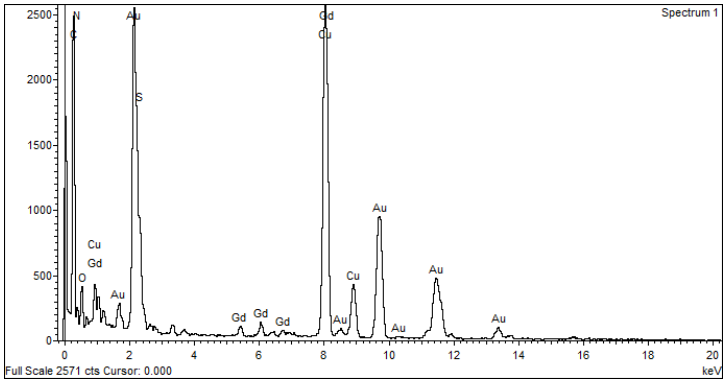

*Figure S6.2-5 EDX data for **NP1**.*

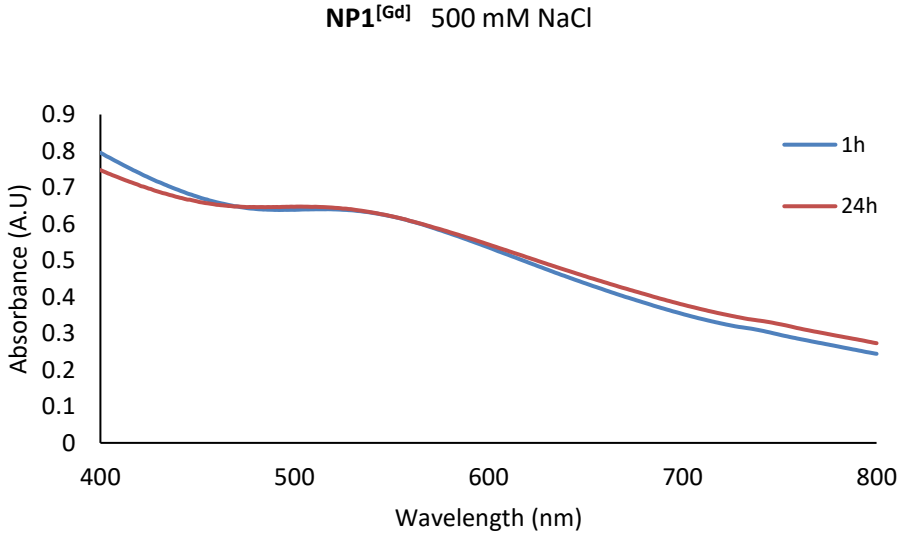

*Figure S6.2-6 UV-vis spectra of **NP1** at various salt concentrations over time.*

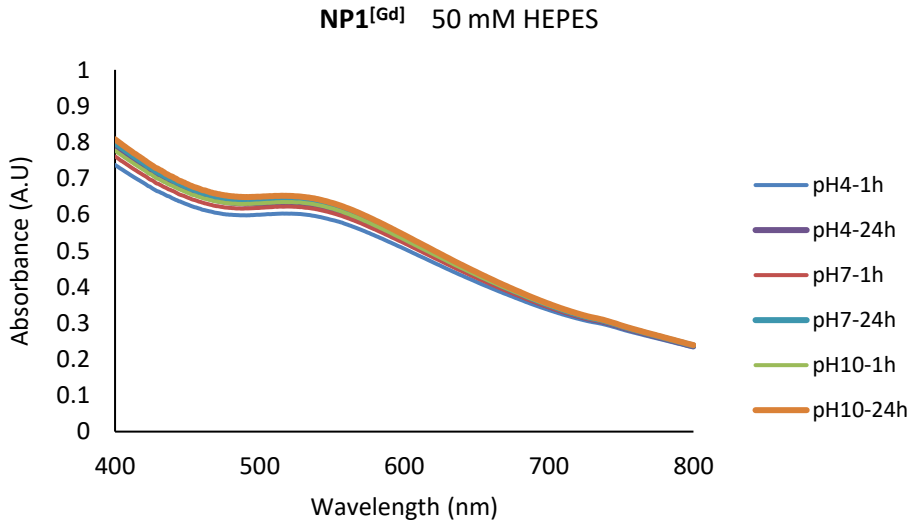

*Figure S6.2-7 UV-vis spectra of **NP1** at various pH values over time.*

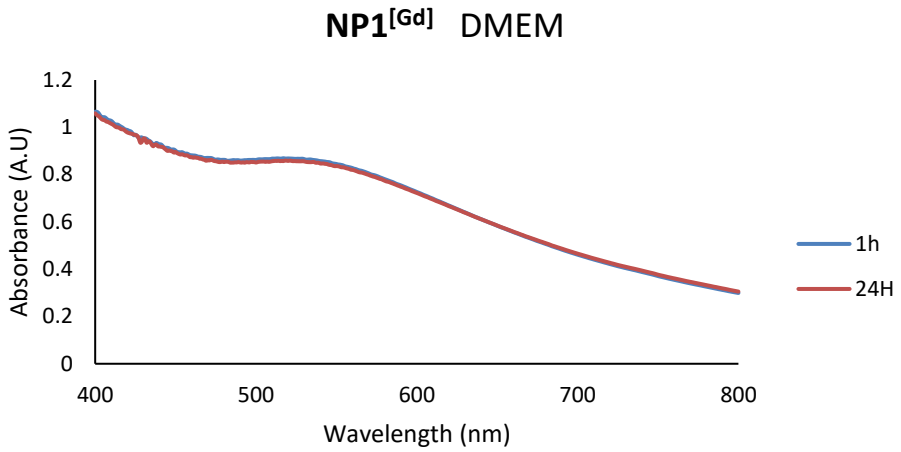

*Figure S6.2-8 UV-vis spectra of **NP1** in DMEM at various time points.*

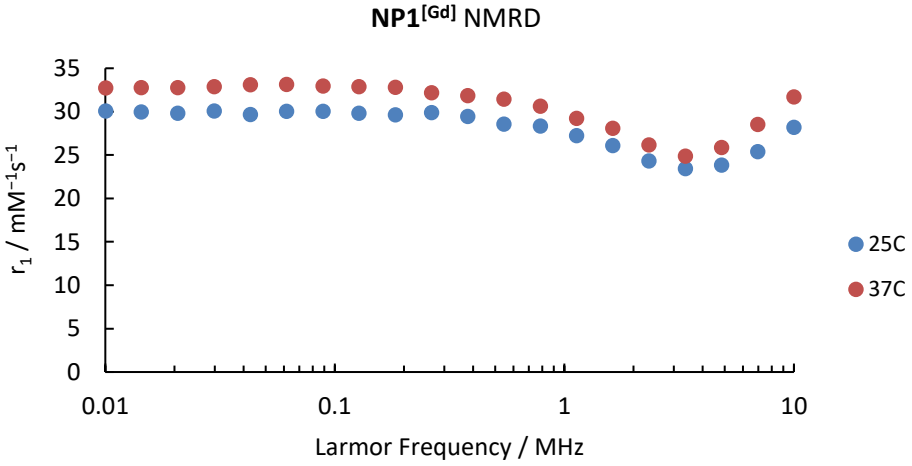

*Figure S6.2-9 NMRD profiles of **NP1** at 25 and 37 °C.*

*Table S6.2-1 Zeta-potential and DLS data for **NP1**.*

Zeta Potential / mV	− 36.5
TEM diameter / nm	4.08 ± 0.67
Hydrodynamic diameter / nm	11.59 ± 4.42

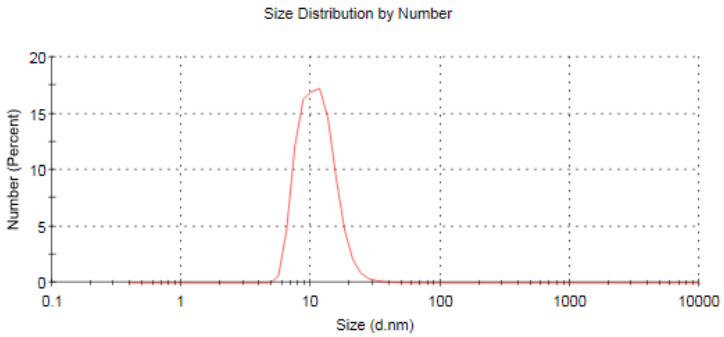

*Figure S6.2-10 DLS data for **NP1**.*

The composition of **NP1** was calculated to be $\mathbf{Au_{3301}(C_{24}H_{35}GdN_6O_9S_2)_{206}}$ based on a combination of TEM data (diameter) to provide the number of Au atoms (assuming NP is a sphere) and TGA data to provide information on mass loss for the organic chelate. The number of gold atoms (N) is calculated from $N = (R_{cluster}/R_{atom})^3 = (2.04 \times 10^{-9}/1.37 \times 10^{-10})^3$. Number of Gd taken from the % mass loss from TGA data (16% mass loss due to the organic part of the ligand) with the remaining 84% made up of approximately 80.3% Au and 3.7% Gd.

*Table S6.2-2 Ratios of Au to Gd determined by ICP and TGA and overall relaxivity of **NP1**.*

Estimate of number of Gd per Au atoms	**Ratio (Au/Gd) from TEM/ICP**	**Ratio (Au/Gd) from TEM/TGA**	**NP r_1 (10 MHz) at 37 °C**
NP1[Gd]	Au_{3301}/Gd_{179} 18/1	Au_{3301}/Gd_{206} 16/1	5691

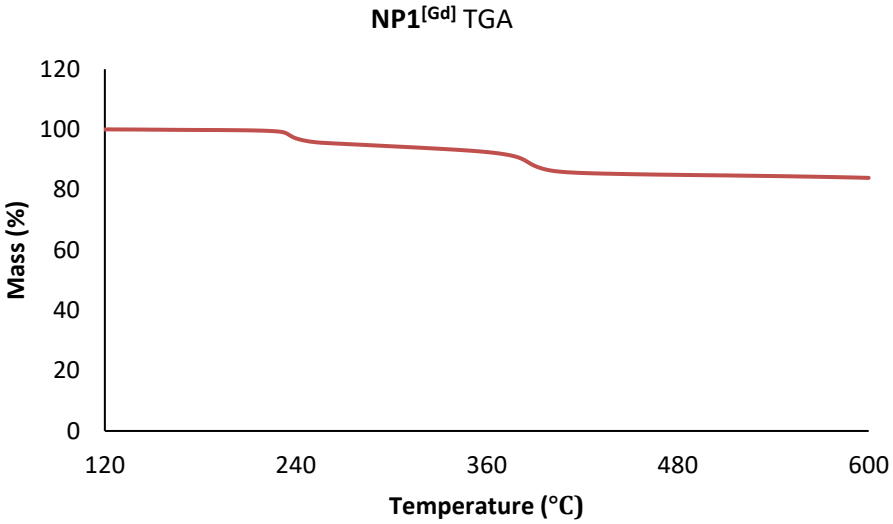

*Figure S6.2-11 TGA data for **NP1**.*

S6.3 Characterization of NP2[Gd]/PEG (1/0.05)

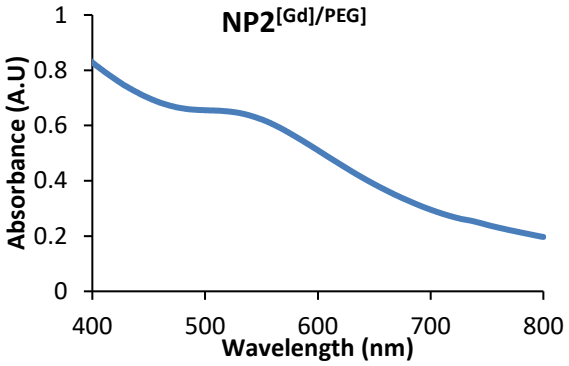

*Figure S6.3-1 UV-vis spectrum of **NP2**.*

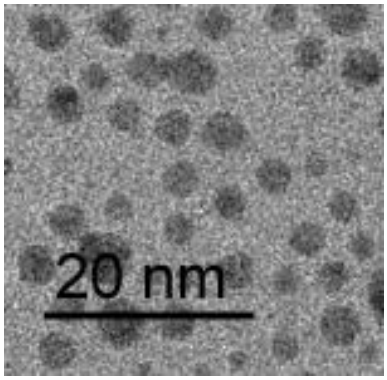

*Figure S6.3-2 TEM image of **NP2**.*

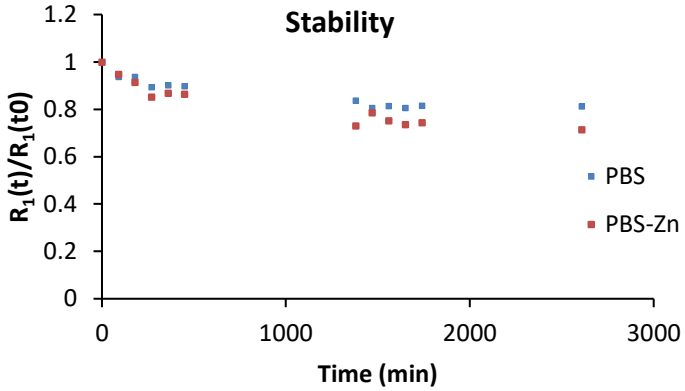

*Figure S6.3-3 Relaxivity data for **NP2** between t = 0 and t = 2610 minutes on addition of Zn^{2+} (2 eq per Gd) in a transmetallation experiment at 37 °C.*

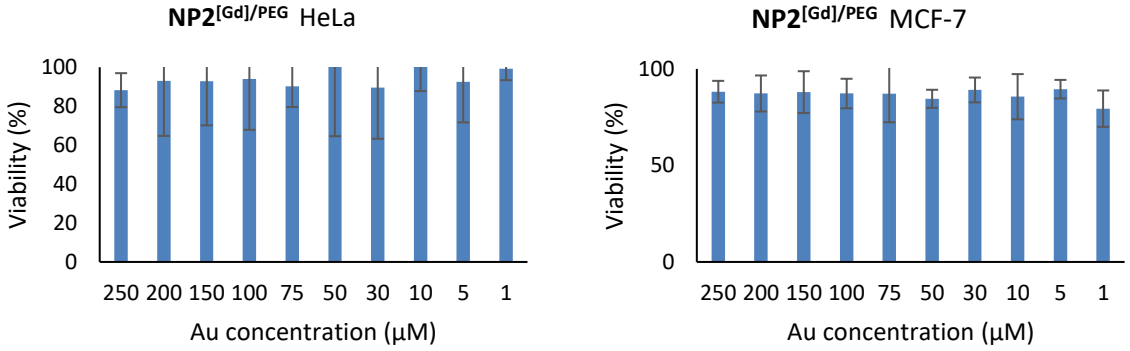

*Figure S6.3-4 Cell viability of HeLa and MCF-7 cells incubated with different concentrations of **NP2** after 24h.*

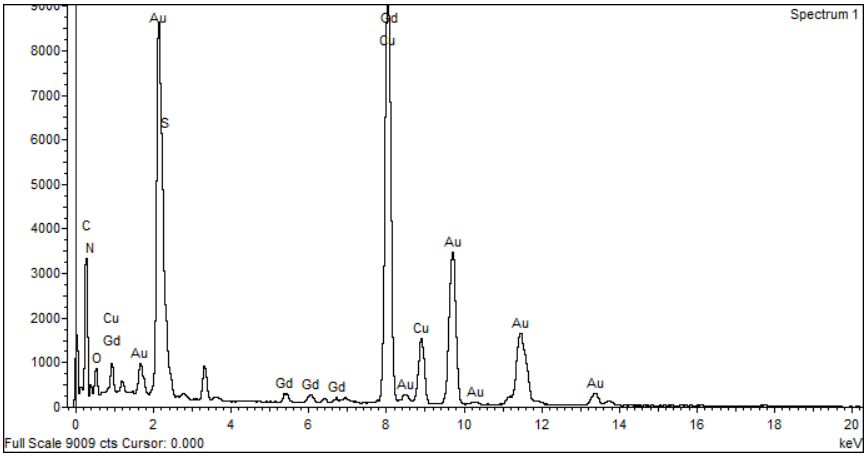

*Figure S6.3-5 EDX data for **NP2**.*

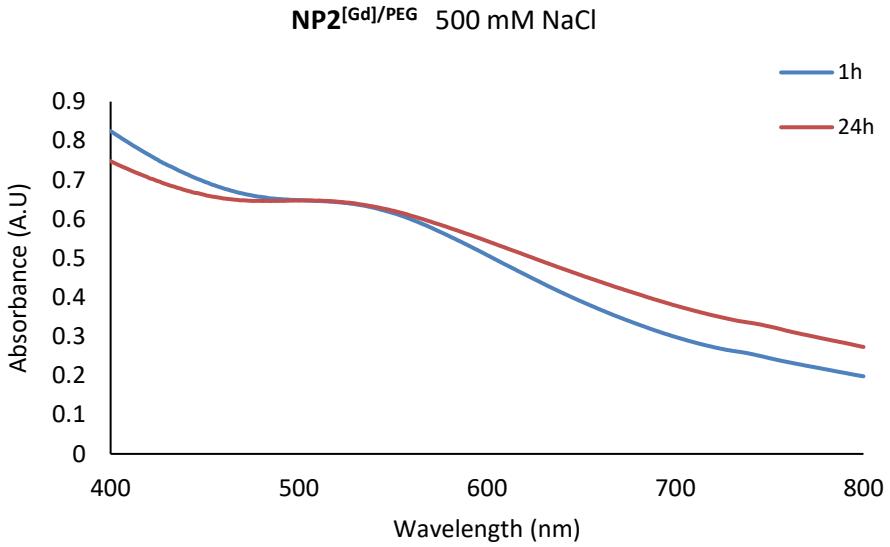

*Figure S6.3-6 UV-vis spectra of **NP2** at various salt concentrations over time.*

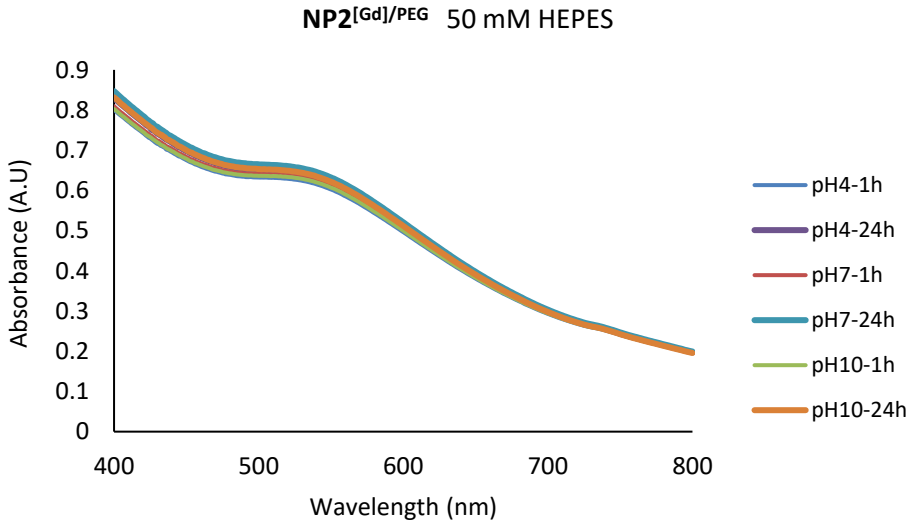

*Figure S6.3-7 UV-vis spectra of **NP2** at various pH values over time.*

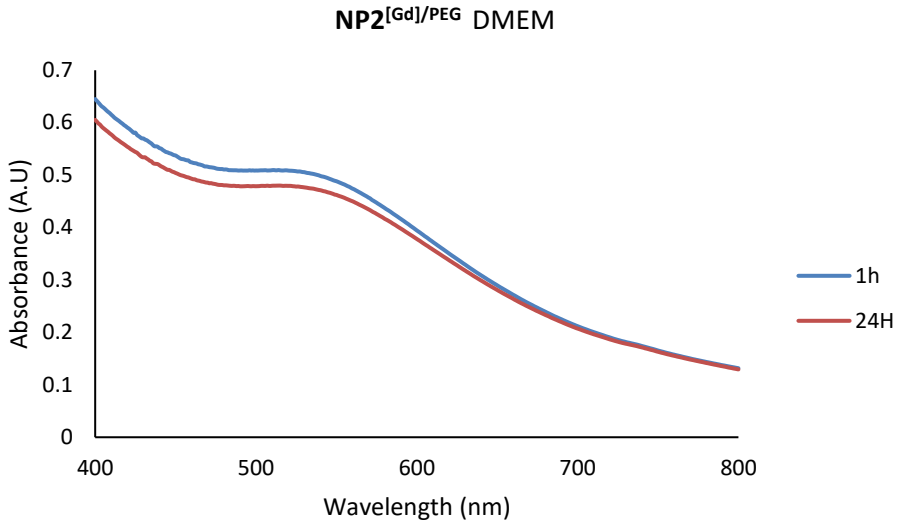

*Figure S6.3-8 UV-vis spectra of **NP2** in DMEM over time.*

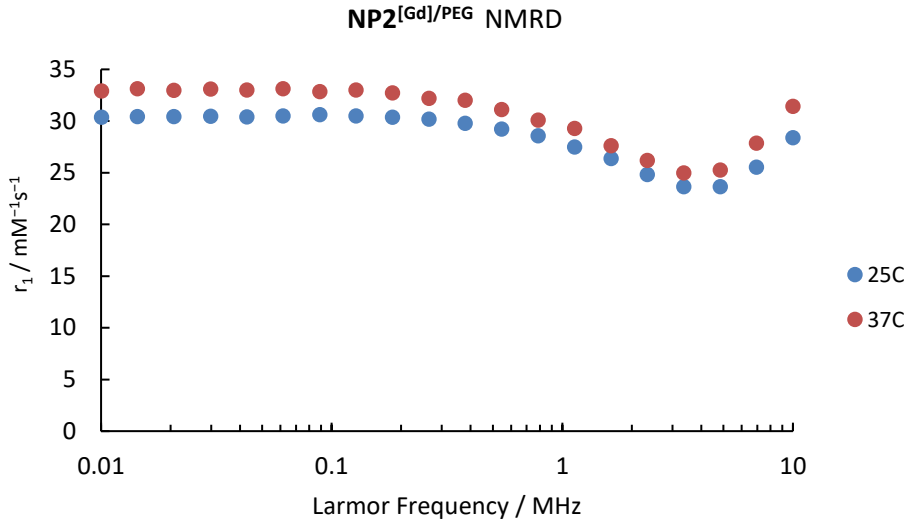

*Figure S6.3-9 NMRD profiles of **NP2** at 25 and 37 °C.*

*Table S6.3-1 Zeta potential and size of **NP2**.*

Zeta Potential / mV	− 39.8
TEM diameter / nm	3.96 ± 0.74

*Table S6.3-2 Ratios of Au to Gd determined by ICP and overall relaxivity for **NP2***

Estimated number of Gd per Au atoms	**Ratio (Au/Gd)**	**NP r_1 (10 MHz) at 37 °C**
NP2[Gd]/PEG	Au_{3018}/Gd_{118} (26:1)	3719

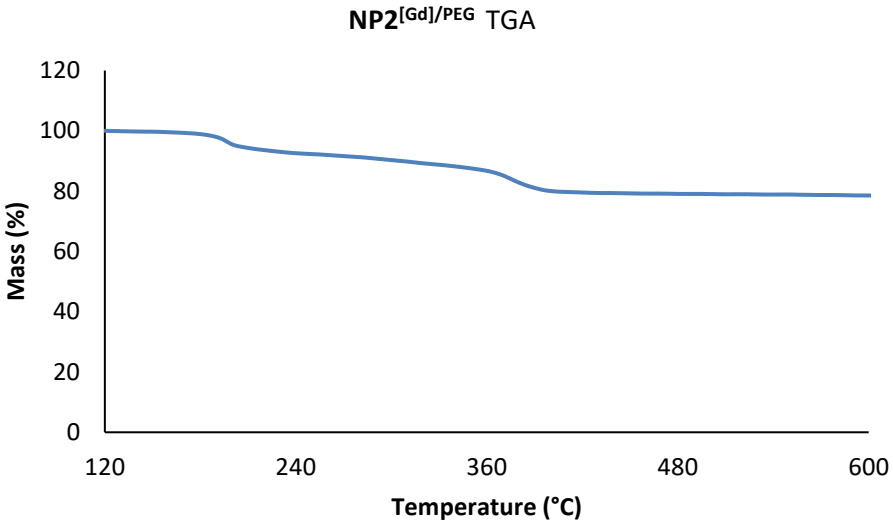

*Figure 9 TGA data for **NP2**.*

S6.4 Characterization of NP3[Gd]/PEG/TG (1:0.05:0.05)

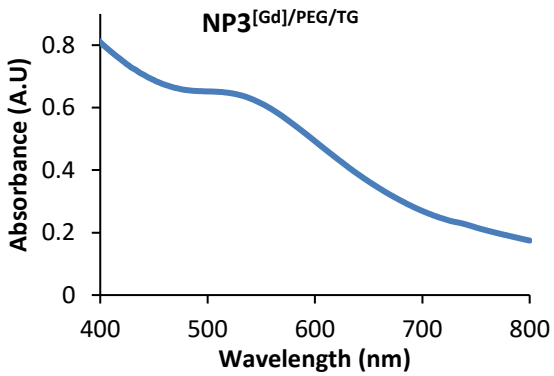

*Figure S6.4-1 UV-vis spectrum of **NP3**.*

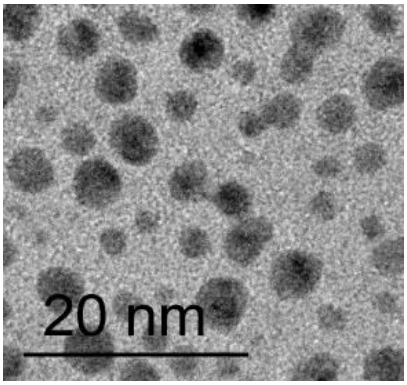

*Figure S6.4-2 TEM image of **NP3**.*

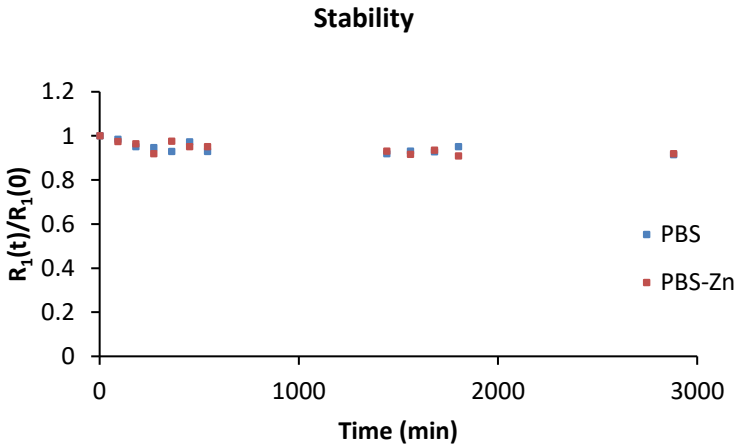

*Figure S6.4-3 Relaxivity for **NP3** between t = 0 and t = 2610 minutes on addition of Zn^{2+} (2 eq. per Gd) in a transmetallation experiment at 37 °C.*

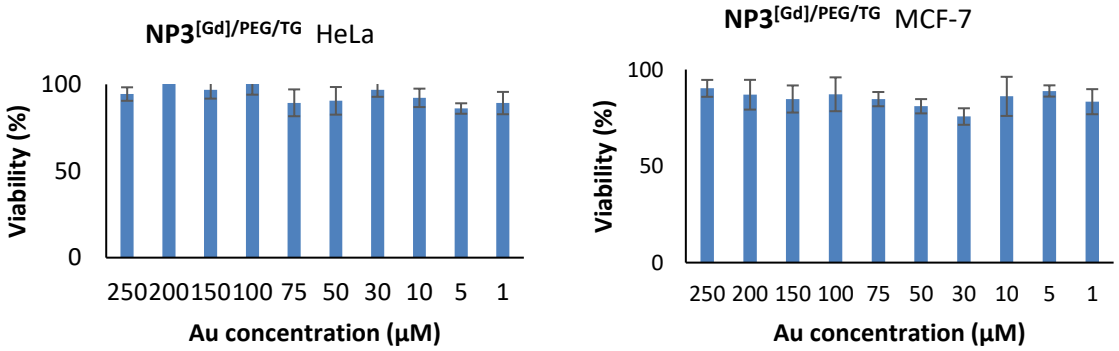

*Figure S6.4-4 Cell viability of HeLa and MCF-7 cells incubated with different concentrations of **NP3** after 24h.*

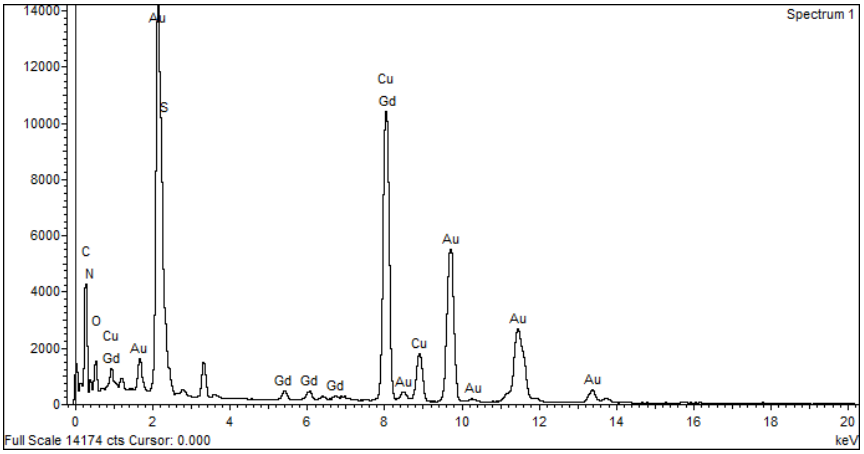

*Figure S6.4-5 EDX data for **NP3**.*

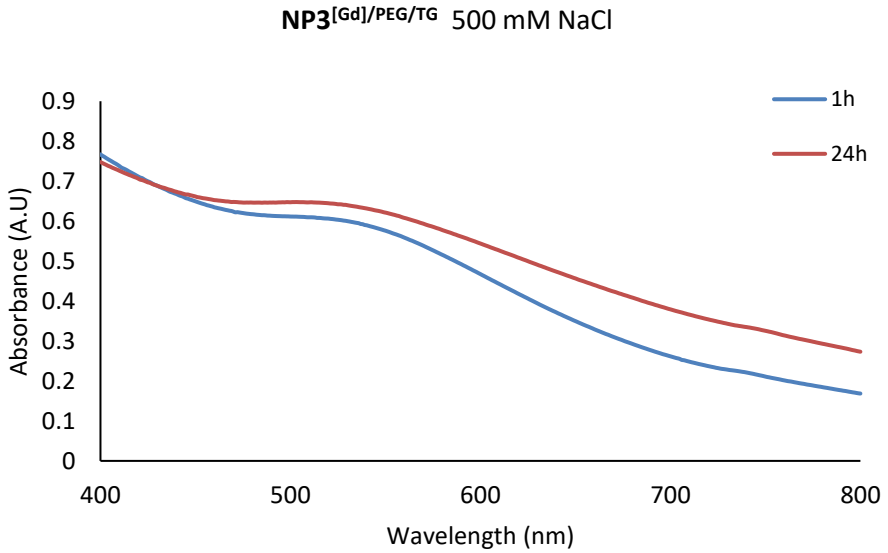

*Figure S6.4-6 UV-vis spectra of **NP3** at various salt concentrations over time.*

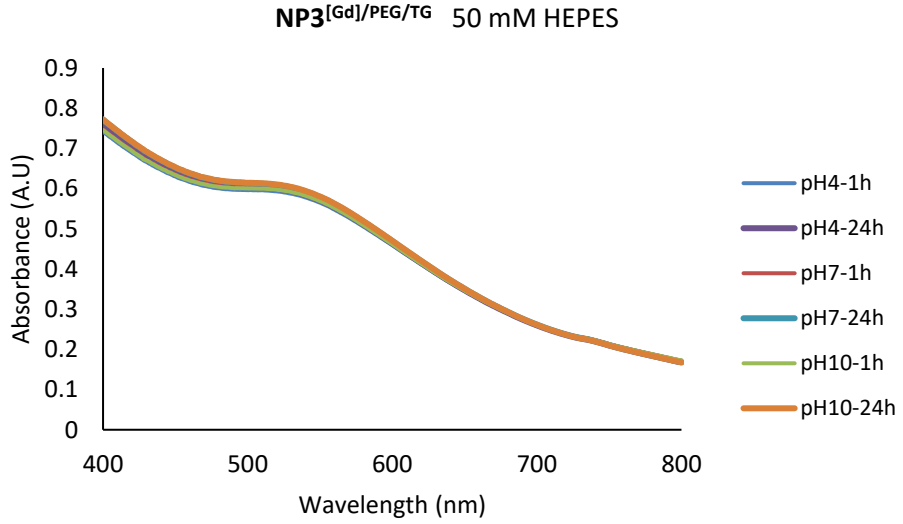

Figure S6.4-7 *UV-vis spectra of **NP3** at various pH values over time.*

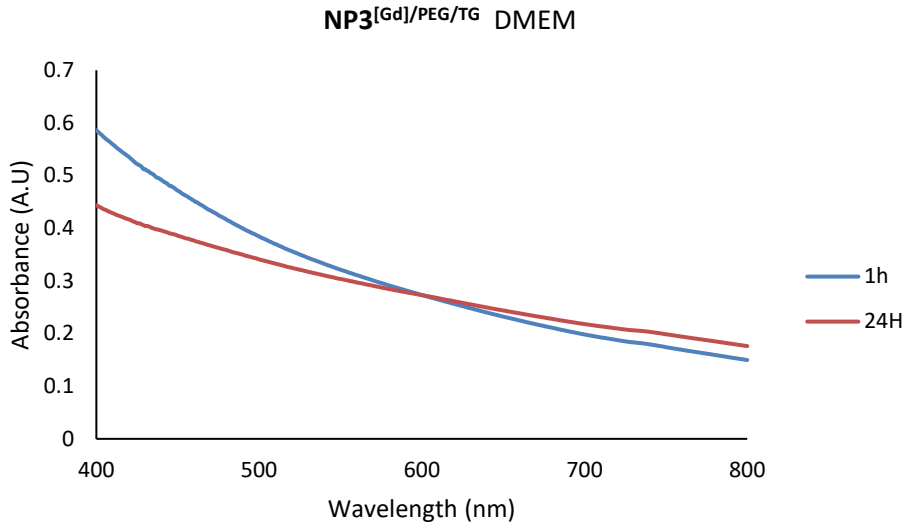

*Figure S6.4-8 UV-vis spectra of **NP3** in DMEM over time.*

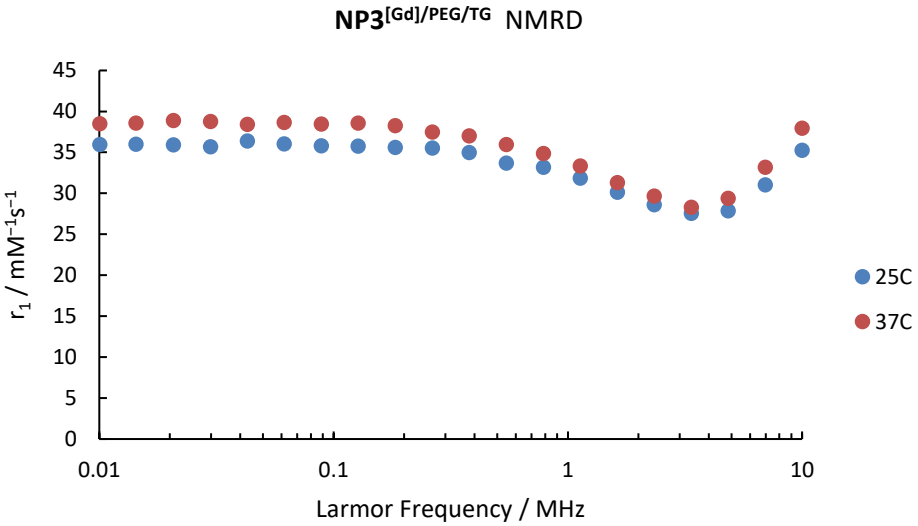

*Figure S6.4-9 NMRD profiles of **NP3** at 25 and 37 °C.*

*Table S6.4-1 Zeta-potential and size of **NP1**.*

Zeta potential / mV	− 35.6
TEM diameter / nm	3.72 ± 0.69

*Table S6.4-2 Ratios of Au to Gd determined by ICP and overall relaxivity for **NP3***

	Ratio (Au/Gd)	**NP r_1 (10 MHz) at 37 °C**
NP3[Gd]/PEG/TG	37/1	2330

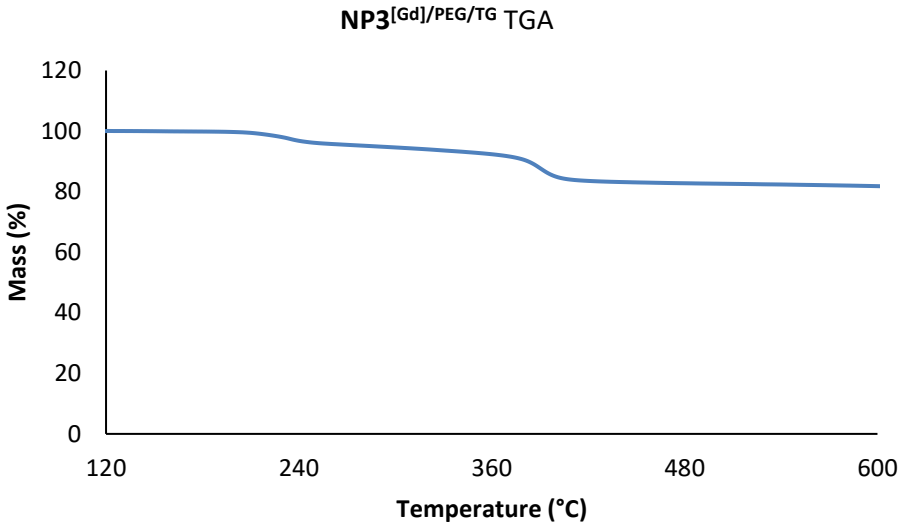

*Figure S6.4-10 TGA data for **NP3**.*

S6.5 Characterization of NP4[Gd]/PEG/FA (1:0.05:0.01)

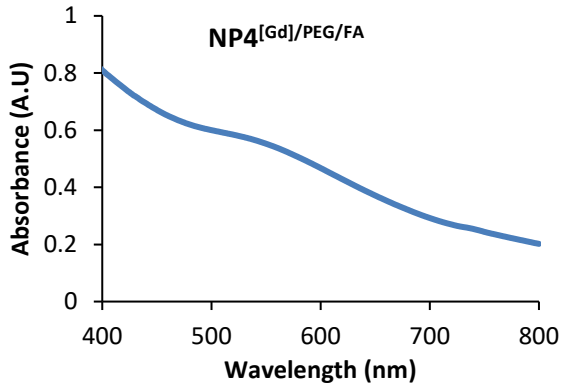

*Figure S6.5-1 UV-vis spectrum of **NP4**.*

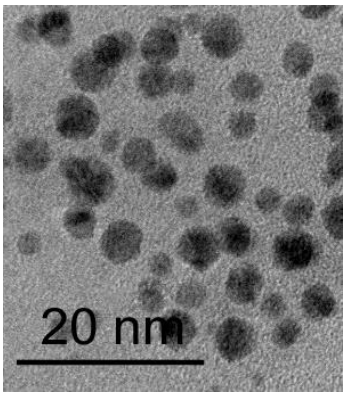

*Figure S6.5-2 TEM image of **NP4**.*

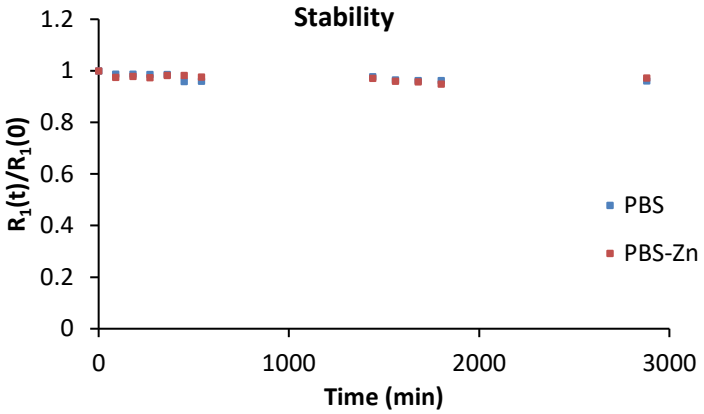

*Figure S6.5-3 Relaxivity of **NP4** between t = 0 and t = 2610 minutes on addition of Zn^{2+} (2 eq per Gd) in a transmetallation experiment at 37 °C.*

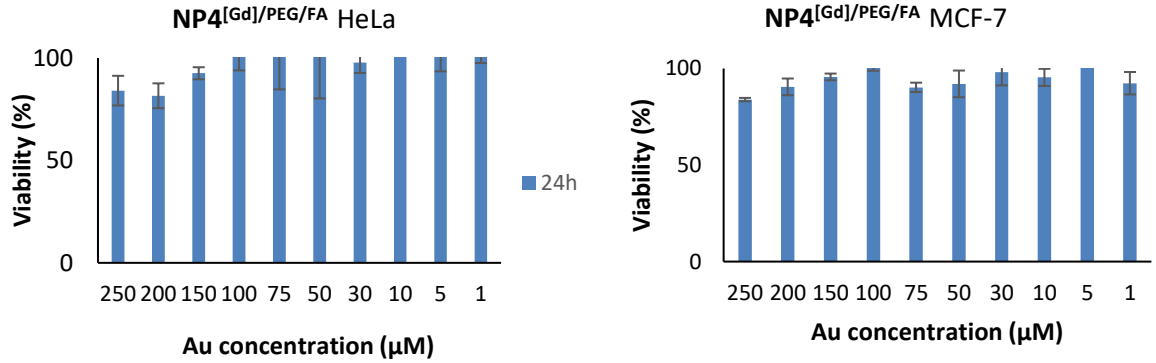

*Figure S6.5-4 Cell viability of HeLa and MCF-7 cells incubated with different concentrations of **NP4** after 24h.*

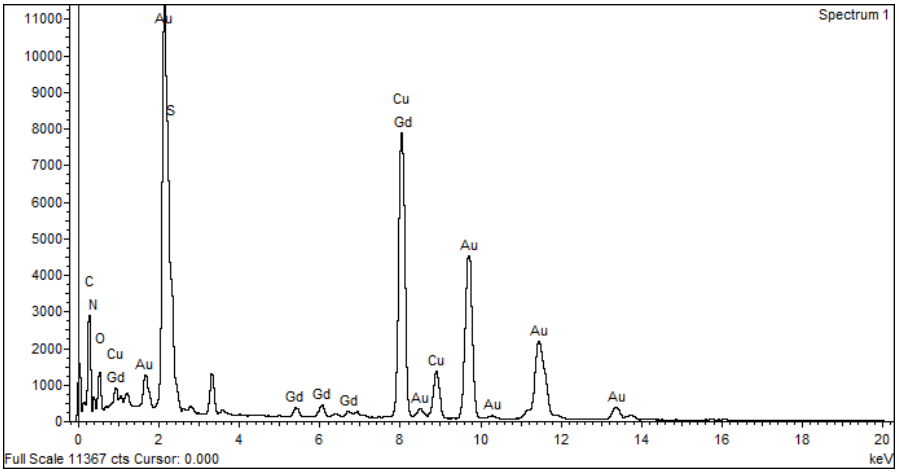

*Figure S6.5-5 EDX data for **NP4**.*

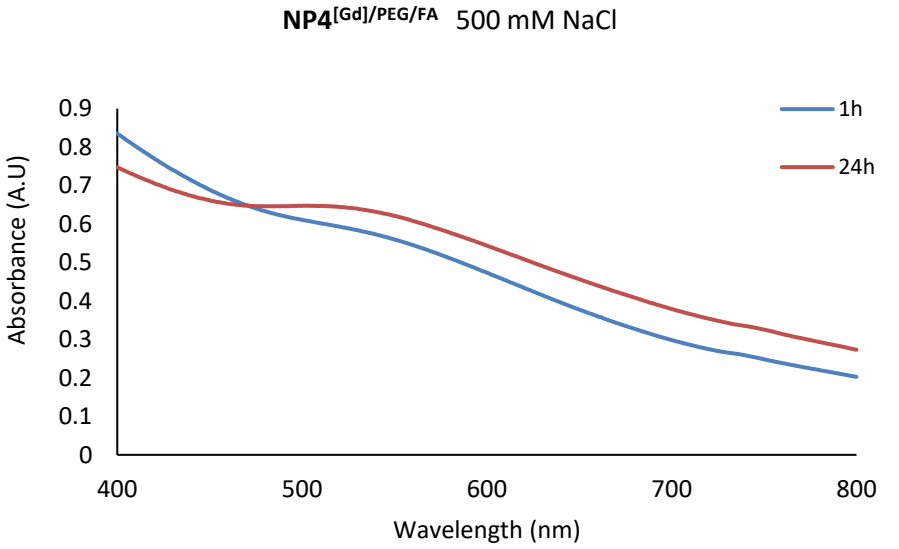

*Figure S6.5-6 UV-vis spectra of **NP4** at various salt concentrations over time.*

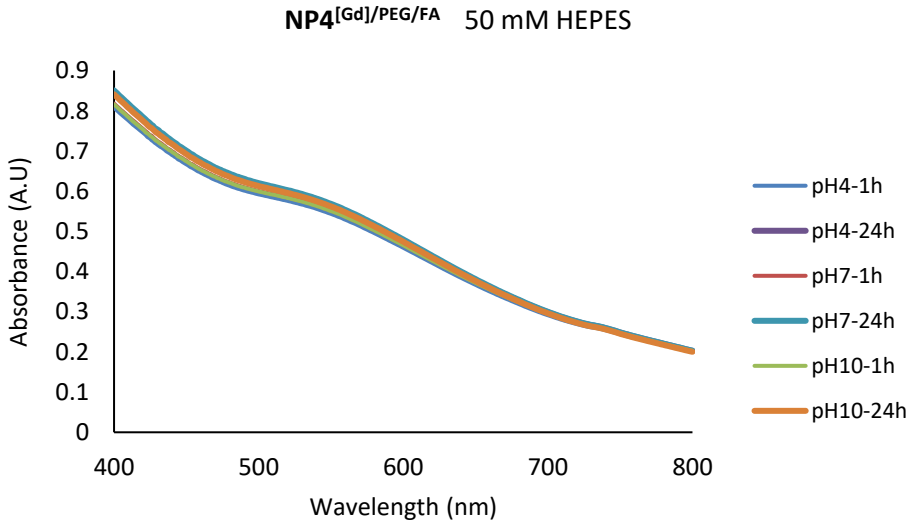

*Figure S6.5-7 UV-vis spectra of **NP4** at various pH values over time.*

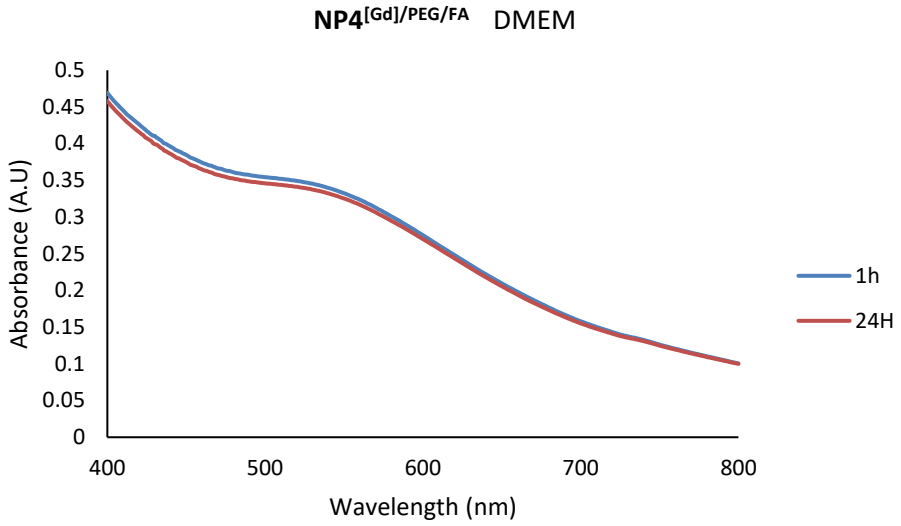

*Figure S6.5-8 UV-vis spectra of **NP4** in DMEM over time.*

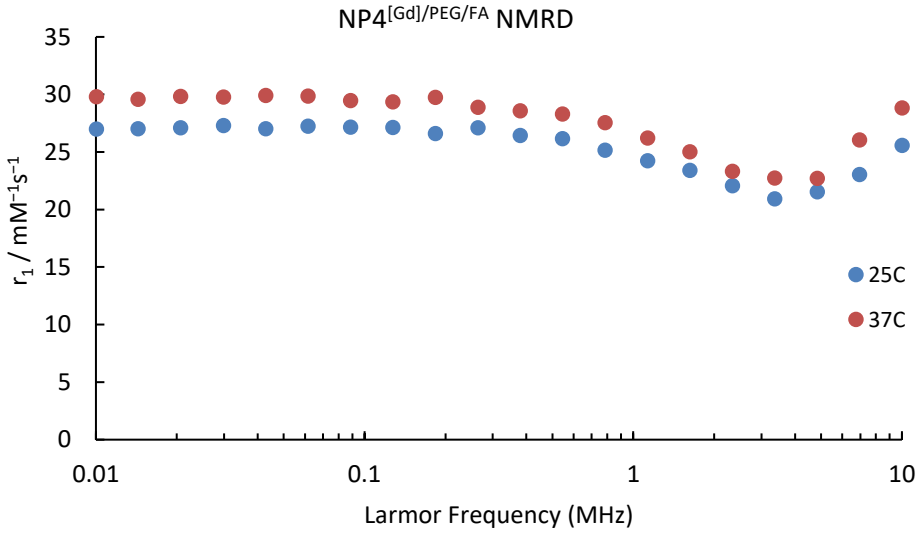

*Figure S6.5-9 NMRD profiles for **NP4** at 25 and 37 °C.*

*Table S6.5-1 Zeta potential and size of **NP4**.*

Zeta potential / mV	− 39.0
TEM diameter / nm	3.72 ± 0.73

*Table S6.5-2 Ratios of Au to Gd determined by ICP and overall relaxivity of **NP4***

	Ratio (Au/Gd)	**NP r_1 (10 MHz) at 37 °C**
NP4[Gd]/PEG/FA	Au_{2502}/Gd_{169} (15:1)	4874

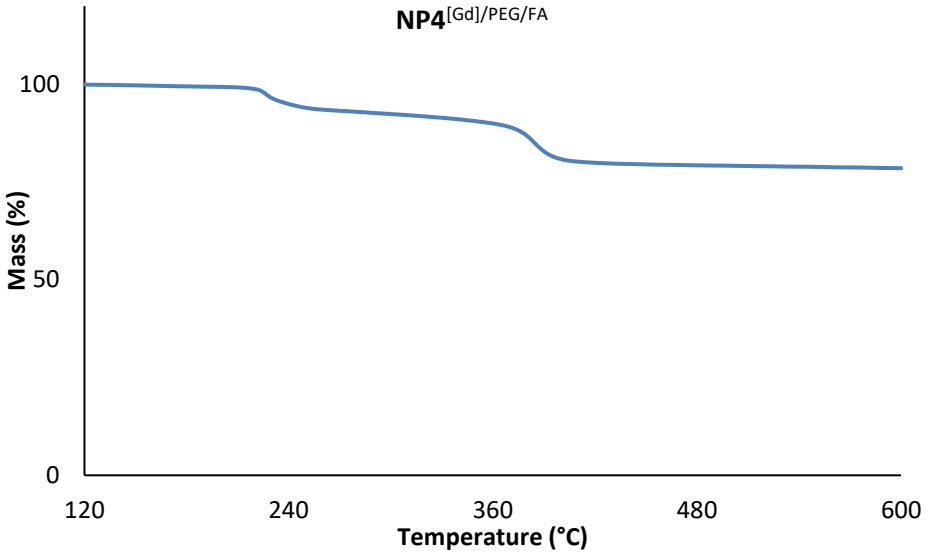

*Figure S6.5-10 TGA data for **NP4**.*

S6.6 Characterization of NP5[Gd]/PEG/TG/FA (1:0.05:0.05:0.01)

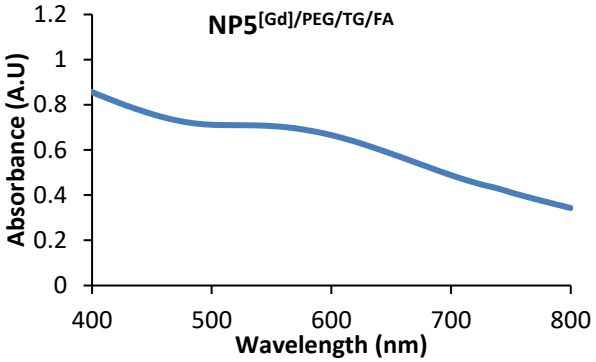

*Figure S6.6-1 UV-vis spectrum of **NP5**.*

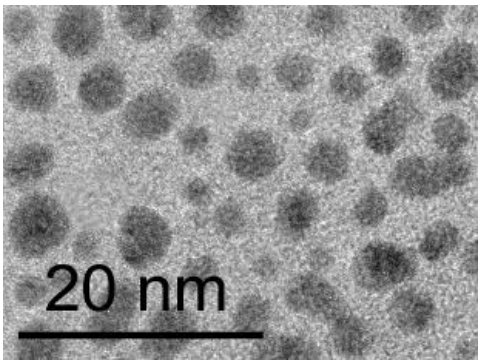

*Figure S6.6-2 TEM image of **NP5**.*

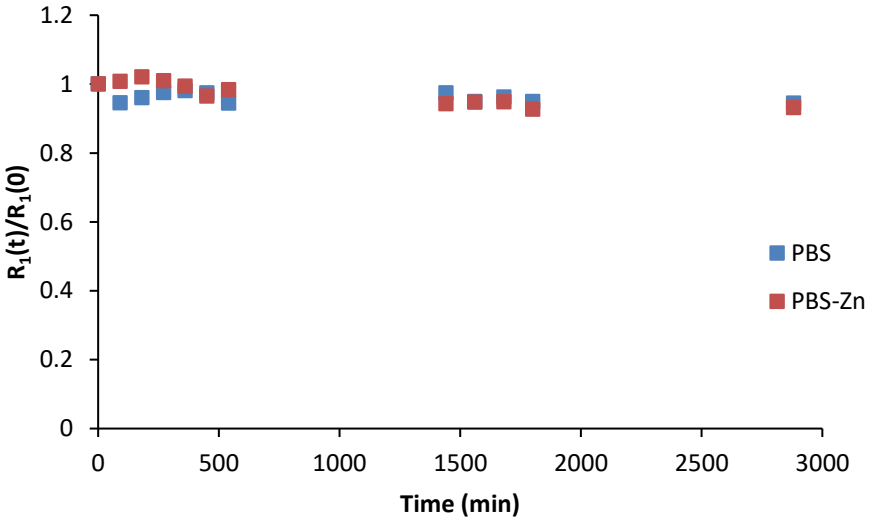

*Figure S6.6-3 Relaxivity of **NP5** between t = 0 and t = 2610 minutes on addition of Zn^{2+} (2 eq. per Gd) in a transmetallation experiment at 37 °C.*

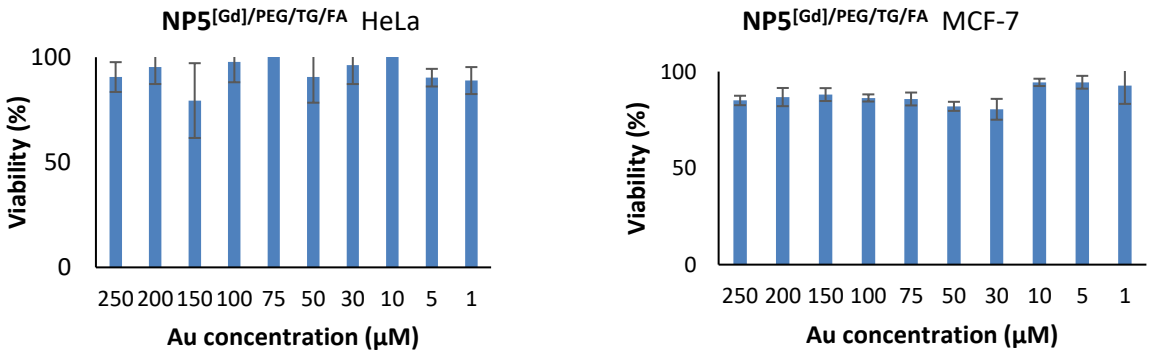

*Figure S6.6-4 Cell viability of HeLa and MCF-7 cells incubated with different concentrations of **NP5** after 24h.*

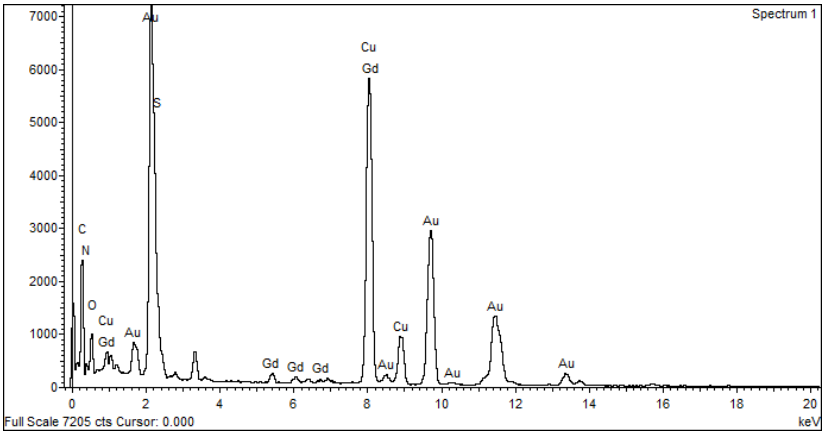

*Figure S6.6-5 EDX data for **NP5***

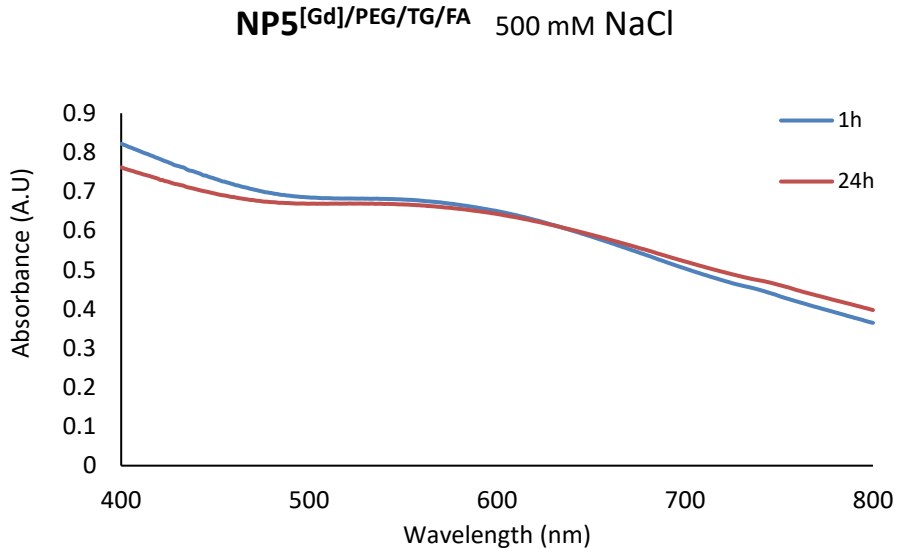

*Figure S6.6-6 UV-vis spectra of **NP5** at various salt concentrations over time.*

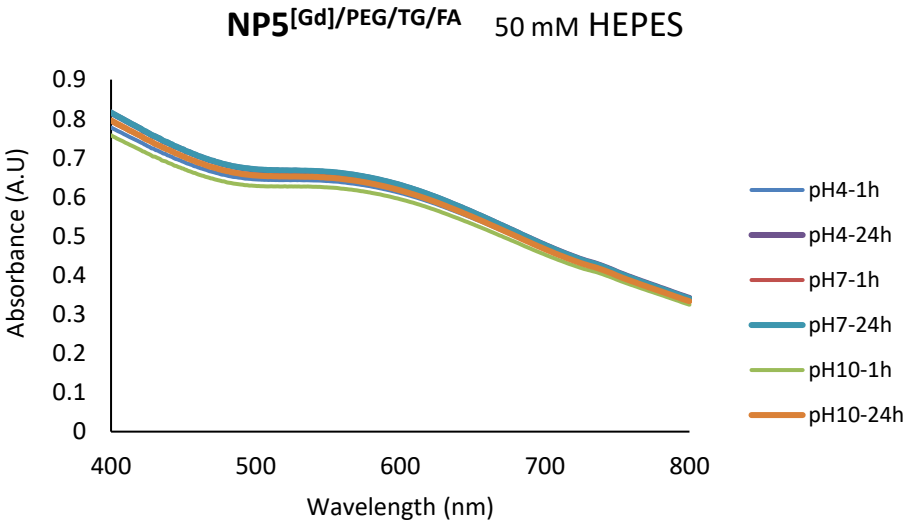

*Figure S6.6-7 UV-vis spectra of **NP5** at various pH values over time.*

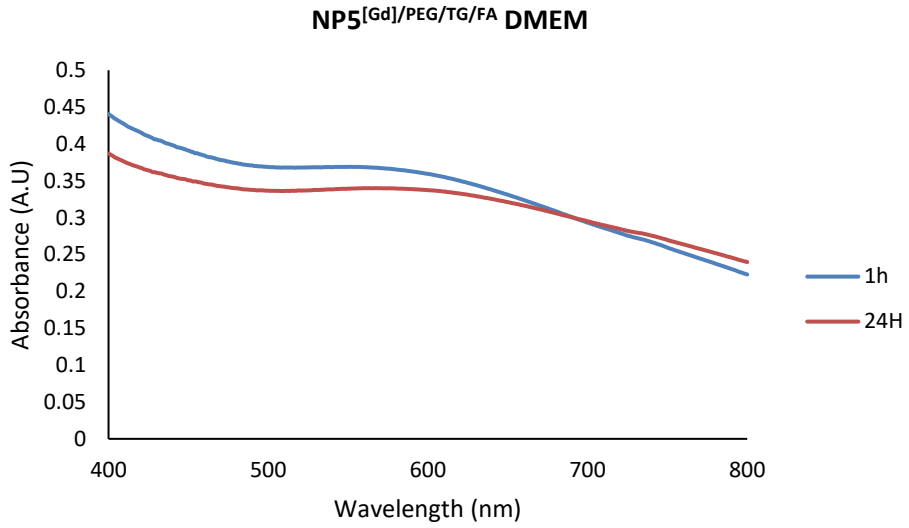

*Figure S6.6-8 UV-vis spectra of **NP5** in DMEM over time.*

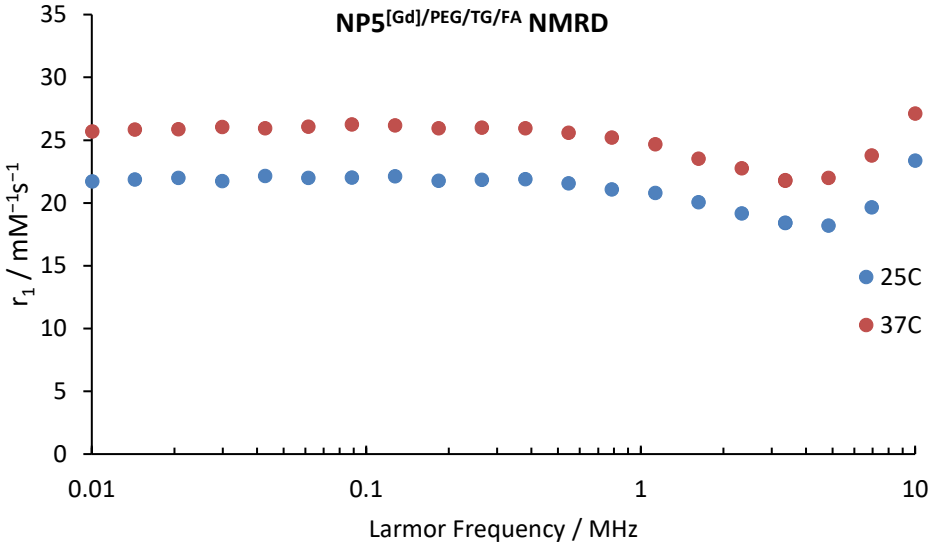

*Figure S6.6-9 NMRD profiles for **NP5** at 25 and 37 °C.*

*Table S6.6-1 Zeta potential, DLS and size of **NP5**.*

Zeta potential / mV	− 37.1
TEM diameter / nm	3.83 ± 0.59
Hydrodynamic diameter/ nm	24.93 ± 4.05

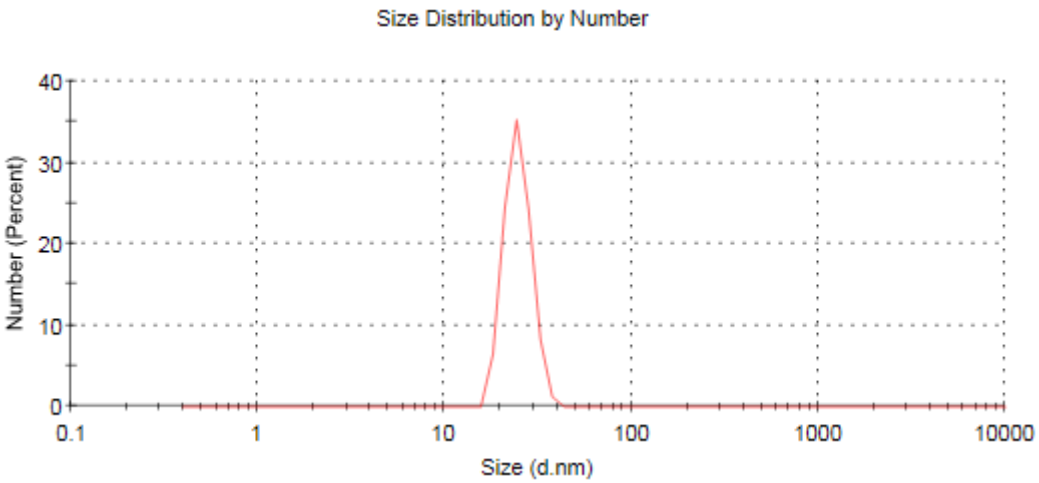

*Figure S6.6-10 DLS data for **NP5**.*

*Table S6.6-2 Ratios of Au to Gd determined by ICP and overall relaxivity of **NP5**.*

ICP data	**Ratio (Au/Gd)**	**NP r_1 (10 MHz)**
NP5$^{[Gd]PEG/FA/TG}$	Au_{2709}/Gd_{100} (27:1)	2932

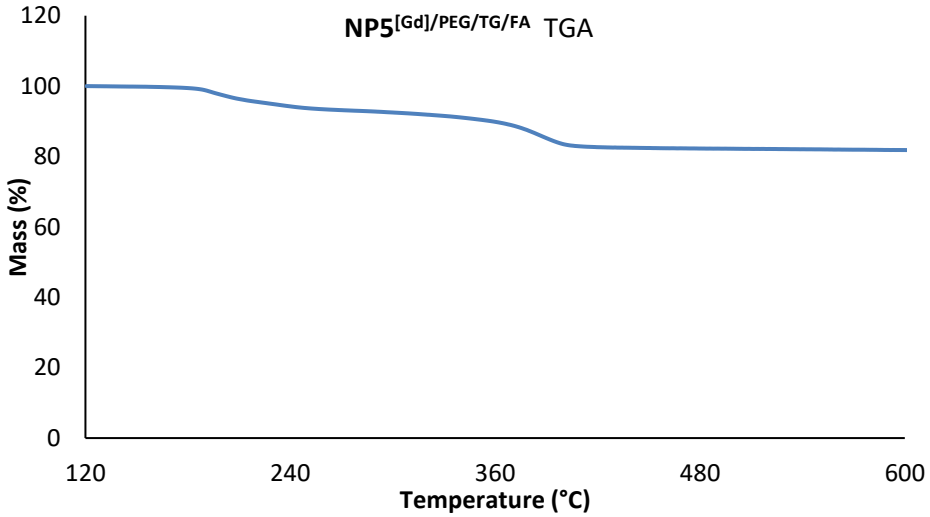

*Figure S6.6-11 TGA data for **NP5**.*

S6.7 Characterization of NP6[Gd]/Porph (1:0.5)

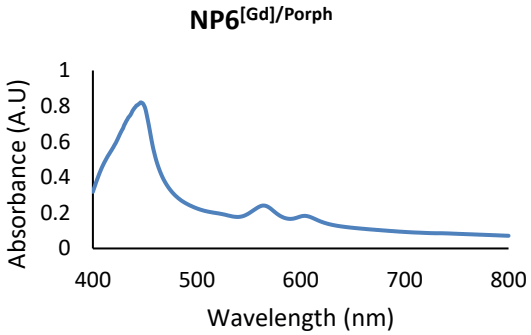

*Figure S6.7-1 UV-vis spectrum of **NP6**.*

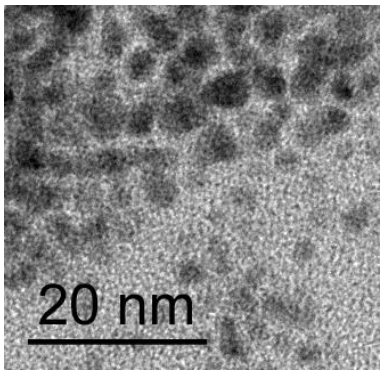

*Figure S6.7-2 TEM image of **NP6**.*

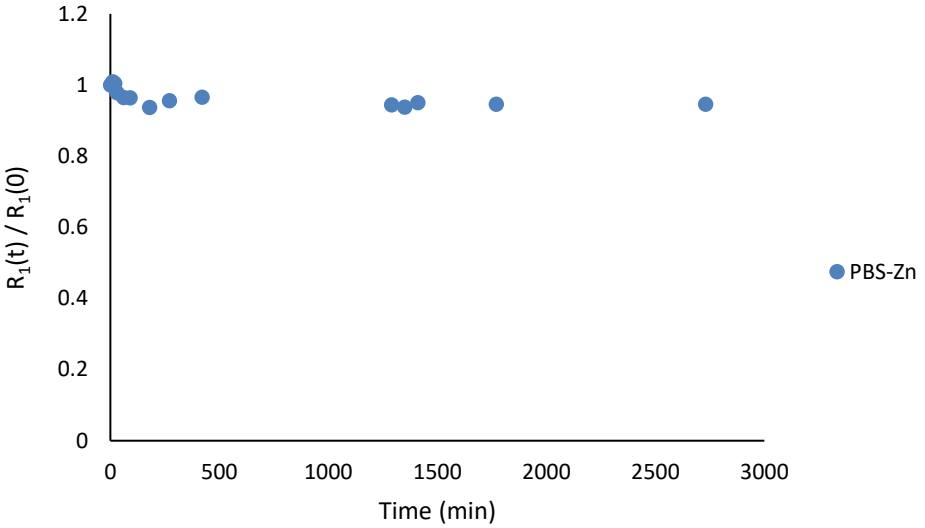

*Figure S6.7-3 Relaxivity between t = 0 and t = 2610 minutes on addition of Zn^{2+} (2 eq per Gd) in a transmetallation experiment at 37 °C for **NP6**.*

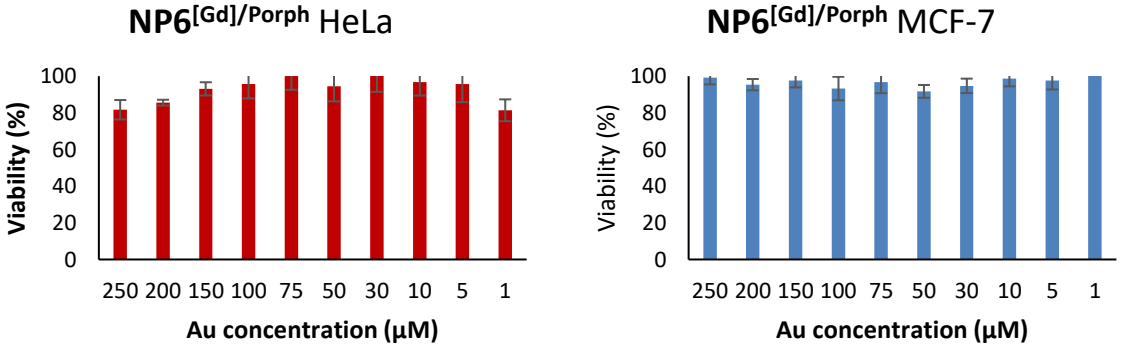

*Figure S6.7-4 Cell viability of HeLa and MCF-7 cells incubated with different concentrations of **NP6** after 24h.*

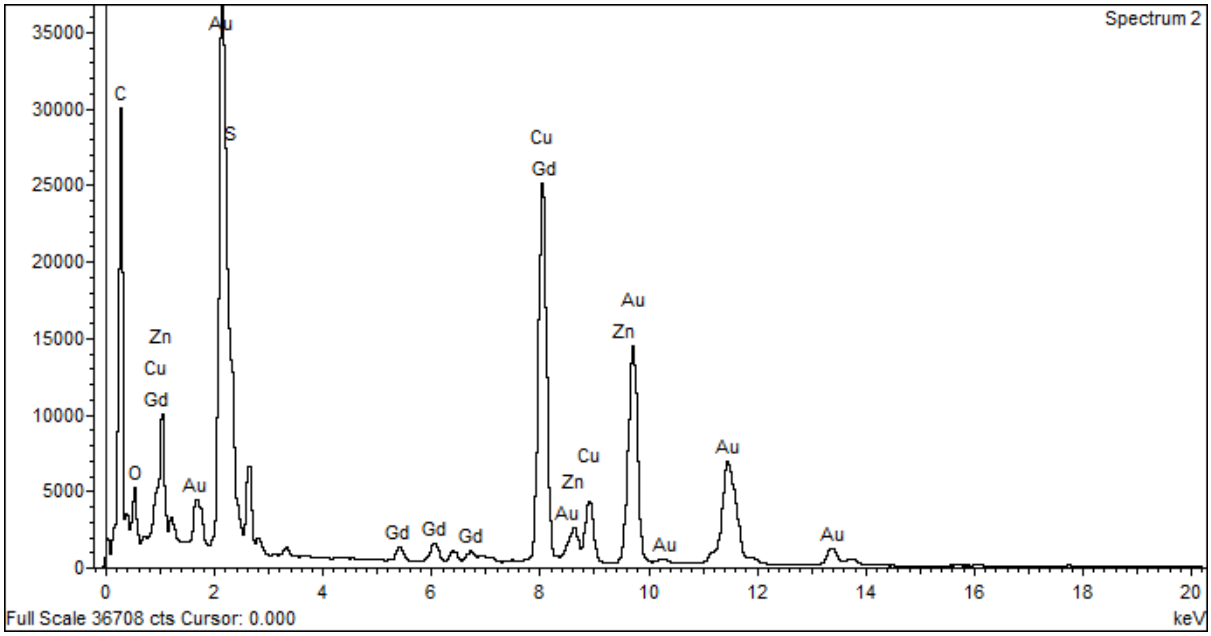

*Figure S6.7-5 EDX data for **NP6**.*

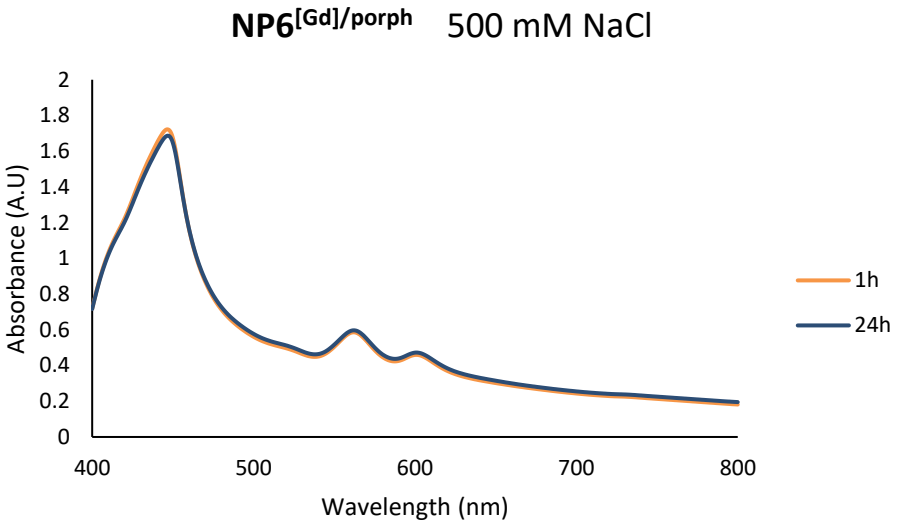

*Figure S6.7-6 UV-vis spectra of **NP6** at various salt concentrations over time.*

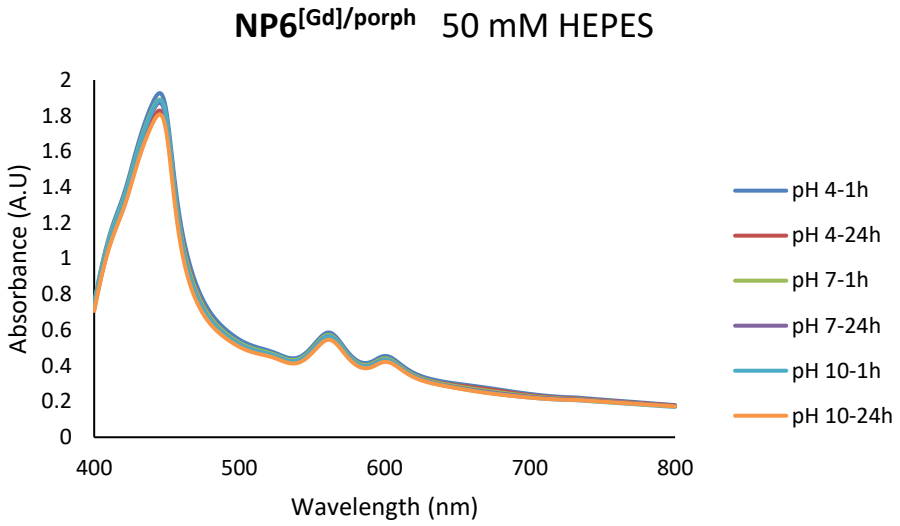

Figure S6.7-7 *UV-vis spectra of* ***NP6*** *at various pH values over time.*

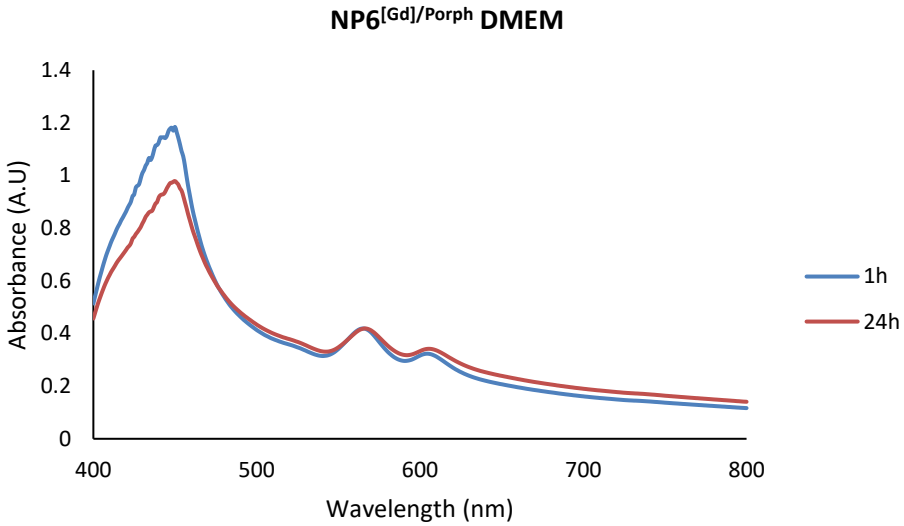

Figure S6.7-8 UV-vis spectra of ***NP6*** *in DMEM over time.*

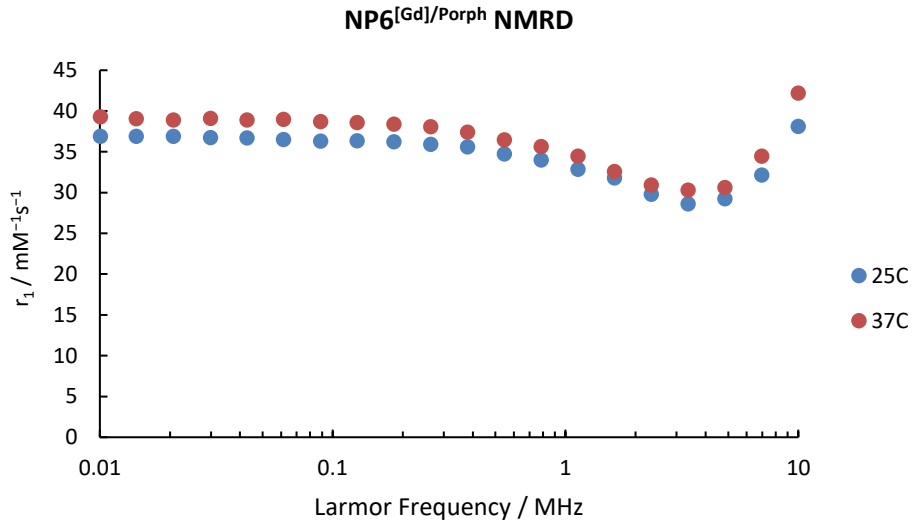

*Figure S6.7-9 NMRD profiles of **NP6** at 25 and 37 °C.*

*Table S6.7-1 Zeta potential and size of **NP6**.*

Zeta potential / mV	− 33.1
TEM diameter / nm	2.77 ± 0.49

*Table S6.7-2 Ratios of Au to Gd determined by ICP-OES and overall relaxivity of **NP6***

	Ratio (Au/Gd)	**NP r_1 (10 MHz) at 37 °C**
NP6[Gd]/Porph	12:1	3713

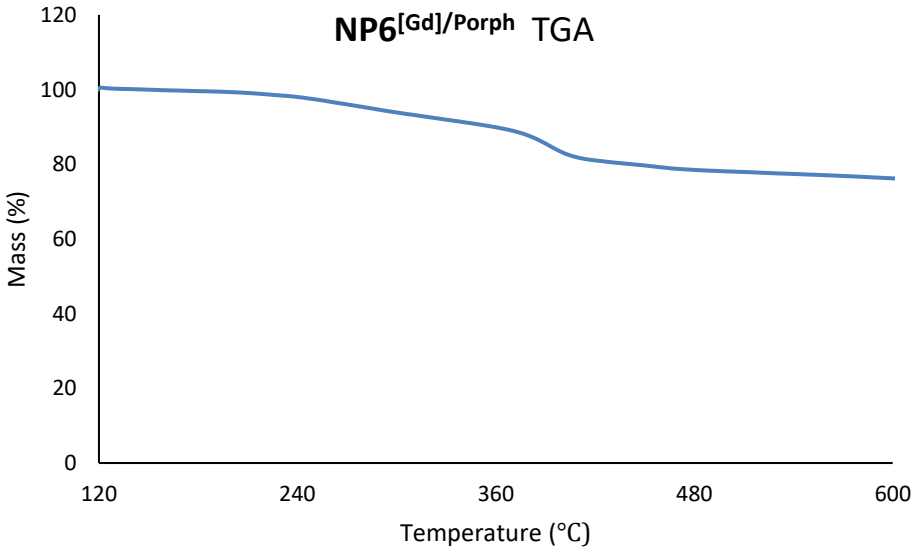

*Figure S6.7-10 TGA data for **NP6**.*

S6.8 Characterization of NP7[Gd]/PEG/Porph (1:0.05:0.5)

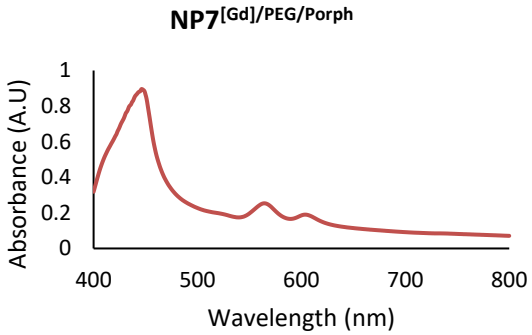

*Figure S6.8-1 UV-vis spectrum of **NP7**.*

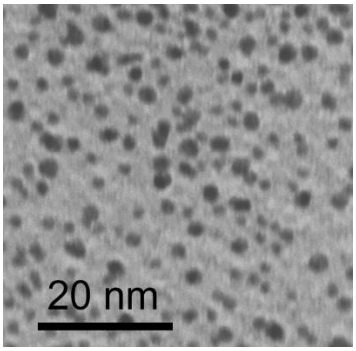

*Figure S6.8-2 TEM image of **NP7**.*

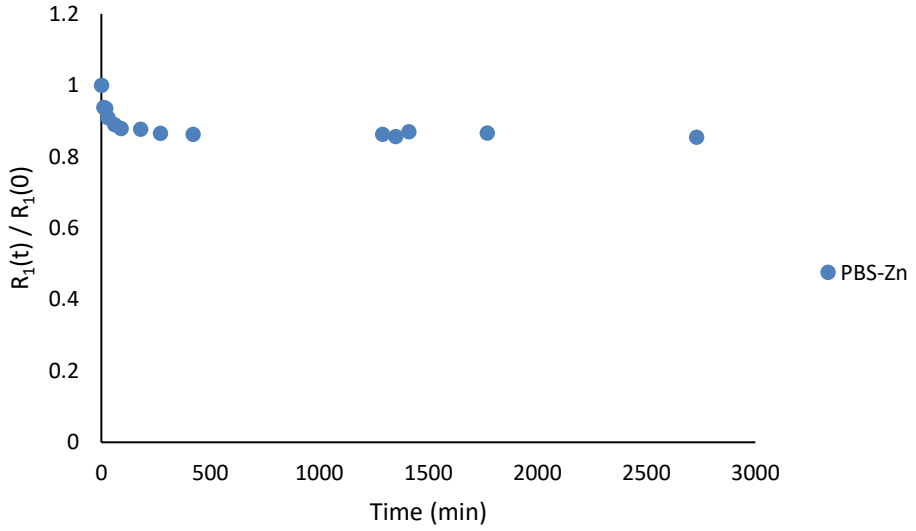

*Figure S6.8-3 Relaxivity for **NP7** values between t = 0 to t = 2610 minutes on addition of Zn^{2+} (2 eq per Gd) in a transmetallation experiment at 37 °C.*

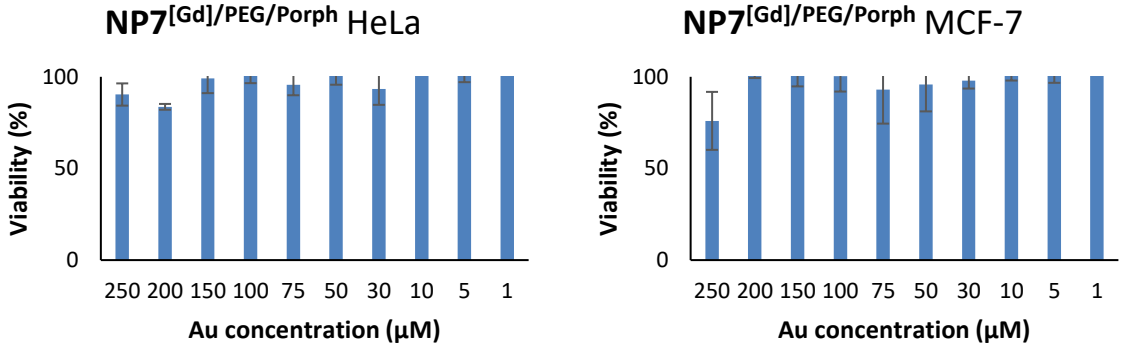

*Figure S6.8-4 Cell viability of HeLa and MCF-7 cells incubated with different concentrations of **NP7** after 24h.*

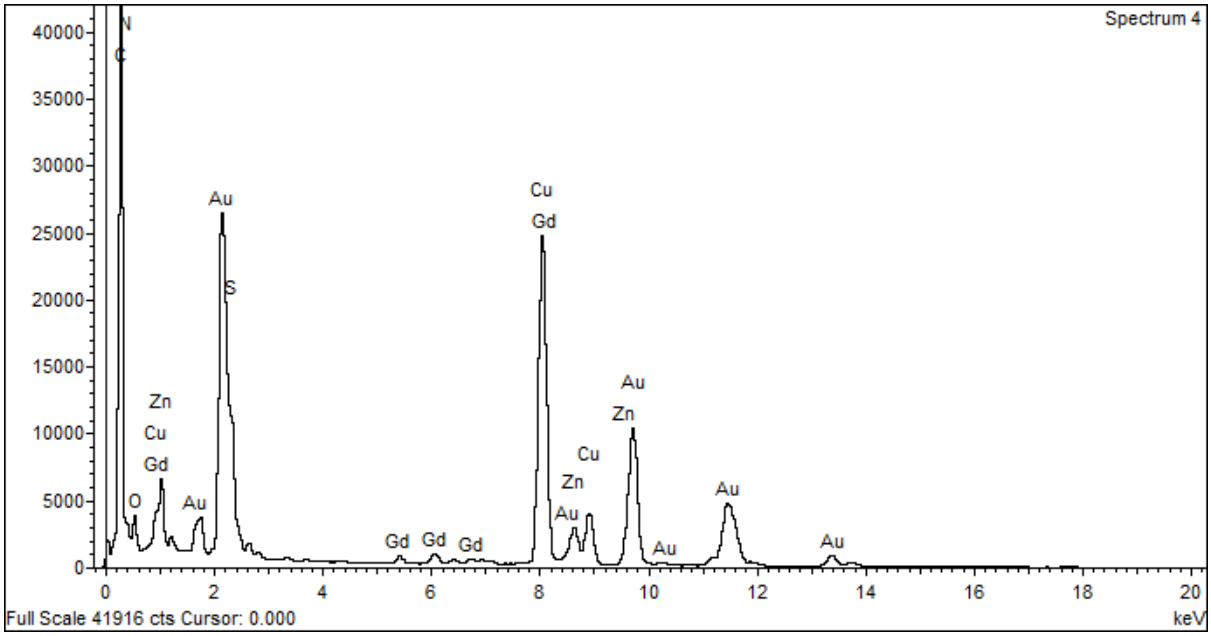

*Figure S6.8-5 EDX data for **NP7**.*

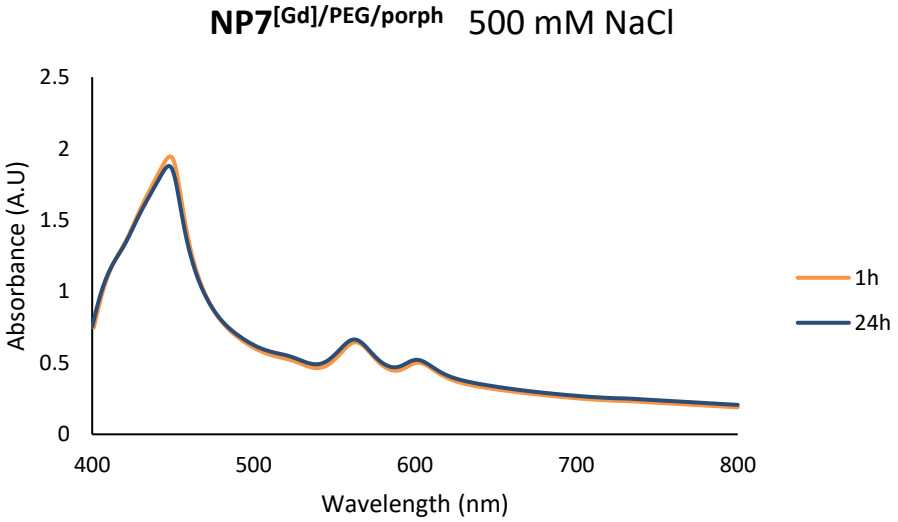

*Figure S6.8-6 UV-vis spectra of **NP7** at various salt concentrations over time.*

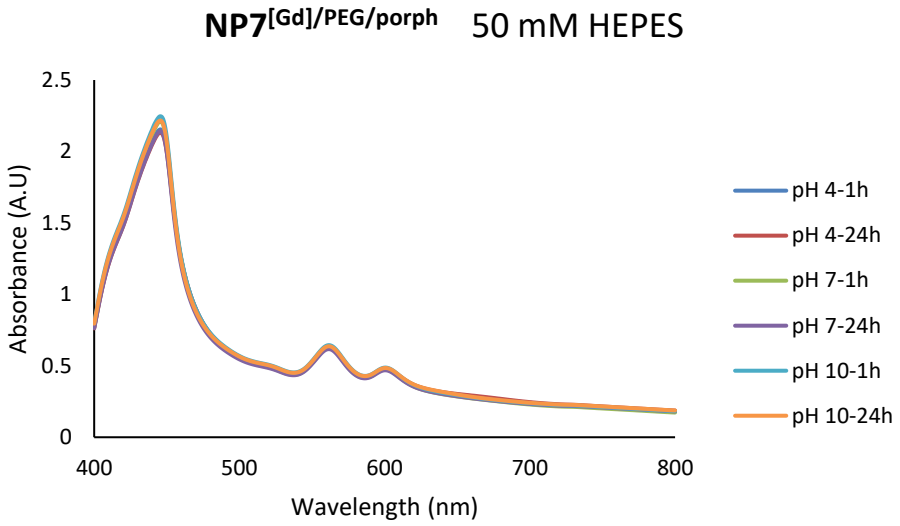

Figure S6.8-7 *UV-vis spectra of* ***NP7*** *at various pH values over time.*

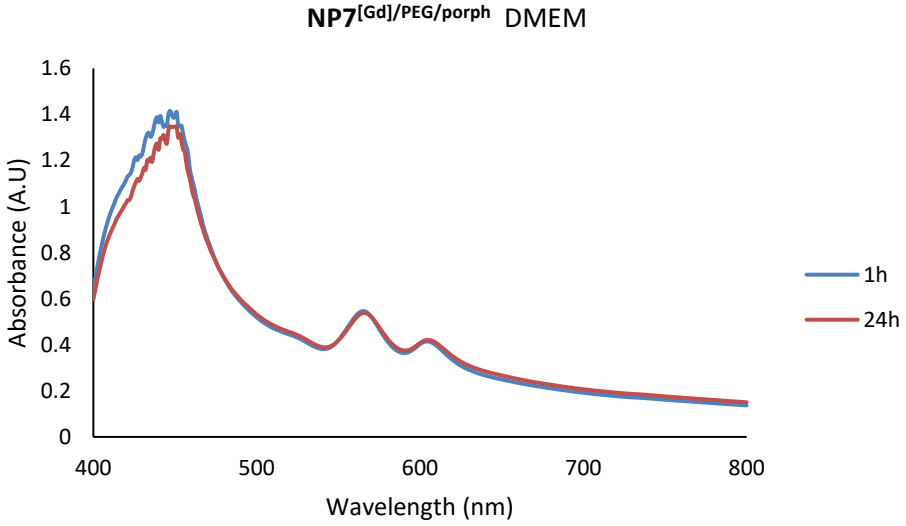

Figure S6.8-8 UV-vis spectra of ***NP7*** *in DMEM over time.*

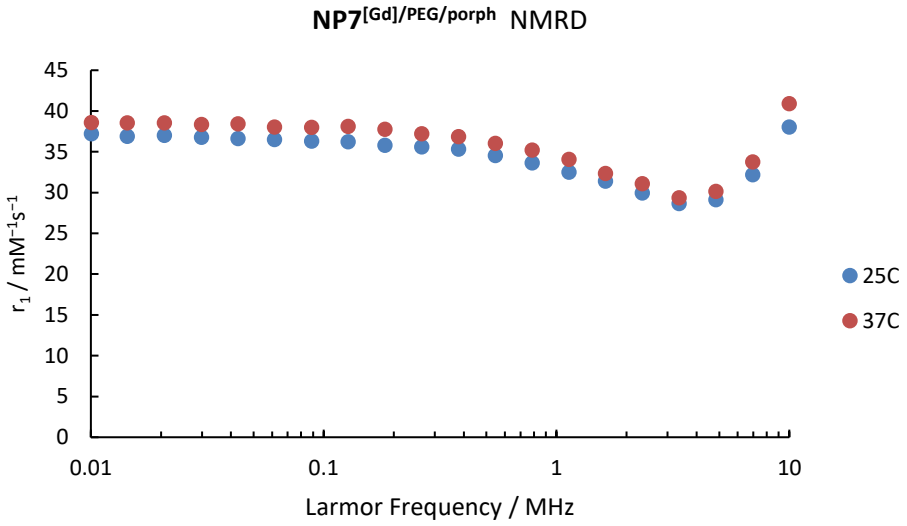

*Figure S6.8-9 NMRD profiles of **NP7** at 25 and 37 °C.*

*Table S6.8-1 Zeta potential, DLS and size of **NP7**.*

Zeta potential / mV	− 32.8
TEM diameter / nm	2.62 ± 0.53
Hydrodynamic diameter / nm	37.22 ± 5.92

Table S6.8-2 *Ratios of Au to Gd determined by ICP-OES and overall relaxivity of **NP7**.*

	Ratio (Au/Gd)	**NP r_1 (10 MHz) at 37 °C**
NP7[Gd]/PEG/Porph	13:1	2749

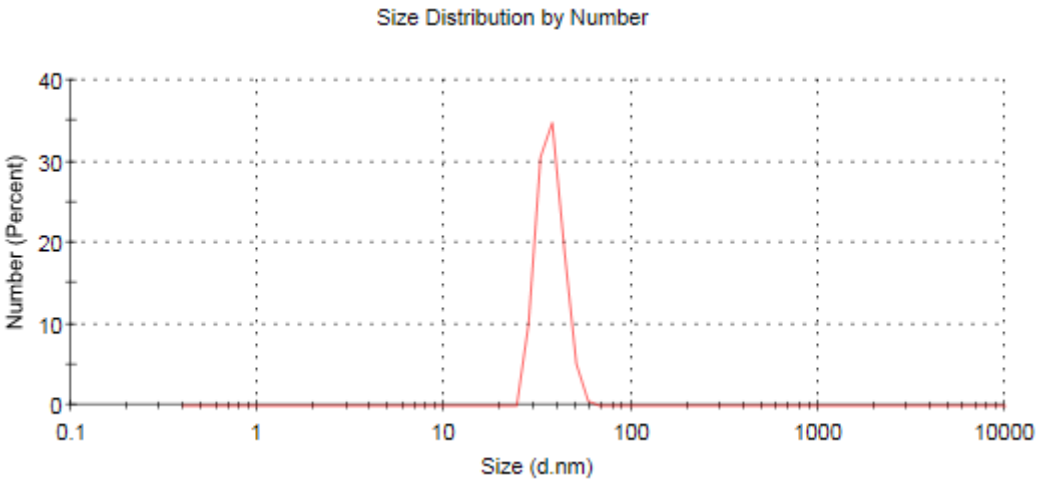

*Figure S6.8-10 DLS data for **NP7**.*

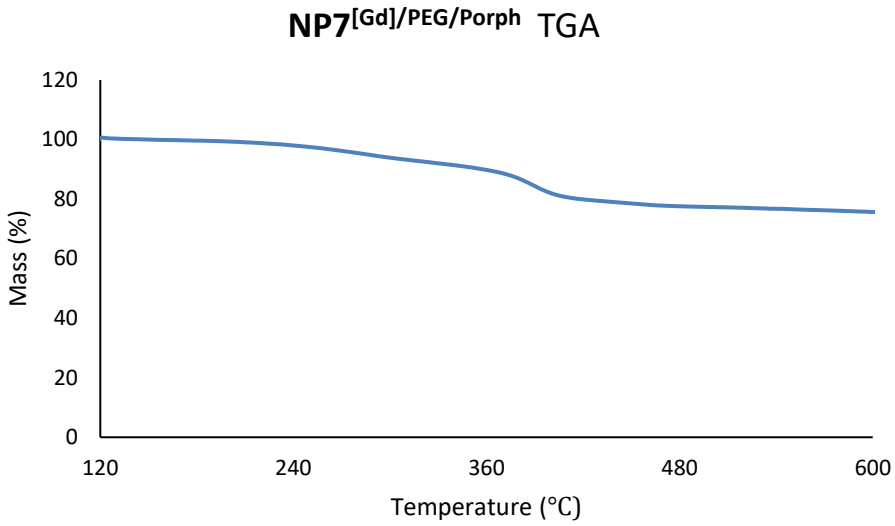

*Figure S6.8-11 TGA data for **NP7**.*

S6.9 Characterization of NP8[Gd]/PEG/FA/Porph (1:0.05:0.05:0.5)

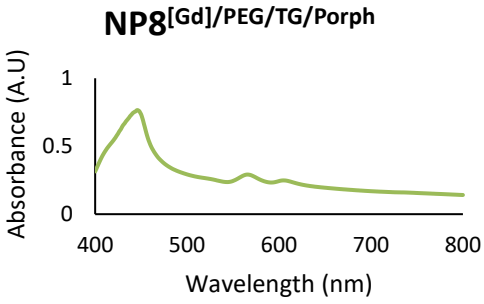

*Figure S6.9-1 UV-vis spectrum of **NP8**.*

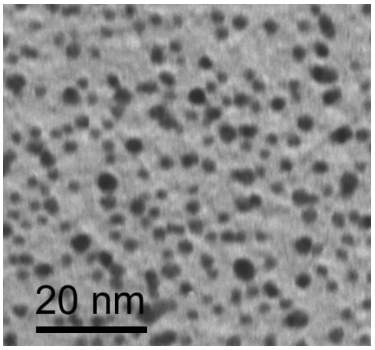

*Figure S6.9-2 TEM image of **NP8**.*

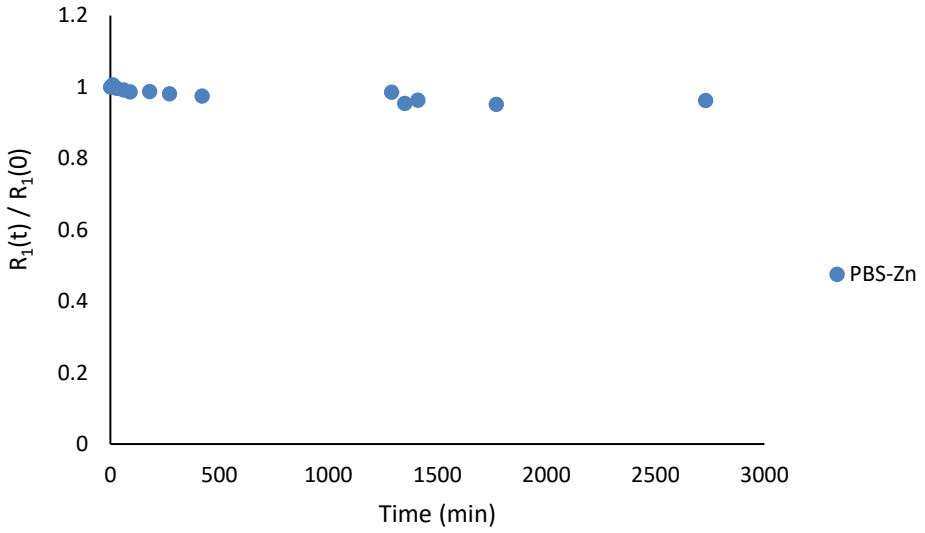

*Figure S6.9-3 Relaxivity for **NP8** between t = 0 and t = 2610 minutes on addition of Zn^{2+} (2 eq per Gd) in a transmetallation experiment at 37 °C.*

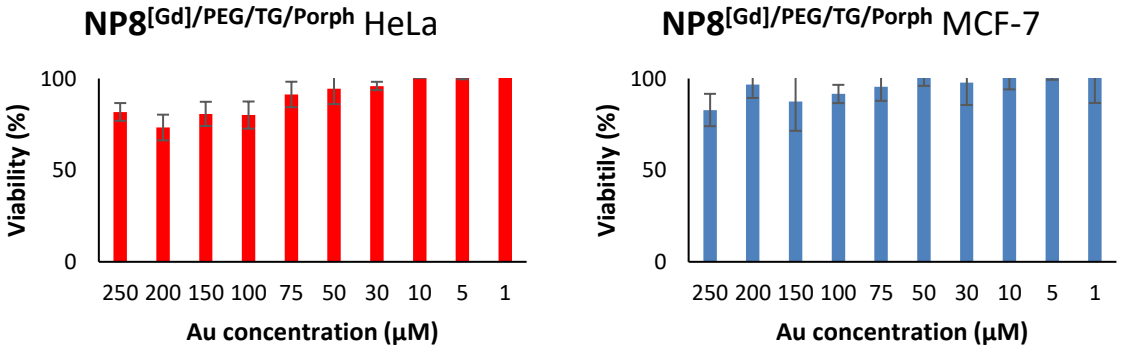

*Figure S6.9-4 Cell viability of HeLa and MCF-7 cells incubated with different concentrations of **NP8** after 24h.*

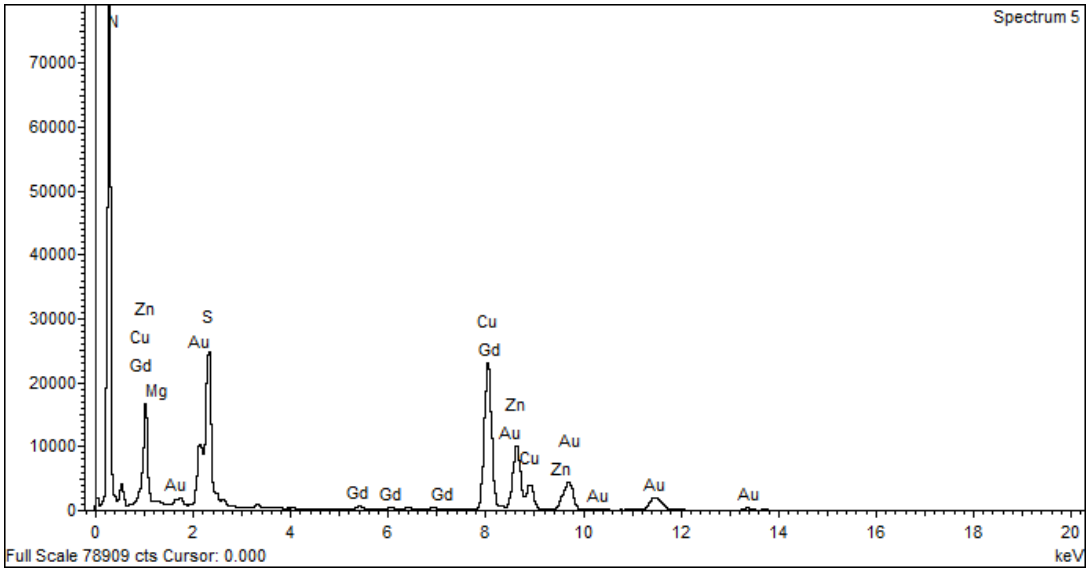

*Figure S6.9-5 EDX data for **NP8**.*

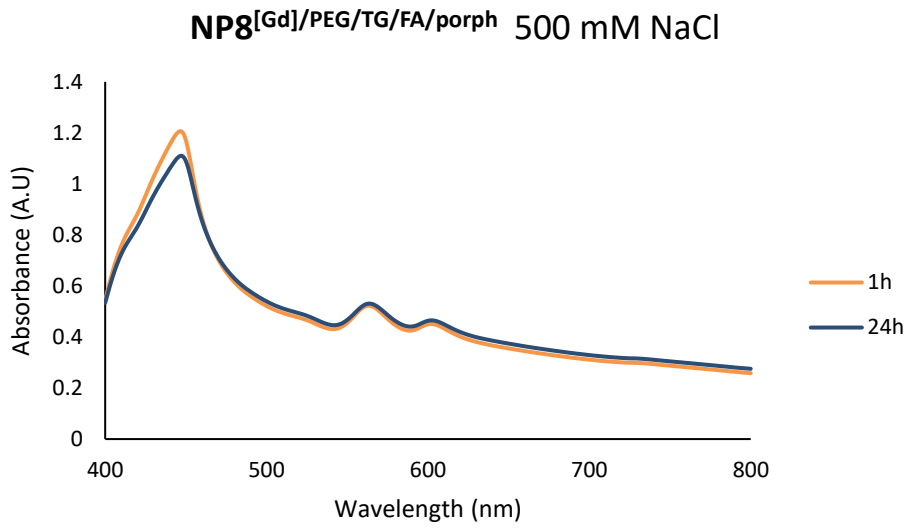

*Figure S6.9-6 UV-vis spectra of **NP8** at various salt concentrations over time.*

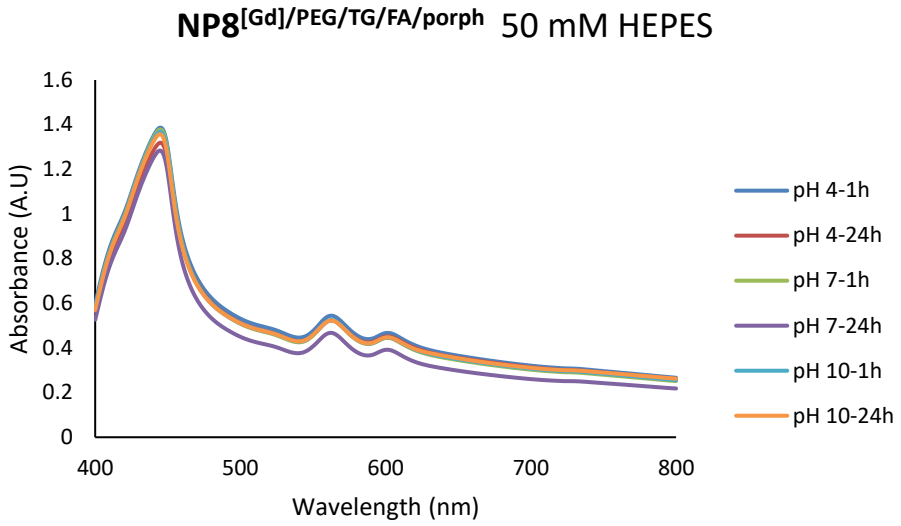

Figure S6.9-7 *UV-vis spectra of* ***NP8*** *at various pH over time.*

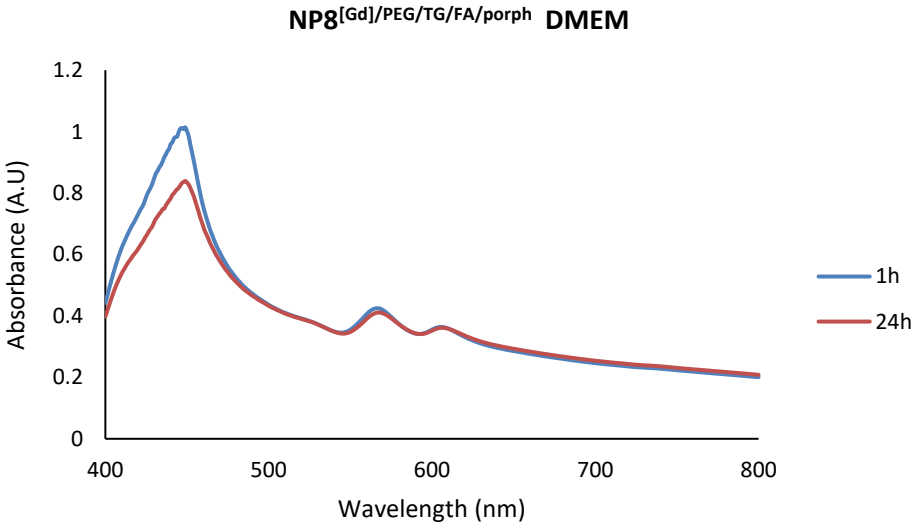

Figure S6.9-8 UV-vis spectra of ***NP8*** *in DMEM over time.*

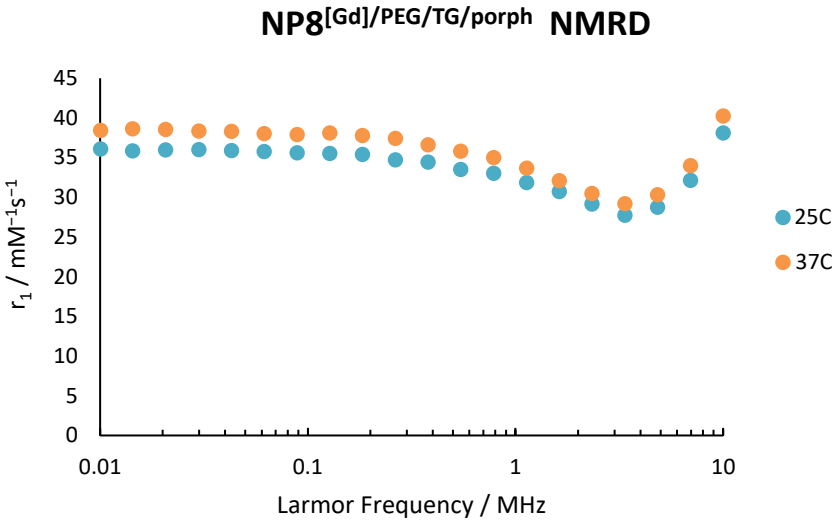

*Figure S6.9-9 NMRD profiles of **NP8** at 25 and 37 °C.*

*Table S6.9-1 Zeta potential and size of **NP8**.*

Zeta potential / mV	− 36.2
TEM diameter / nm	2.93 ± 0.53

*Table S6.9-2 Ratios of Au to Gd determined by ICP and overall relaxivity of **NP8**.*

	Ratio (Au/Gd)	**NP r_1 (10 MHz) at 37 °C**
NP8[Gd]/PEG/TG/Porph	18:1	2701

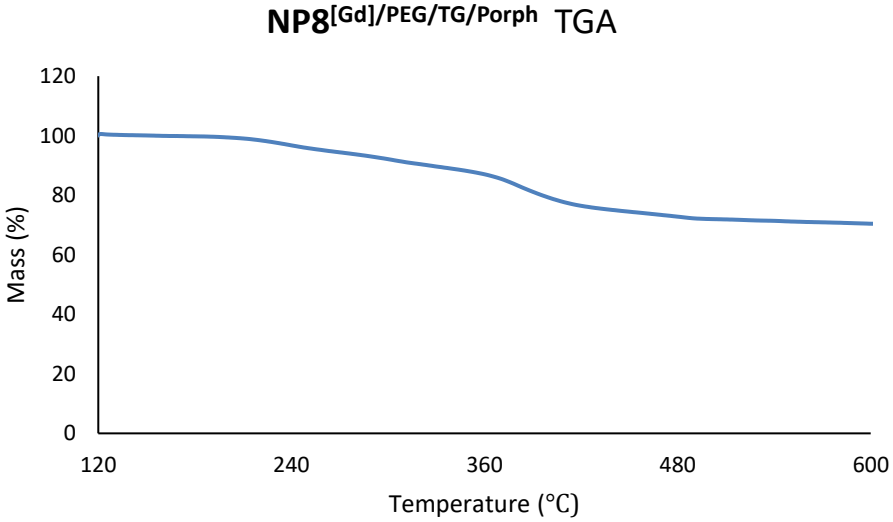

*Figure S6.9-10 TGA data for **NP8**.*

S6.10 Characterization of NP9[Gd]/PEG//FA/Porph (1:0.05:0.05:0.05:0.5)

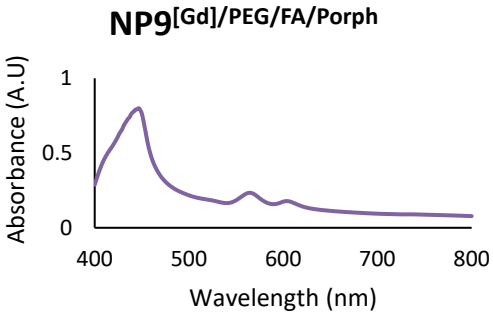

*Figure S6.10-1 UV-vis spectrum of **NP9**.*

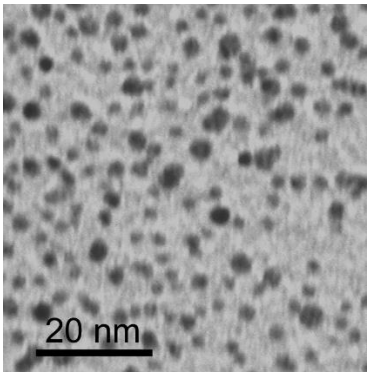

*Figure S6.10-2 TEM image of **NP9**.*

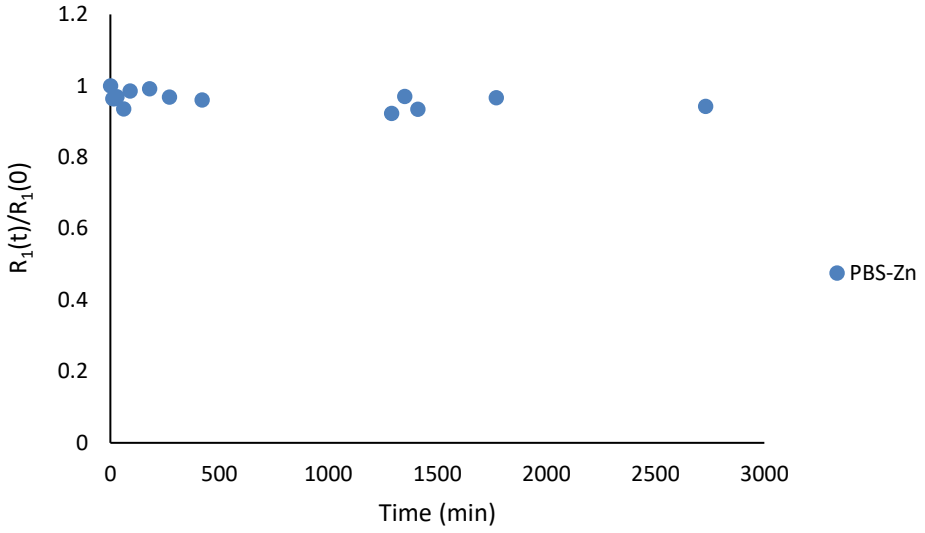

*Figure S6.10-3 Relaxivity for **NP9** between t = 0 and t = 2610 minutes for addition of Zn^{2+} (2 eq per Gd) in a transmetallation experiment at 37 °C.*

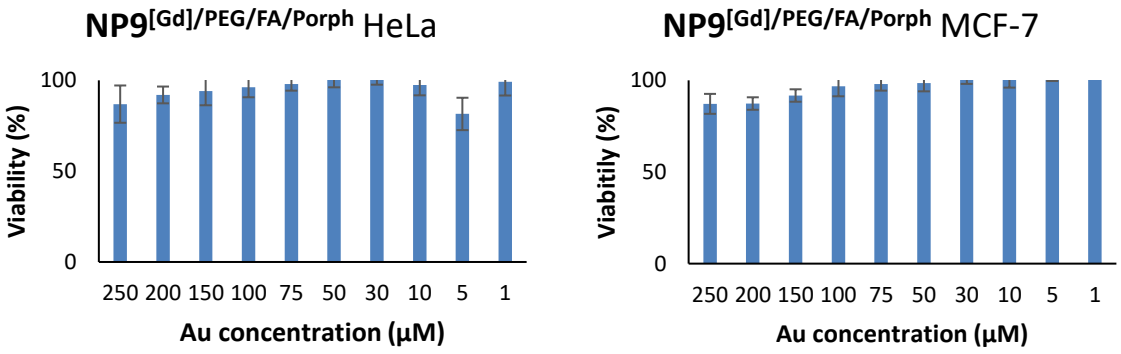

*Figure S6.10-4 Cell viability of HeLa and MCF-7 cells incubated with different concentrations of **NP9** after 24h.*

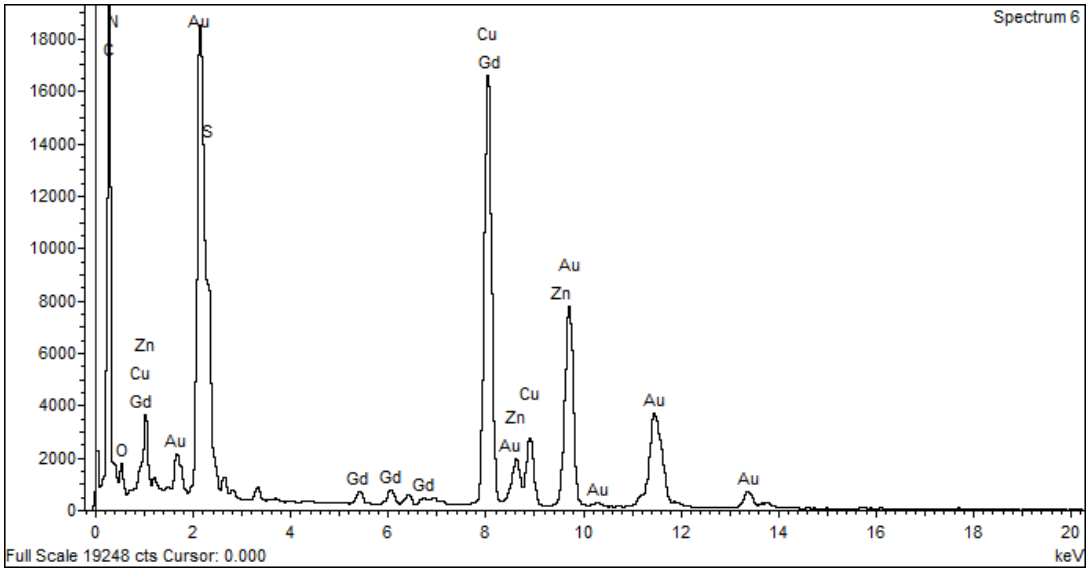

*Figure S6.10-5 EDX data for **NP9**.*

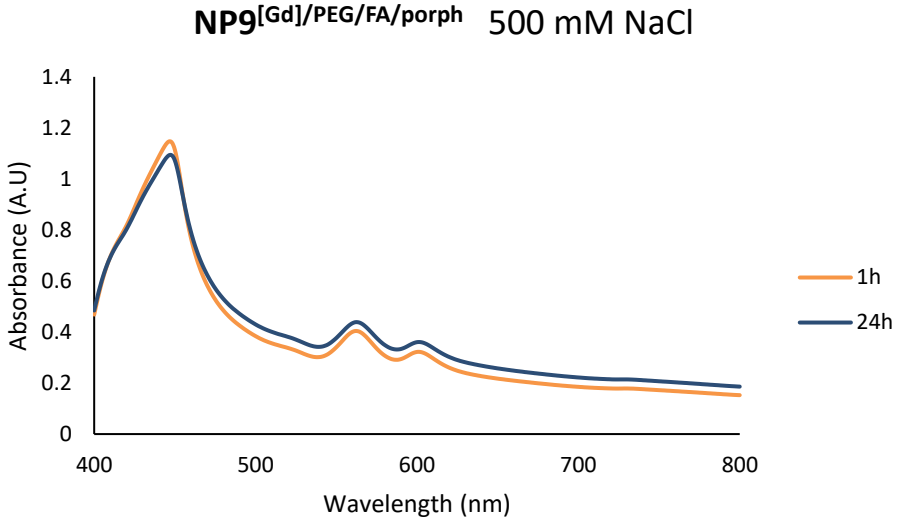

*Figure S6.10-6 UV-vis spectra of **NP9** at various salt concentrations over time.*

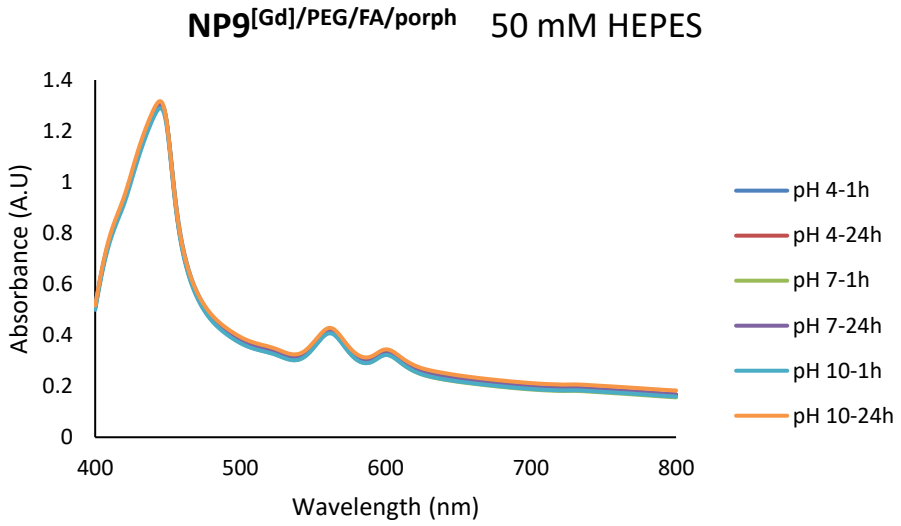

Figure S6.10-7 UV-vis spectra *of* ***NP9*** *at various pH values over time.*

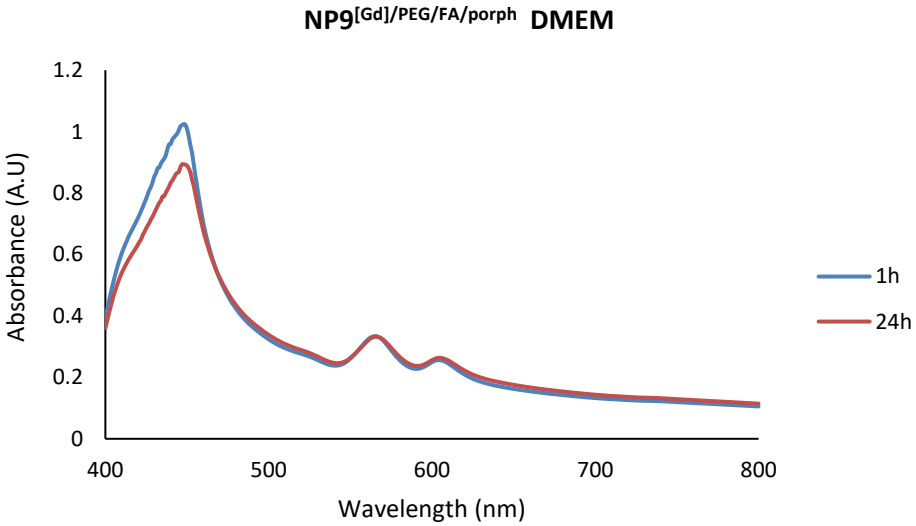

Figure S6.10-8 UV-vis spectra of ***NP9*** *in DMEM over time.*

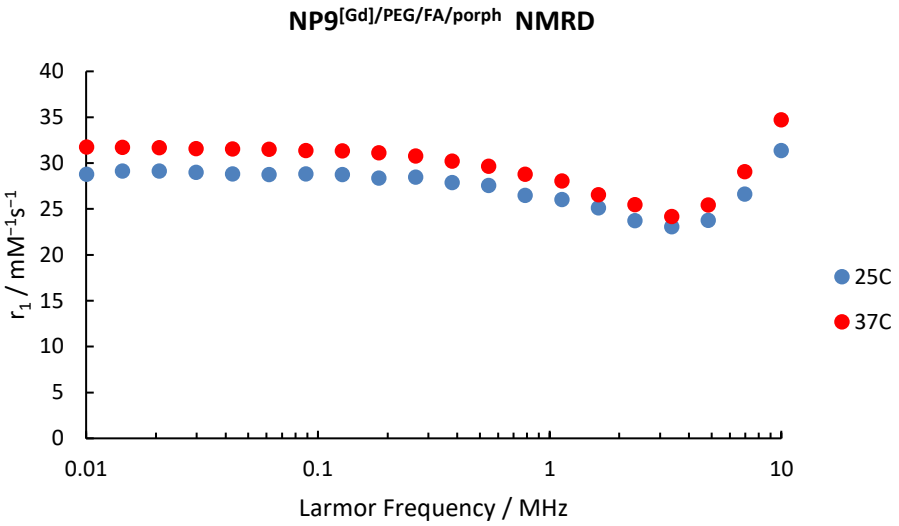

*Figure S6.10-9 NMRD profiles for **NP9** at 25 and 37 °C.*

*Table S6.10-1 Zeta potential and size of **NP9**.*

Zeta potential / mV	− 33.4
TEM diameter / nm	3.02 ± 0.63

*Table S6.10-2 Ratios of Au to Gd determined by ICP-OES and overall relaxivity of **NP9**.*

	Ratio (Au/Gd)	**NP r_1 (10 MHz) at 37 °C**
NP9[Gd]/PEG/FA/Porph	16:1	2810

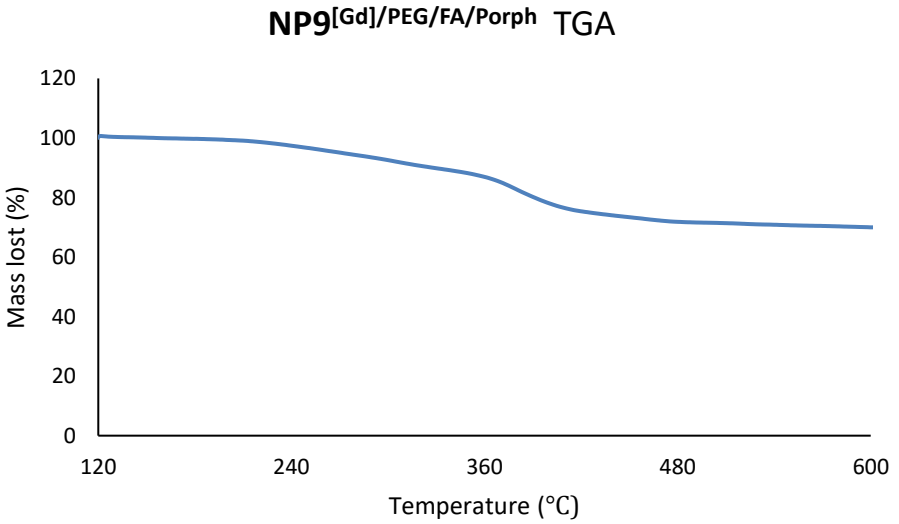

*Figure S6.10-10 TGA data for **NP9**.*

S6.11 Characterization of NP10[Gd]/PEG/TG/FA/Porph (1:0.05:0.05:0.05:0.5)

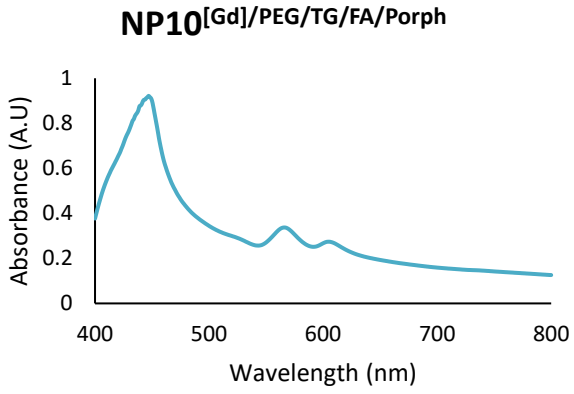

*Figure S6.11-1 UV-vis spectrum of **NP10**.*

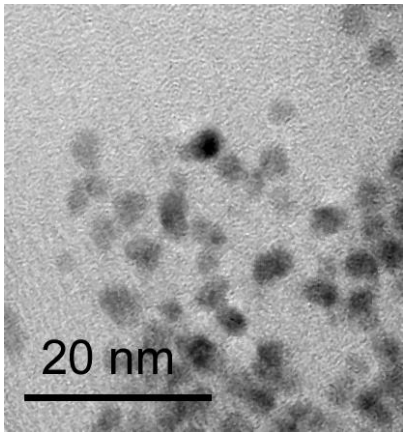

*Figure S6.11-2 TEM image of **NP10**.*

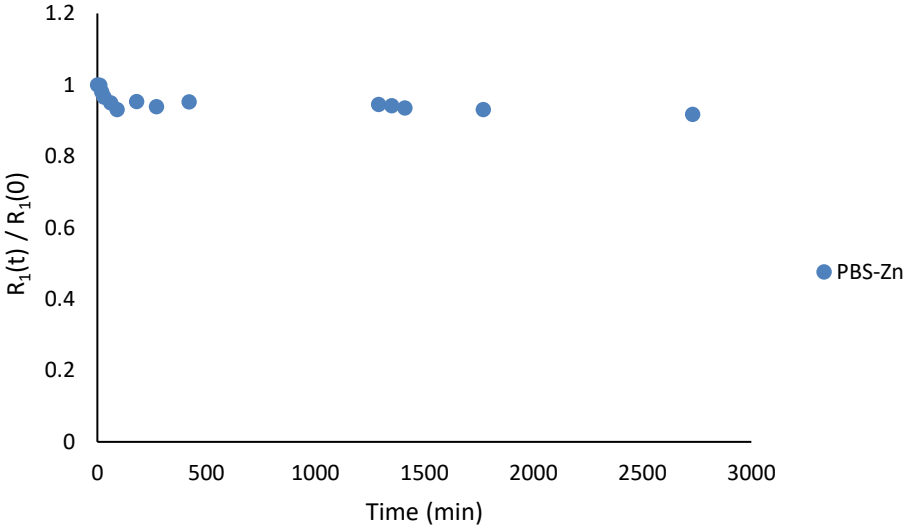

*Figure S6.11-3 Relaxivity for **NP10** between t = 0 and t = 2610 minutes on addition of Zn^{2+} (2 eq per Gd) in a transmetallation experiment at 37 °C.*

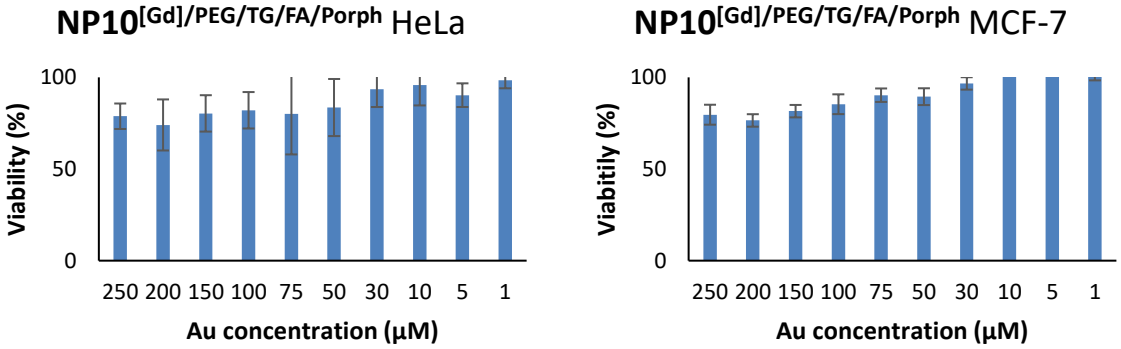

*Figure S6.11-4 Cell viability of HeLa and MCF-7 cells incubated with different concentrations of **NP10** after 24h.*

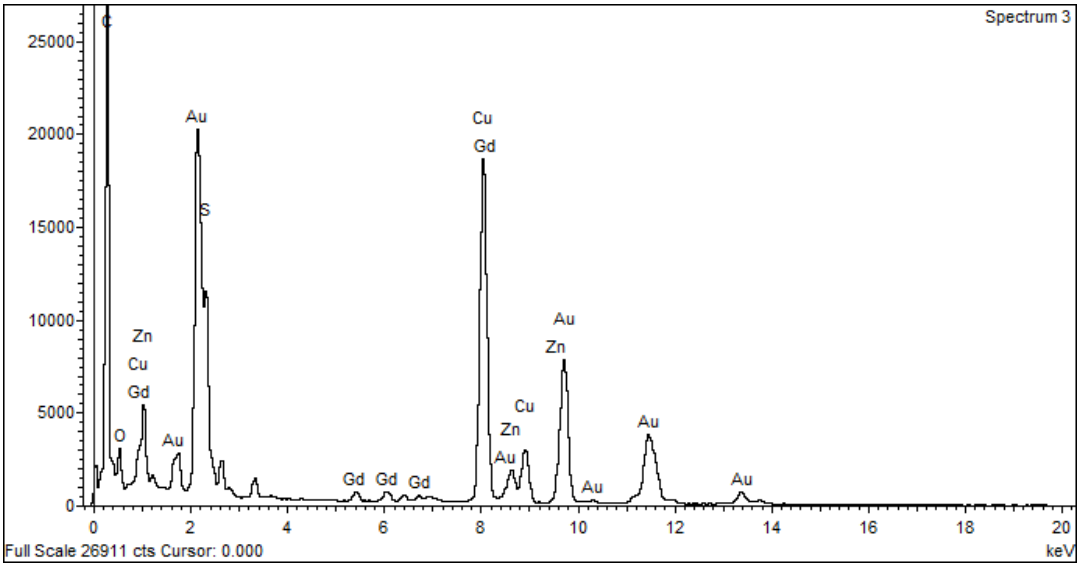

*Figure S6.11-5 EDX data for **NP10***

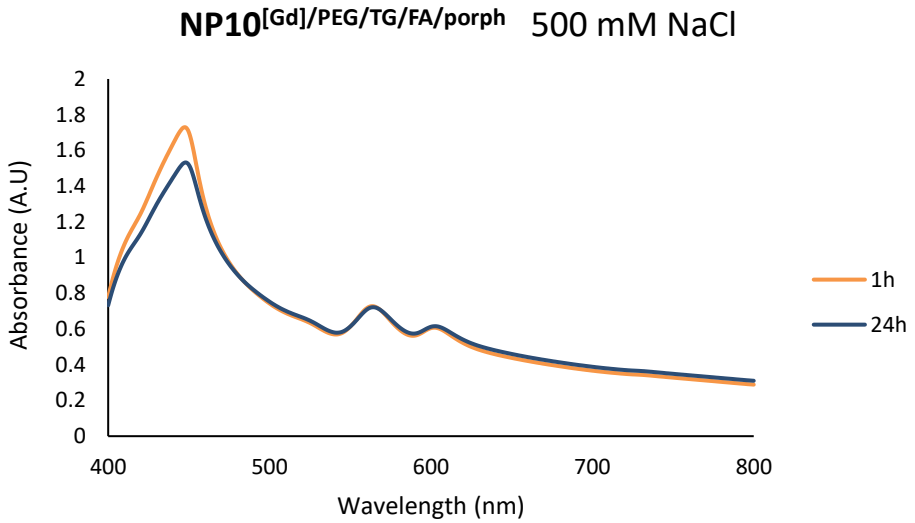

*Figure S6.11-6 Stability of **NP10** at various salt concentrations over time.*

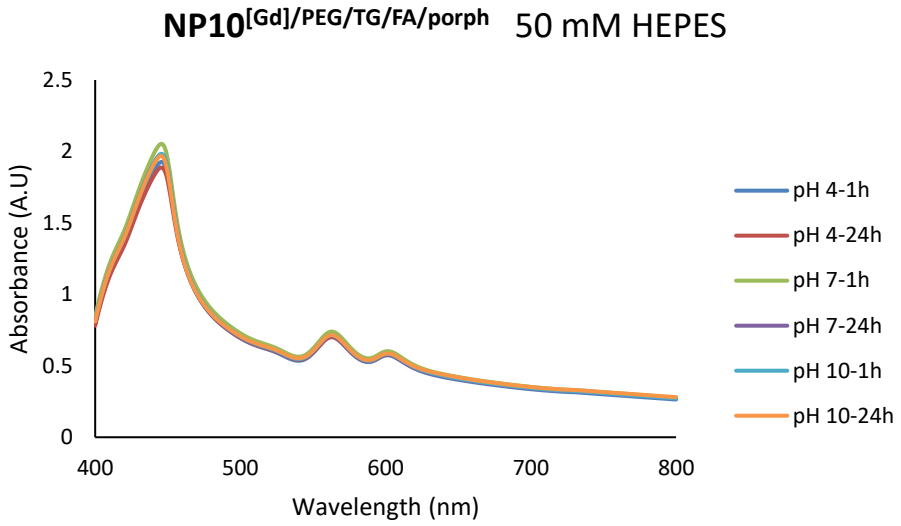

*Figure S6.11-7 UV-vis spectra of **NP10** at various pH values over time.*

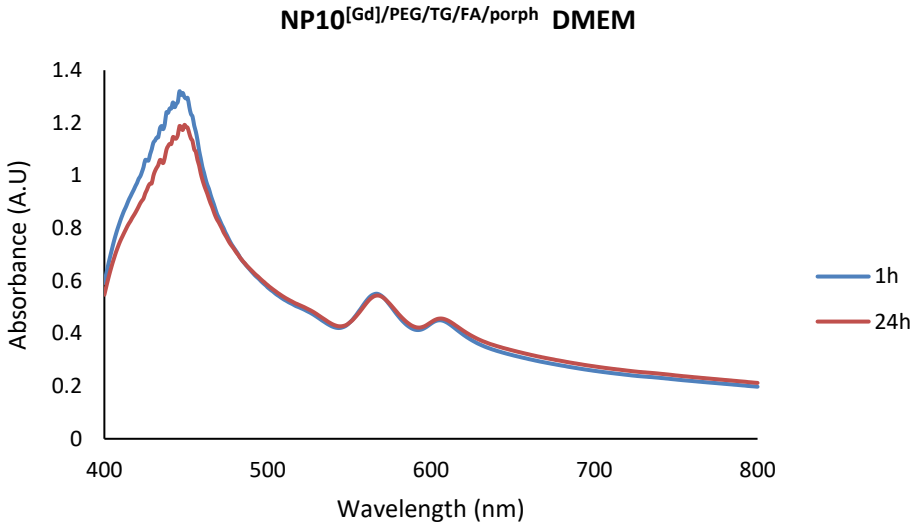

*Figure S6.11-8 UV-vis spectra of **NP10** in DMEM over time.*

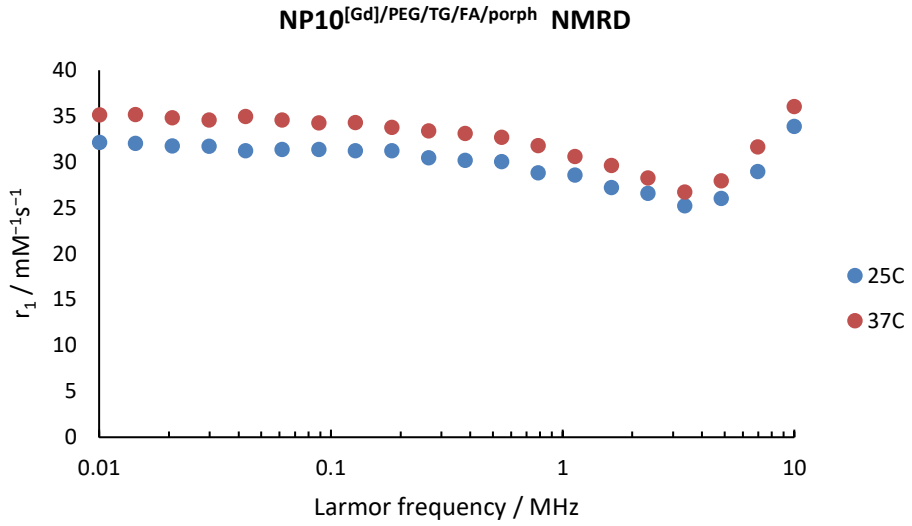

*Figure S6.11-9 NMRD profiles of **NP10** at 25 and 37 °C.*

*Table S6.11-1 Zeta potential, DLS and size of **NP10**.*

Zeta potential / mV	− 34.4
TEM diameter / nm	2.82 ± 0.58
Hydrodynamic diameter / nm	37.89 ± 12.86

*Table S6.11-2 Ratios of Au to Gd determined by ICP-OES and overall relaxivity of **NP10**.*

	Ratio (Au/Gd)	**NP r_1 (10 MHz) at 37 °C**
NP8[Gd]/PEG/TG/FA/Porph	19:1	2090

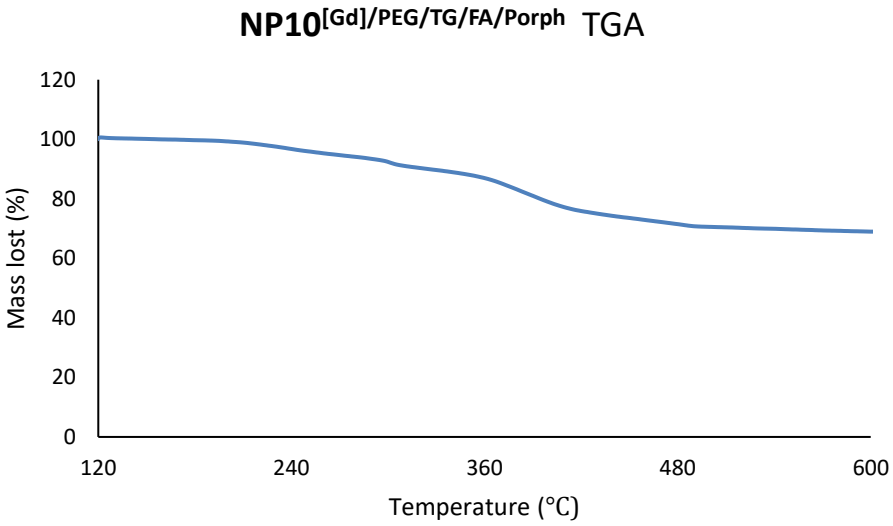

*Figure S6.11-10 TGA data for **NP10**.*

S7. Summary of NMRD profiles

The NMRD profiles were measured at ^{1}H Larmor frequencies from 0.01 to 10 MHz using a Stelar SMARtracer™ FFC NMR relaxometer (0.25 T), equipped with a VTC90 temperature control unit. Each point was measured 8 times and if the deviation was outside 1% the measurement was repeated and the average value was taken. The measurements were made at 25 °C and 37 °C for each gold nanoparticle (AuNP) and the precise concentration of Gd^{3+} was determined using by ICP-OES. The r_1 values were calculated using the below equation, with R_1 being the relaxation rate measured, R_{1d} the diamagnetic constant of the solvent and [CA] the concentration of Gd^{3+}.

$$R_1 = r_1[CA] + R_{1d}$$

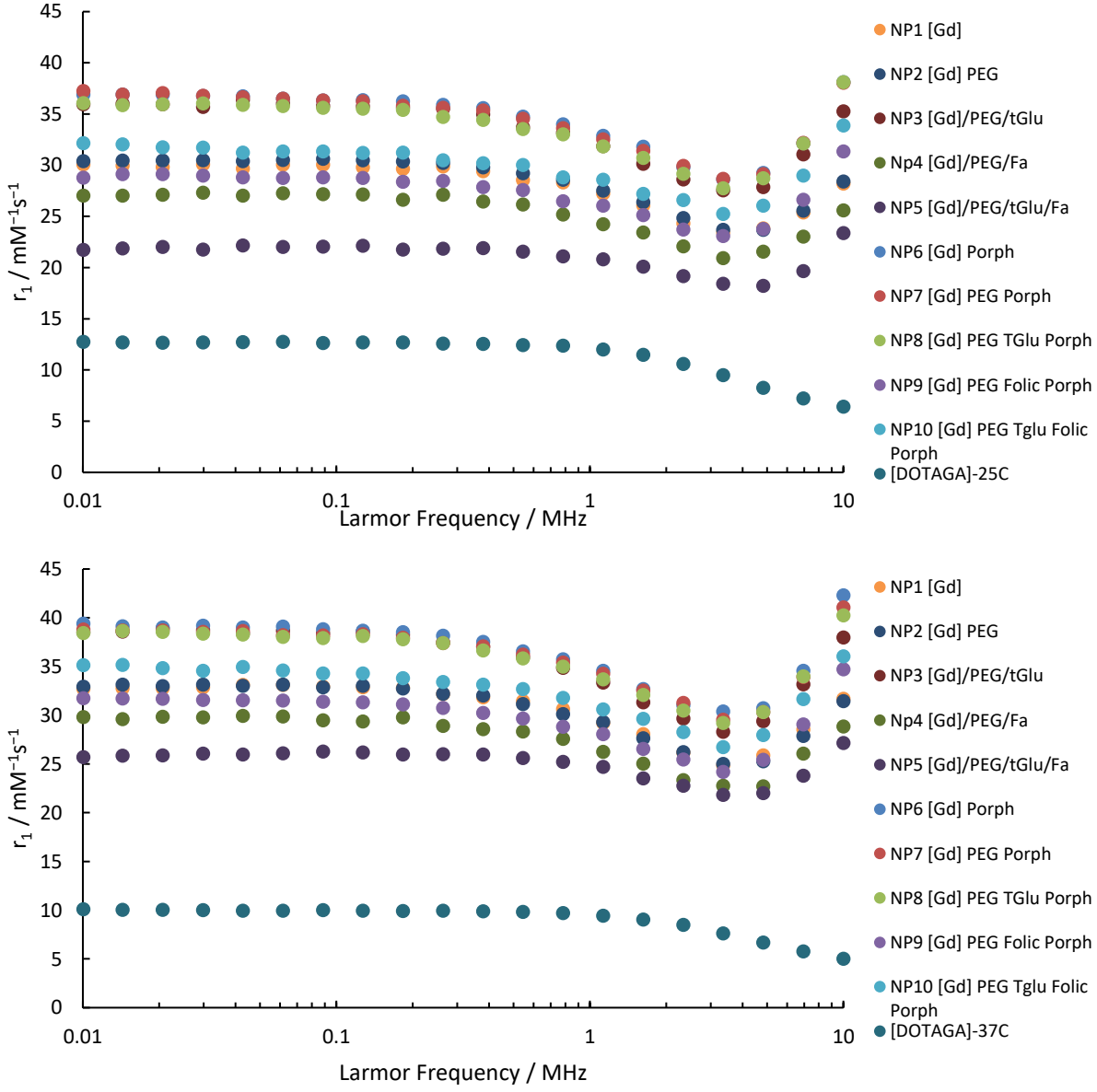

*Figure S7-1 NMRD profiles of **NP1** – **NP10** and **8** (labelled DOTAGA) per Gd unit at 25 °C (above) and 37 °C (below).*

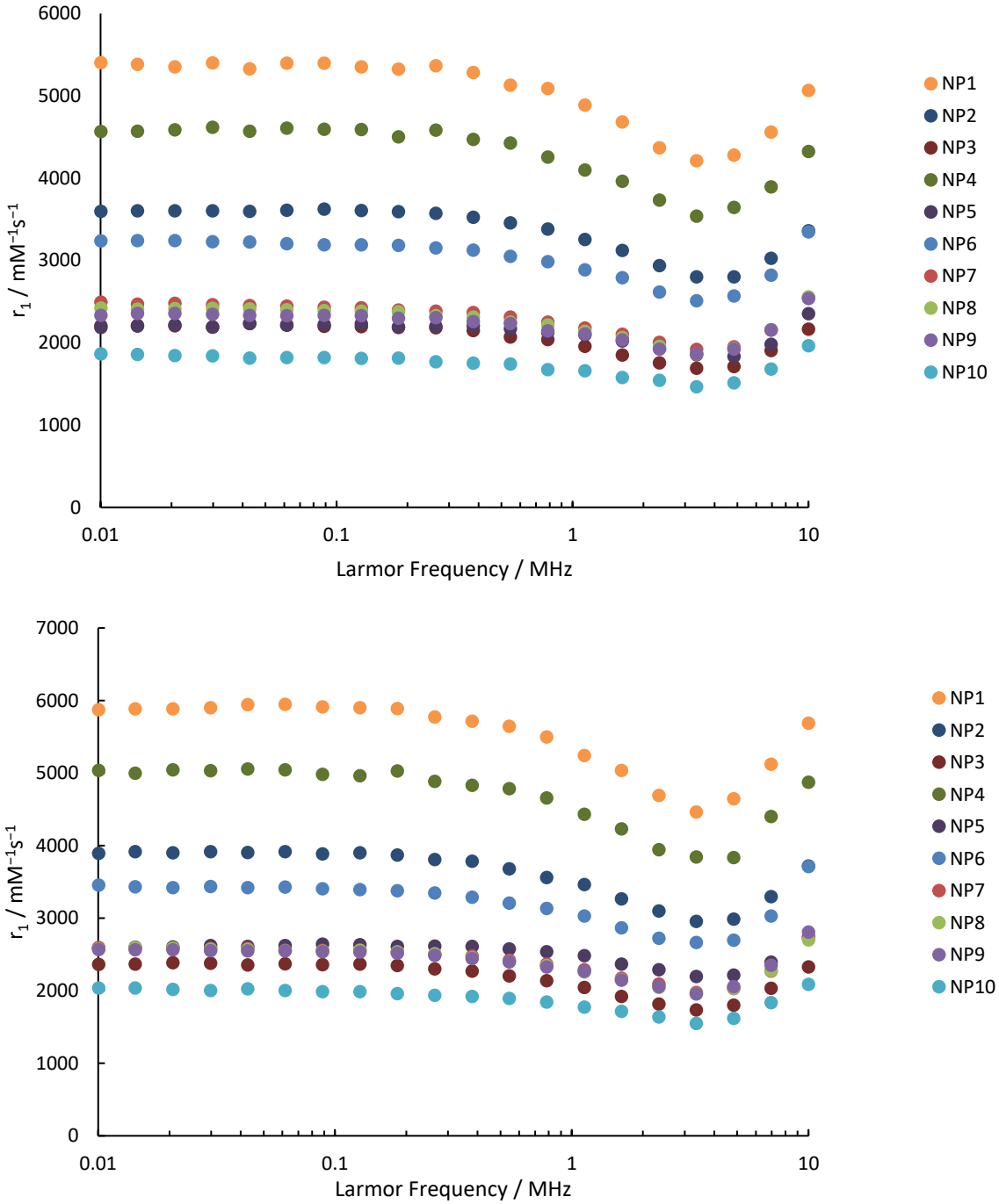

*Figure S7-2 NMRD profiles of **NP1** – **NP10** per nanoparticle at 25 °C (above) and 37 °C (below).*

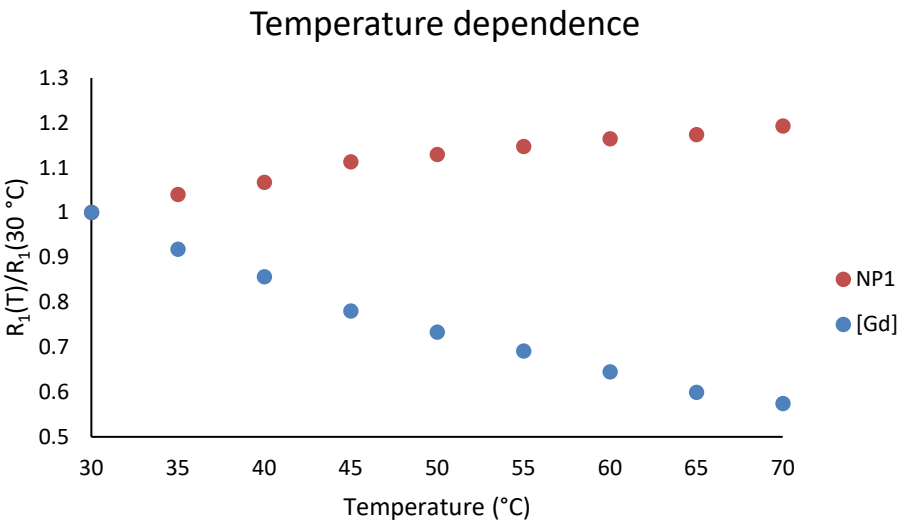

*Figure S7-3 Temperature dependence comparison between **NP1** and **8**.*

S8 Magnetic resonance imaging

Magnetic resonance imaging was performed at 25 °C on a clinical 1.5 T MRI Scanner (Philips Ingenia, Philips Medical Systems) using a Modified Look-Locker Imaging (MOLLI) T_1 sequence. The scan parameters were as follows: 15 x 300 x 300 mm field of view, 300 x 300 mm acquisition matrix, 3 mm slice thickness, 2.145 ms echo time, 4.290 ms repetition time and 50° flip angle. Each nanoparticle sample was prepared at gadolinium concentrations (ICP-OES) between 0.01 and 0.065 mM. The 1 mL phantoms were submerged in water during acquisition to reduce Gibbs artefacts. The T_1 maps were analysed using Philips DICOM Viewer 3.0. T_1 values were extracted for each nanoparticle sample across 5 slices and a mean average value was taken. R_1 was then plotted against gadolinium concentration and the gradient of the straight line was taken to be the relaxivity.

S9. ICP-OES and relaxivity data per nanoparticle summary

ICP-OES analyses were performed on a Perkin Elmer Optima 2000 DV OES and 3 references were used (0.2, 5, 25 ppm solutions of the appropriate metal) in order to determine the precise concentration of the chosen metal. Prior to the measurement, the gold nanoparticles were digested in *aqua regia* at room temperature for a minimum of 3 hours before being diluted with water to reach a 10% concentration in *aqua regia*.

*Table S9-1 Summary of data for **NP1** – **NP10***

Nanoparticle	Ratio atoms (Au/Gd) ICP-OES	r_1 ($mM^{-1}s^{-1}$) 10 MHz at 37 °C	NP r_1 ($mM^{-1}s^{-1}$) 10 MHz at 37 °C	Size (nm) TEM	Mass loss (%) TGA
NP1$^{[Gd]}$	$Au_{3301}Gd_{179}$ (18/1)	31.68	5691	4.08 ± 0.67	16
NP2$^{[Gd]/PEG}$	$Au_{3018}Gd_{118}$ (26/1)	31.44	3719	3.96 ± 0.74	21
NP3$^{[Gd]/PEG/TG}$	$Au_{2516}Gd_{61}$ (37/1)	37.96	2330	3.72 ± 0.69	41
NP4$^{[Gd]/PEG/FA}$	$Au_{2502}Gd_{169}$ (15/1)	28.83	4874	3.72 ± 0.73	21
NP5$^{[Gd]/PEG/FA/TG}$	$Au_{2709}Gd_{100}$ (27/1)	27.13	2932	3.83 ±0.59	18
NP6$^{[Gd]/Porph}$	$Au_{1033}Gd_{87}$ (12/1)	42.21	3713	2.77 ± 0.49	24
NP7$^{[Gd]/PEG/Porph}$	$Au_{874}Gd_{67}$ (13/1)	40.88	2749	2.62 ± 0.53	24
NP8$^{[Gd]/PEG/TG/Porph}$	$Au_{1235}Gd_{67}$ (18/1)	40.24	2701	2.93 ± 0.53	30
NP9$^{[Gd]/PEG/FA/Porph}$	$Au_{1338}Gd_{80}$ (16/1)	34.72	2810	3.02 ± 0.63	30
NP10$^{[Gd]/PEG/FA/TG/Porph}$	$Au_{1090}Gd_{58}$(19/1)	36.02	2090	2.82 ± 0.58	31

S10 Time course study of cell uptake of GNP in HeLa and MCF-7 cells

For cell uptake studies, cells were seeded into a 96-well plate (Corning® Costar®, Sigma-Aldrich) at a density of 15,000 cells per well and incubated for 24 h at 37 °C in a 5% CO_2 incubator. The cells were then incubated with a 200 µM solution of the respective nanoparticle for a period of 1, 6 or 24 hours and in duplicates. The media was then removed and the cells were washed three times with PBS to ensure that all un-internalized nanoparticles had been removed. The cells were then fixed using a 4% formaldehyde solution and digested using *aqua regia* for at least 2 hours at room temperature. The digested solutions were then diluted with water to reach a 10% concentration of *aqua regia* and the gold concentration was measured using ICP-OES.

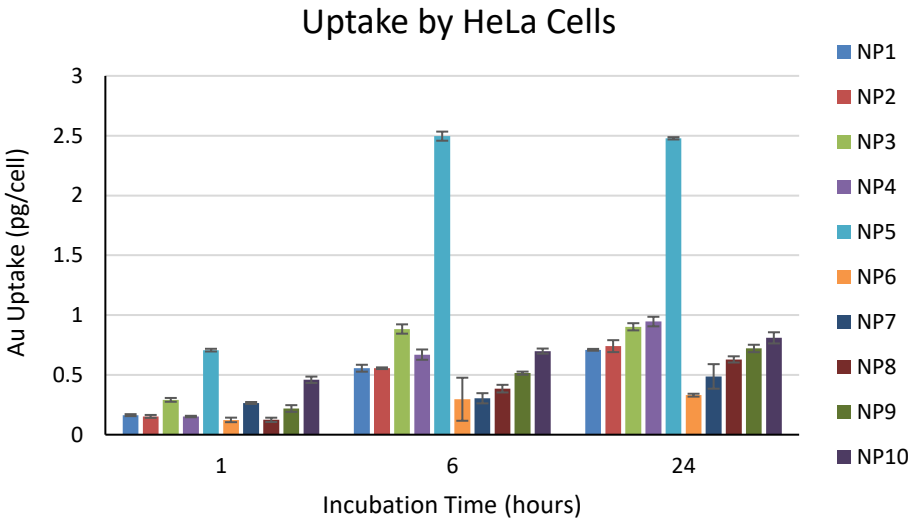

Figure S10-1 Uptake in HeLa cells incubated with 200 µM of ***NP1*** *-* ***NP10*** *after 1, 6, 24 hours.*

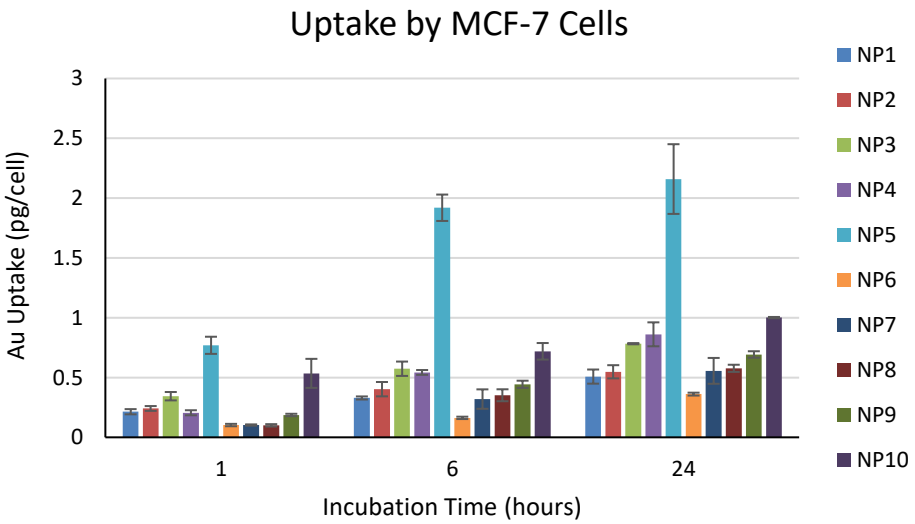

Figure S10-2 Uptake in MCF-7 cells incubated with 200 µM of ***NP1*** *-* ***10*** *after 1, 6, 24 hours.*

The data in Figure 12 are quoted in GNP/mL to take into account the differing sizes of the NPs. This was calculated in the following manner:

In preparing the samples for ICP-OES, the nanoparticles underwent a 7.5-fold dilution. Therefore, the gold concentrations (in mg/L), as determined by ICP-OES, were first multiplied by 7.5 to give gold concentration in each well. The volume of solution in each well was 200 µL, so dividing each value by 5000 gave the mass of gold (in mg) in each well. These values were then divided by 15,000 (number of cells per well) to give mass of gold per cell. These values were then divided by the mass of the gold nanoparticle, to give number of nanoparticles per cell.

The mass of each nanoparticle was calculated using the radius, as measured by TEM. First, the volume of each nanoparticle was calculated using the volume of a sphere equation:

$$V = \frac{4}{3}\,\pi\, r^3$$

The mass of each nanoparticle was calculated by multiplying the volume of the nanoparticle by the density of gold (19.32 g cm^{-3}).

$$density = \frac{mass}{volume}$$

As an alternative, the data are shown below in terms of picograms per cell:

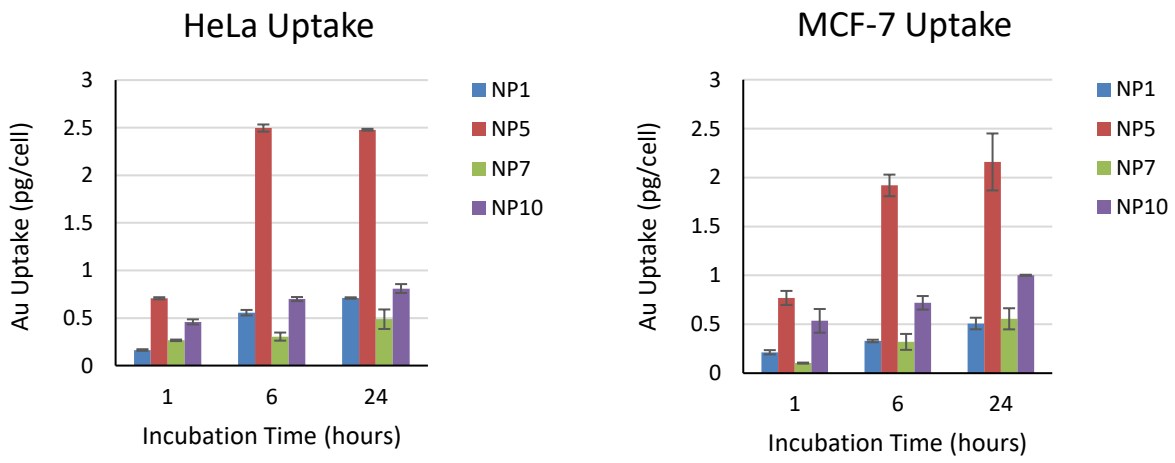

*Figure S10-3. Cell uptake studies (quoted in pg/cell) performed with **NP1**, **NP5**, **NP7** and **NP10** (200 µM) over various incubation times for HeLa (left) and MCF-7 cells (right).*

S11 *In vitro* photodynamic therapy study

HeLa cells were seeded into 8-well plates (Corning Costar, Sigma Aldrich) at a density of 30,000 cells per well and incubated for 24 h at 37 °C, in 5% CO_2. The cells were then incubated with a 200 µM solution of the respective nanoparticle in media for a further 24 h. The media was then removed and the cells were washed 3 times with PBS before fresh media was added. Each well was then irradiated with a 570 nm laser, at 37 °C on a Zeiss-Axio Observer inverted microscope for a period of 5, 15 or 30 min. To measure cell viability, an MTT assay was performed whereby the media was replaced with a solution of MTT (3-(4,5-dimethylthiazol-2-yl)-2,5-diphenyltetrazolium bromide) in PBS (2 mg/mL) before incubating the cells for 2 h. The solution was then replaced with DMSO before incubating the cells at room temperature, in the dark. Absorbance was measured at 570 nm, using a plate reader (SpectraMax M2/M2e Microplate Reader, Molecular Devices) and reported as a percentage, relative to the absorbance of cells that had been incubated with only media (no nanoparticles).

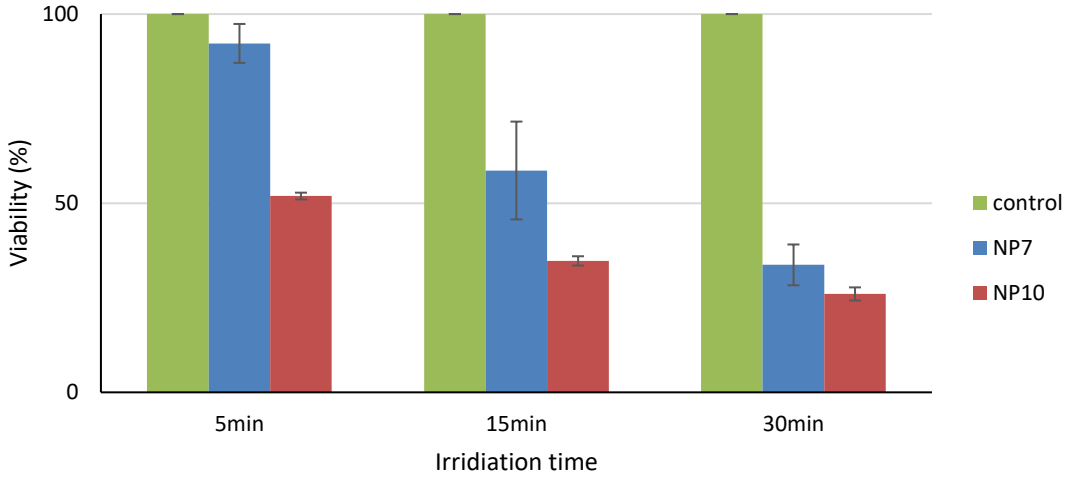

*Figure S11-1 Cell viability on irradiation of cells incubated with **NP7** and **NP10** at 570 nm.*

S12 Crystallographic data for porphyrin unit

Crystal data for **15'**: $C_{56}H_{49}N_5O_4S_2Zn{\cdot}1.35(C_4H_8O)$, M = 1082.83, trigonal, R-3 (no. 148), a = b = 50.2134(14), c = 11.0418(3) Å, V = 24110.7(15) Å^3, Z = 18, D_c = 1.342 g cm^{-3}, μ(Mo-Kα) = 0.593 mm^{-1}, T = 173 K, dark red blocks, Agilent Xcalibur 3 E diffractometer; 11584 independent measured reflections (R_{int} = 0.0412), F^2 refinement,[8,9] R_1(obs) = 0.1039, wR_2(all) = 0.2750, 8535 independent observed absorption-corrected reflections [$|F_o| > 4\sigma(|F_o|)$, completeness to θ_{full}(25.2°) = 99.9%], 636 parameters. CCDC 1913151.

The C46- and C52-based phenyl rings, and the O60-based coordinated tetrahydrofuran (THF) molecule in the structure of **15'** (formed by aerial oxidation of **15** during the crystallization experiment) were all found to be disordered, and in each case two orientations were identified, of *ca*. 67:33, 52:48 and 67:33% occupancy respectively. The geometries of each pair of orientations were optimized, the thermal parameters of adjacent atoms were restrained to be similar, and only the non-hydrogen atoms of the major occupancy orientations were refined anisotropically (those of the minor occupancy orientations were refined isotropically). The presumed N27–H hydrogen atom could not be reliably located from ΔF maps, and so was added in a calculated position at an N–H distance of 0.90 Å.

The included solvent was found to be highly disordered, and the best approach to handling this diffuse electron density was found to be the SQUEEZE routine of PLATON.[10] This suggested a total of 974 electrons per unit cell, equivalent to 54.1 electrons per molecule. Before the use of SQUEEZE the solvent most resembled tetrahydrofuran (THF, C_4H_8O, 40 electrons), and 1.35 THF molecules corresponds to 54 electrons, so this was used as the solvent present. As a result, the atom list for the asymmetric unit is low by $1.35(C_4H_8O) = C_{5.4}H_{10.8}O_{1.35}$ (and that for the unit cell low by $C_{97.2}H_{194.4}O_{24.3}$) compared to what is actually presumed to be present.

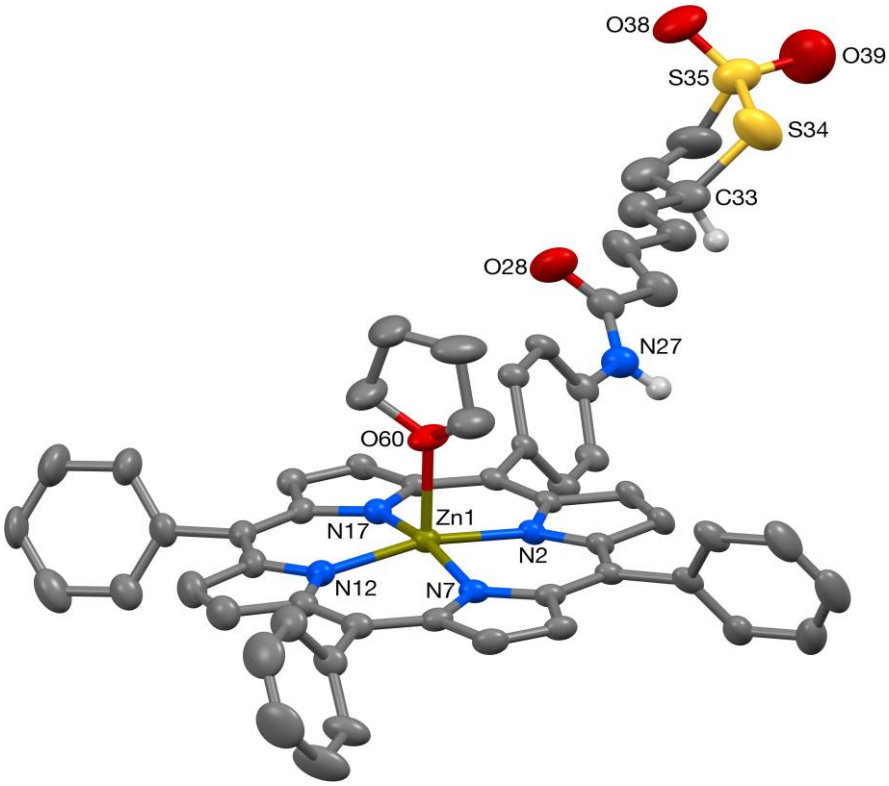

Figure S12-1 Structure of Porph-SH (**15**) ligand in oxidized form (**15'**), with 30% probability ellipsoids.

Table S12-2 Bond lengths [Å] and angles [°]

Zn(1)-N(17)	2.058(4)
Zn(1)-N(2)	2.064(4)
Zn(1)-N(12)	2.066(5)
Zn(1)-N(7)	2.069(4)
Zn(1)-O(60)	2.161(7)
Zn(1)-O(60')	2.198(14)
C(1)-C(20)	1.381(7)
C(1)-C(2)	1.406(7)
C(1)-C(21)	1.515(7)
C(2)-N(2)	1.384(6)
C(2)-C(3)	1.450(7)
N(2)-C(5)	1.359(6)
C(3)-C(4)	1.356(7)
C(4)-C(5)	1.436(8)
C(5)-C(6)	1.414(7)
C(6)-C(7)	1.410(7)
C(6)-C(40)	1.488(8)
C(7)-N(7)	1.370(7)
C(7)-C(8)	1.455(7)
N(7)-C(10)	1.373(7)
C(8)-C(9)	1.343(9)
C(9)-C(10)	1.432(8)
C(10)-C(11)	1.409(8)
C(11)-C(12)	1.413(8)
C(11)-C(46)	1.492(7)
C(11)-C(46')	1.514(13)
C(12)-N(12)	1.372(7)
C(12)-C(13)	1.419(9)
N(12)-C(15)	1.375(7)
C(13)-C(14)	1.315(10)
C(14)-C(15)	1.458(8)
C(15)-C(16)	1.417(8)
C(16)-C(17)	1.397(8)
C(16)-C(52')	1.493(10)
C(16)-C(52)	1.509(8)
C(17)-N(17)	1.374(7)
C(17)-C(18)	1.456(8)
N(17)-C(20)	1.385(7)
C(18)-C(19)	1.342(8)
C(19)-C(20)	1.448(7)
C(21)-C(26)	1.382(8)
C(21)-C(22)	1.398(7)
C(22)-C(23)	1.396(8)
C(23)-C(24)	1.396(9)
C(24)-C(25)	1.369(8)
C(24)-N(27)	1.431(8)
C(25)-C(26)	1.371(8)
N(27)-C(28)	1.333(9)

C(28)-O(28)	1.220(9)
C(28)-C(29)	1.505(10)
C(29)-C(30)	1.498(11)
C(30)-C(31)	1.543(11)
C(31)-C(32)	1.476(11)
C(32)-C(33)	1.506(11)
C(33)-C(37)	1.489(12)
C(33)-S(34)	1.822(9)
S(34)-S(35)	2.086(3)
S(35)-O(38)	1.435(7)
S(35)-O(39)	1.444(9)
S(35)-C(36)	1.661(12)
C(36)-C(37)	1.434(15)
C(40)-C(45)	1.384(9)
C(40)-C(41)	1.398(9)
C(41)-C(42)	1.373(10)
C(42)-C(43)	1.368(13)
C(43)-C(44)	1.394(13)
C(44)-C(45)	1.409(10)
C(46)-C(47)	1.3900
C(46)-C(51)	1.3900
C(47)-C(48)	1.3900
C(48)-C(49)	1.3900
C(49)-C(50)	1.3900
C(50)-C(51)	1.3900
C(46')-C(47')	1.3900
C(46')-C(51')	1.3900
C(47')-C(48')	1.3900
C(48')-C(49')	1.3900
C(49')-C(50')	1.3900
C(50')-C(51')	1.3900
C(52)-C(53)	1.3900
C(52)-C(57)	1.3900
C(53)-C(54)	1.3900
C(54)-C(55)	1.3900
C(55)-C(56)	1.3900
C(56)-C(57)	1.3900
C(52')-C(53')	1.3900
C(52')-C(57')	1.3900
C(53')-C(54')	1.3900
C(54')-C(55')	1.3900
C(55')-C(56')	1.3900
C(56')-C(57')	1.3900
O(60)-C(64)	1.377(12)
O(60)-C(61)	1.428(11)
C(61)-C(62)	1.449(11)
C(62)-C(63)	1.443(13)
C(63)-C(64)	1.471(11)
O(60')-C(61')	1.417(15)
O(60')-C(64')	1.427(15)

C(61')-C(62')	1.479(15)
C(62')-C(63')	1.486(15)
C(63')-C(64')	1.453(15)

N(17)-Zn(1)-N(2)	89.98(17)
N(17)-Zn(1)-N(12)	89.21(18)
N(2)-Zn(1)-N(12)	165.42(18)
N(17)-Zn(1)-N(7)	167.08(17)
N(2)-Zn(1)-N(7)	88.98(17)
N(12)-Zn(1)-N(7)	88.57(18)
N(17)-Zn(1)-O(60)	97.1(3)
N(2)-Zn(1)-O(60)	94.8(3)
N(12)-Zn(1)-O(60)	99.7(3)
N(7)-Zn(1)-O(60)	95.8(3)
N(17)-Zn(1)-O(60')	97.6(7)
N(2)-Zn(1)-O(60')	97.7(5)
N(12)-Zn(1)-O(60')	96.8(5)
N(7)-Zn(1)-O(60')	95.3(7)
C(20)-C(1)-C(2)	125.6(5)
C(20)-C(1)-C(21)	117.7(4)
C(2)-C(1)-C(21)	116.7(4)
N(2)-C(2)-C(1)	125.8(5)
N(2)-C(2)-C(3)	108.7(4)
C(1)-C(2)-C(3)	125.5(5)
C(5)-N(2)-C(2)	107.1(4)
C(5)-N(2)-Zn(1)	126.7(3)
C(2)-N(2)-Zn(1)	125.2(3)
C(4)-C(3)-C(2)	107.1(5)
C(3)-C(4)-C(5)	107.2(5)
N(2)-C(5)-C(6)	125.7(5)
N(2)-C(5)-C(4)	110.0(4)
C(6)-C(5)-C(4)	124.3(5)
C(7)-C(6)-C(5)	124.8(5)
C(7)-C(6)-C(40)	116.4(4)
C(5)-C(6)-C(40)	118.8(5)
N(7)-C(7)-C(6)	126.0(4)
N(7)-C(7)-C(8)	109.2(5)
C(6)-C(7)-C(8)	124.7(5)
C(7)-N(7)-C(10)	106.6(4)
C(7)-N(7)-Zn(1)	126.0(3)
C(10)-N(7)-Zn(1)	126.9(4)
C(9)-C(8)-C(7)	106.7(5)
C(8)-C(9)-C(10)	107.8(5)
N(7)-C(10)-C(11)	125.4(5)
N(7)-C(10)-C(9)	109.6(5)
C(11)-C(10)-C(9)	124.9(5)
C(10)-C(11)-C(12)	125.7(5)
C(10)-C(11)-C(46)	115.4(6)
C(12)-C(11)-C(46)	118.9(6)
C(10)-C(11)-C(46')	120.0(9)

C(12)-C(11)-C(46')	114.2(9)
N(12)-C(12)-C(11)	124.7(5)
N(12)-C(12)-C(13)	110.1(5)
C(11)-C(12)-C(13)	125.2(5)
C(12)-N(12)-C(15)	106.2(5)
C(12)-N(12)-Zn(1)	127.6(4)
C(15)-N(12)-Zn(1)	126.0(4)
C(14)-C(13)-C(12)	107.8(6)
C(13)-C(14)-C(15)	107.9(6)
N(12)-C(15)-C(16)	126.6(5)
N(12)-C(15)-C(14)	108.1(5)
C(16)-C(15)-C(14)	125.4(6)
C(17)-C(16)-C(15)	124.4(5)
C(17)-C(16)-C(52')	121.0(7)
C(15)-C(16)-C(52')	114.5(7)
C(17)-C(16)-C(52)	116.5(6)
C(15)-C(16)-C(52)	119.0(6)
N(17)-C(17)-C(16)	126.1(5)
N(17)-C(17)-C(18)	108.8(5)
C(16)-C(17)-C(18)	125.2(5)
C(17)-N(17)-C(20)	107.4(4)
C(17)-N(17)-Zn(1)	127.1(4)
C(20)-N(17)-Zn(1)	125.3(3)
C(19)-C(18)-C(17)	107.3(5)
C(18)-C(19)-C(20)	108.0(5)
C(1)-C(20)-N(17)	126.5(5)
C(1)-C(20)-C(19)	125.0(5)
N(17)-C(20)-C(19)	108.4(5)
C(26)-C(21)-C(22)	118.3(5)
C(26)-C(21)-C(1)	121.1(5)
C(22)-C(21)-C(1)	120.6(5)
C(23)-C(22)-C(21)	119.8(5)
C(24)-C(23)-C(22)	120.3(5)
C(25)-C(24)-C(23)	119.2(5)
C(25)-C(24)-N(27)	116.2(6)
C(23)-C(24)-N(27)	124.4(6)
C(24)-C(25)-C(26)	120.5(6)
C(25)-C(26)-C(21)	121.8(5)
C(28)-N(27)-C(24)	128.8(6)
O(28)-C(28)-N(27)	122.2(7)
O(28)-C(28)-C(29)	121.3(7)
N(27)-C(28)-C(29)	116.5(7)
C(30)-C(29)-C(28)	115.3(7)
C(29)-C(30)-C(31)	113.5(7)
C(32)-C(31)-C(30)	113.6(7)
C(31)-C(32)-C(33)	116.4(8)
C(37)-C(33)-C(32)	113.6(9)
C(37)-C(33)-S(34)	108.0(6)
C(32)-C(33)-S(34)	110.6(6)
C(33)-S(34)-S(35)	93.0(3)

O(38)-S(35)-O(39)	118.6(6)
O(38)-S(35)-C(36)	106.2(6)
O(39)-S(35)-C(36)	113.1(7)
O(38)-S(35)-S(34)	110.2(3)
O(39)-S(35)-S(34)	110.5(5)
C(36)-S(35)-S(34)	95.8(4)
C(37)-C(36)-S(35)	107.2(9)
C(36)-C(37)-C(33)	111.3(10)
C(45)-C(40)-C(41)	118.1(6)
C(45)-C(40)-C(6)	122.2(6)
C(41)-C(40)-C(6)	119.6(6)
C(42)-C(41)-C(40)	121.7(8)
C(43)-C(42)-C(41)	120.0(8)
C(42)-C(43)-C(44)	120.4(8)
C(43)-C(44)-C(45)	119.2(8)
C(40)-C(45)-C(44)	120.5(8)
C(47)-C(46)-C(51)	120.0
C(47)-C(46)-C(11)	119.4(5)
C(51)-C(46)-C(11)	120.6(5)
C(48)-C(47)-C(46)	120.0
C(49)-C(48)-C(47)	120.0
C(48)-C(49)-C(50)	120.0
C(51)-C(50)-C(49)	120.0
C(50)-C(51)-C(46)	120.0
C(47')-C(46')-C(51')	120.0
C(47')-C(46')-C(11)	120.0(13)
C(51')-C(46')-C(11)	119.8(13)
C(46')-C(47')-C(48')	120.0
C(49')-C(48')-C(47')	120.0
C(50')-C(49')-C(48')	120.0
C(51')-C(50')-C(49')	120.0
C(50')-C(51')-C(46')	120.0
C(53)-C(52)-C(57)	120.0
C(53)-C(52)-C(16)	122.0(7)
C(57)-C(52)-C(16)	118.0(7)
C(54)-C(53)-C(52)	120.0
C(53)-C(54)-C(55)	120.0
C(56)-C(55)-C(54)	120.0
C(57)-C(56)-C(55)	120.0
C(56)-C(57)-C(52)	120.0
C(53')-C(52')-C(57')	120.0
C(53')-C(52')-C(16)	119.3(8)
C(57')-C(52')-C(16)	120.6(8)
C(54')-C(53')-C(52')	120.0
C(55')-C(54')-C(53')	120.0
C(54')-C(55')-C(56')	120.0
C(55')-C(56')-C(57')	120.0
C(56')-C(57')-C(52')	120.0
C(64)-O(60)-C(61)	107.4(9)
C(64)-O(60)-Zn(1)	122.8(7)

C(61)-O(60)-Zn(1)	122.1(8)
O(60)-C(61)-C(62)	105.2(8)
C(63)-C(62)-C(61)	106.1(7)
C(62)-C(63)-C(64)	106.3(7)
O(60)-C(64)-C(63)	106.4(8)
C(61')-O(60')-C(64')	108.1(11)
C(61')-O(60')-Zn(1)	119.1(12)
C(64')-O(60')-Zn(1)	116.3(12)
O(60')-C(61')-C(62')	104.7(11)
C(61')-C(62')-C(63')	100.8(11)
C(64')-C(63')-C(62')	100.9(11)
O(60')-C(64')-C(63')	105.8(10)

S13 References

1. B. Jagadish, G. L. Brickert-Albrecht, G. S. Nichol, E. A. Mash, N. Raghunand, *Tetrahedron Lett*. **2011**, *52*, 2058-2061.
2. N. Sim, R. Pal, D. Parker, J. Engelmann, A. Mishra, S. Gottschalk, *Org. Biomol. Chem*. **2014**, *12*, 9389-9404.
3. K.-P. Eisenwiener, P. Powell, H. R. Mäcke, *Bioorganic & Medicinal Chemistry Letters* **2000**, *10*, 2133-2135.
4. J. Park, W. I. Jeon, S. Y. Lee, K.-S. Ock, J. H. Seo, J. Park, E.-O. Ganbold, K. Cho, N. W. Song, S.-W. Joo, *J. Biomed. Mater. Res. A.* **2012**, *100*, 1221-1228.
5. A. D. Adler, F. R. Longo, J. D. Finarelli, J. Goldmacher, J. Assour, L. A. Korsakoff, *J. Org. Chem.* **1967**, *32*, 476-476.
6. R. Luguya, L. Jaquinod, F. R. Fronczek, M. G. H. Vicente, K. M. Smith, *Tetrahedron* **2004**, *60*, 2757-2763.
7. M. Brust, J. Fink, D. Bethell, D. J. Schiffrin, C. Kiely, *J. Chem. Soc., Chem. Commun.* **1995**, 1655-1656.
8. SHELXTL v5.1, Bruker AXS, Madison, WI, **1998**.
9. SHELX-2013, G. M. Sheldrick, *Acta Cryst.* **2015**, *C71*, 3-8.
10. A. L. Spek, (2003, 2009) PLATON, A Multipurpose Crystallographic Tool, Utrecht University, Utrecht, The Netherlands. See also A. L. Spek, *Acta. Cryst.* **2015**, *C71*, 9-18.